Multiscale Investigation of Sodium-Ion Battery Anodes: Analytical Techniques and Applications

ADVANCED ENERGY MATERIALS
www.advenergymat.de

Multiscale Investigation of Sodium-Ion Battery Anodes: Analytical Techniques and Applications

*David Schäfer, Kie Hankins, Michelle Allion, Ulrike Krewer, Franziska Karcher, Laurin Derr, Rolf Schuster, Julia Maibach, Stefan Mück, Dominik Kramer, Reiner Mönig, Fabian Jeschull, Sven Daboss, Tom Philipp, Gregor Neusser, Jan Romer, Krishnaveni Palanisamy, Christine Kranz, Florian Buchner, R. Jürgen Behm, Ali Ahmadian, Christian Kübel, Irshad Mohammad, Ago Samoson, Raiker Witter, Bernd Smarsly, and Marcus Rohnke**

The anode/electrolyte interface behavior, and by extension, the overall cell performance of sodium-ion batteries is determined by a complex interaction of processes that occur at all components of the electrochemical cell across a wide range of size- and timescales. Single-scale studies may provide incomplete insights, as they cannot capture the full picture of this complex and intertwined behavior. Broad, multiscale studies are essential to elucidate these processes. Within this perspectives article, several analytical and theoretical techniques are introduced, and described how they can be combined to provide a more complete and comprehensive understanding of sodium-ion battery (SIB) performance throughout its lifetime, with a special focus on the interfaces of hard carbon anodes. These methods target various length- and time scales, ranging from micro to nano, from cell level to atomistic structures, and account for a broad spectrum of physical and (electro)chemical characteristics. Specifically, how mass spectrometric, microscopic, spectroscopic, electrochemical, thermodynamic, and physical methods can be employed to obtain the various types of information required to understand battery behavior will be explored. Ways are then discussed how these methods can be coupled together in order to elucidate the multiscale phenomena at the anode interface and develop a holistic understanding of their relationship to overall sodium-ion battery function.

1. Introduction

One of the primary challenges in transitioning from fossil fuels to renewable energy sources is the fluctuating availability of wind and solar energy; advanced energy storage technologies are needed to ensure a reliable power supply during production and consumption peaks. Therefore, secondary batteries are gaining importance not only in the automotive industry, but also for stationary storage of electrical energy at the grid scale.[1–3]

Lithium-ion batteries (LIBs) have been at the forefront of energy storage technology since the early 1990s due to their relatively high energy density (260 Wh kg^{-1}), reasonable cost ($153 per kWh), and long lifespan.[4–6] In spite of these impressive features, LIBs exhibit several significant shortcomings that hinder their widespread use for electric vehicles and grid-scale energy storage. Two of the main constituting elements, lithium

D. Schäfer, B. Smarsly, M. Rohnke
Institute of Physical Chemistry and Center for Materials Research
Justus Liebig University Giessen
Heinrich Buff Ring 17, 35392 Giessen, Germany
E-mail: marcus.rohnke@phys.chemie.uni-giessen.de

The ORCID identification number(s) for the author(s) of this article can be found under https://doi.org/10.1002/aenm.202302830

DOI: 10.1002/aenm.202302830

K. Hankins, M. Allion, U. Krewer
Institute for Applied Materials – Electrochemical Technologies
Karlsruhe Institute of Technology
Adenauerring 20b, 76131 Karlsruhe, Germany

F. Karcher, L. Derr, R. Schuster
Institute of Physical Chemistry
Karlsruhe Institute of Technology
Kaiserstraße 12, 76131 Karlsruhe, Germany

J. Maibach
Department of Physics
Division of Materials Physics
Chalmers University of Technology
Origovägen 6B, Gothenburg SE-412 96, Sweden

and cobalt, are relatively rare and unevenly distributed across the globe, which has created mining practices that are politically and ethically concerning.[7] The scarcity of these metals, coupled with the high cost of the copper current collector, causes the overall LIB system to be too expensive and too rare for a full global transition to renewable energy, especially in developing countries. Additionally, the electrolyte species and cobalt-based cathode materials pose long-term toxicity and ecological concerns.[8]

Sodium-ion batteries (SIBs) offer several significant advantages over LIBs regarding these challenges. Sodium is the 6th most abundant element on earth and is more evenly distributed throughout the globe.[9] SIBs can be fabricated with cheaper aluminum as a current collector for both electrodes, rather than copper, and the problematic cobalt cathode components can be replaced by compounds based on less critical elements, such as manganese and iron. These factors correspond to a marked increase in safety and sustainability, and a substantial reduction in battery costs. The theoretical energy density of SIB technology, ≈150 Wh kg^{-1},[9] is lower than that of LIBs, and limits its application in portable devices and electric vehicles, where weight is a significant factor. This is less of an issue for stationery and grid-scale energy storage applications, where the gravimetric energy density is less of a concern and has a relatively low impact for grid-scale storage. This allows for SIBs to be a cost-effective alternative to LIBs as the primary energy storage technology for stationary applications.[10,3]

The chemical similarities between Li^+ and Na^+ allowed for the application of knowledge and design strategies from LIBs to guide the initial development of SIBs. The complex battery phenomena that have been the subjects of decades of study for LIBs, such as reactivity, stability, and intercalation, can be used as a baseline of comparison for SIBs. Both systems implement similar electrode materials, the same solvents, and sodium/lithium analogues of the same conducting salts.[11,12] Still, in spite of these component and mechanistic similarities, SIBs exhibit many behavioral differences compared to LIBs in regards to stability and reactivity.

Graphite has long been the standard anode material in LIBs, and provides a theoretical maximum storage capacity of 372 mAhg^{-1} (LiC_6). The Li^+ cation is able to easily intercalate between the graphene layers, however, bonding behavior of the Na^+ cation inhibits this behavior, leading to substantially diminished capacity (maximum NaC_{64}).[13–15] Research for anode materials in SIBs has instead focused on hard carbon (HC), which has previously been investigated for use in LIBs, offering storage capacities of up to 350 mAh g^{-1}.[7,16] Some of the insights gained from graphite can be applied to HC, as both are carbon-based insertion structures with relatively similar chemistries. HC is mostly derived from renewable resources such as sugar, starch, cellulose, and bio-waste such as peanut shells and fruit peels. The microstructure of the initial feedstock is preserved, though, with a lower density.[17–21] This preservation causes significant problems with battery design, as every HC sample is different, and has significantly different effects on the cell performance and SEI formation.

The carbon structure present in graphite, consisting of parallel graphene layers, is only found in HC in microscopic domains (40 Å, 2-11 layers). HC is instead comprised of disordered carbon structures, such as non-planar fragments and deformed graphene-like layers, without long-range ordering of the graphitic domains. Covalent C—O—C bonds are formed between the layers at 900 °C and are considered the main cause of both non-graphitizability and hardness. This disordered microstructure causes HC to have an amorphous macrostructure, with pores and voids up to 500 nm in diameter, and surface areas that range from <10 to >100 m^{2}g^{-1}.[17,18,22–27] These pores and voids are responsible for the effective storage of Na^+, but the exact storage mechanisms are complex and not yet fully understood.[28]

The widespread success of LIBs is largely due to the selection of effective electrolyte and electrode materials. During the initial cycles in half- and full-cells, electrolyte species react with and deposit at the electrode surface, which leads to the formation of a stable anode–electrolyte interfacial layer known as the solid electrolyte interphase (SEI).[6,16,29] The SEI layer protects the electrode surface from degradation while allowing facile ion transport, and is fundamentally important[30] for the effective function of a battery. A well-formed SEI must also passivate against further electrolyte decomposition; as a significant amount of the charge carriers are consumed during the formation process, and uncontrolled reactions diminish the capacity of the cell.[18,29,31,32] This is a significant problem in SIBs; their SEIs are shown to be significantly less stable than their LIB counterparts, in spite of having very similar chemical properties.[33,34] The loss of reversible capacity, i.e., the trapping of sodium, is quantified by the initial coulombic efficiency (ICE), a measure comparing the first charge and discharge capacities. State-of-the-art SIBs, with capacities >300 mAh g^{-1}, have achieved ICE values of 95%.[35–40]

S. Mück, D. Kramer, R. Mönig, F. Jeschull
Institute for Applied Materials
Karlsruhe Institute of Technology
Hermann-von-Helmholtz-Platz 1, 76344 Eggenstein-Leopoldshafen, Germany

S. Daboss, T. Philipp, G. Neusser, J. Romer, K. Palanisamy, C. Kranz
Institute of Analytical and Bioanalytical Chemistry
Ulm University
Albert-Einstein-Allee 11, 89081 Ulm, Germany

F. Buchner, R. J. Behm
Institute of Theoretical Chemistry
Ulm University
Oberberghof 7, 89081 Ulm, Germany

A. Ahmadian, C. Kübel
Institute of Nanotechnology
Karlsruhe Institute of Technology
Hermann-von-Helmholtz-Platz 1, 76344 Eggenstein-Leopoldshafen, Germany

A. Ahmadian, C. Kübel
Helmholtz Institute Ulm
Helmholtzstraße 11, 89081 Ulm, Germany

I. Mohammad
AIT Austrian Institute of Technology GmbH
Center for Low-Emission Transport, Battery Technologies
Giefinggasse 2, Vienna 1210, Austria

A. Samoson
Department of Cybernetics
Tallinn University of Technology
Ehitajate tee 5, Tallinn 19086, Estonia

R. Witter
Institute of Quantum Optics
Ulm University
Meyerhofstraße M26, 89081 Ulm, Germany

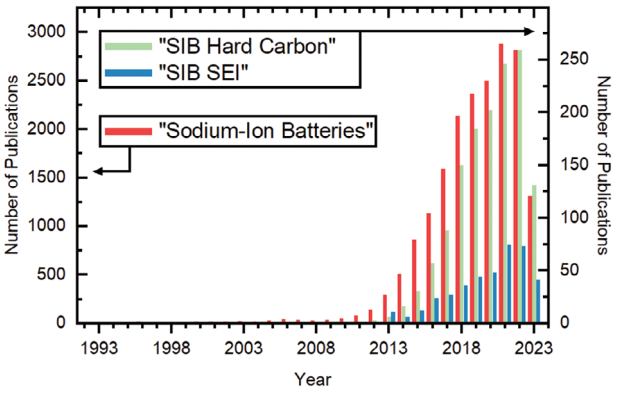

Figure 1. Number of search results for the search items as listed in the legends at webofscience.com (31/05/2023). "SIB" stands for "Sodium-Ion Batteries" as full search item.

Beyond that, batteries require a coulombic efficiency (CE) of at least 99.96%[41] to obtain suitable capacities after 500 cycles to be economically viable.

The number of publications concerning SIBs has increased exponentially since the early 2000s and the number of publications focused on the SEI over HC electrodes has grown at a commensurate rate, as can be seen in **Figure 1**. This shows firstly, the growing relevance of SIB technology in the global energy sector, and secondly, that the SEI is an integral part of the battery system. The abundance of research can be overwhelming, and the presence of vague sources and conflicting ideas can make it difficult to develop a clear, systemic, understanding of the SEI and anode interface in SIBs.

With this perspective, we highlight the techniques and methods that are necessary for the investigation of the SEI on HC in SIBs. We couple this with a focus on the type of information that is gained from each method, and how different methods can be used in conjunction to obtain a clearer picture than either method provides on their own. Finally, we suggest the need for comprehensive multiscale studies to fully investigate and develop a deeper understanding of the formation and evolution of the SEI on HC electrodes in SIBs during electrochemical cycling. The effect of small changes in component properties on overall SIB performance necessitates that these multiscale studies must work in unison, using the same materials and cell preparations, in order to obtain clear and accurate information.

2. Current State of Research

In a typical SIB, the anode (negative electrode) consists of HC with a mechanically stabilizing binder, such as polyvinylidene fluoride (PVDF)[23,42–44] or carboxymethylcellulose (CMC),[35,45,46] and an electrically conductive substance such as carbon black. Aluminum is typically used as a current collector. The positive electrode consists of the cathode material (Prussian blue analogues,[47,48] polyanionic composites,[49,50] or layered oxides[51,52]) coated onto the aluminum current collector. The electrodes are separated by a short-circuit-preventing separator and an electrolyte solution consisting of ether- or ester-based solvent(s), conductive salt, and additives. The properties and behavior of the initially formed SEI are influenced by many parameters of the battery but are most strongly impacted by the electrolyte chemistry and the electrode surface characteristics. The majority of SIB SEI research is therefore focused on either the properties of the HC anode surface, or on the electrolyte.[53,54]

The surface characteristics and ion insertion behavior of the HC anode have a significant effect on the properties of the SEI. Many studies are working to elucidate the complex storage behavior of Na^+ in HC, and there is still active debate about the exact mechanisms. The most accepted theory is known as the "3-step model" developed by Bommier et al. In this model, Na^+ is adsorbed at defect sites, intercalated between graphene sheets with larger spacing than in graphite, and ultimately accumulated in pores, resulting in a plateau region at higher capacity values.[55] Others argue that intercalation, not plating in pores, is represented by the plateau region and responsible for the majority of Na^+ storage.[56] A challenge for comparing these studies is related to the different synthesis routes from different sources and with that the inconsistent nature of HC. Different initial feedstocks produce HC with substantially different material properties and electrochemical behavior. Significant differences also emerged in HCs made from different batches of the same type of feedstock.[11,57,58] This makes a consistent study of HC very difficult, as there is no well-established baseline to use as a point of reference.

Bommier et al. also reported that the surface area accessible to adsorbed gas is proportional to the open porosity, and inversely proportional to the reversible capacity.[22] The authors explained the negative impact of open porosity by considering the proportion of exposed carbon relative to the total mass of carbon used. The highest capacities were measured in samples with the lowest proportion of exposed carbon, and vice versa, highlighting the role of available surface area for SEI formation. Defect atoms serve as nucleation sites for SEI particle formation, which aligns with cathodic electrolyte degradation.

Research is focused at engineering the HC electrode and surface design to maximize storage capacity and encourage favorable surface characteristics for SEI formation. The microstructure, surface area, and the number of defects and heteroatoms can be tailored by controlling the precursor, milling parameters, heating rate, and temperature. These methods aim to minimize the surface area of open pores while maximizing the volume of closed pores.[18] Hierarchically-porous HC surfaces have been designed in order to create microchannels that promote rapid ion insertion, facile electrolyte transport, and favorable SEI formation.[59]

The electrolyte composition has a larger impact on the SEI than any other part of the battery, and many different chemistries are being explored. Ester- and ether-based solvents are most-commonly used, such as cyclic propylene carbonate (PC) and ethylene carbonate (EC), as well as linear dimethyl carbonate (DMC), ethyl methyl carbonate (EMC), and diethyl carbonate (DEC) (chemical structures shown in **Figure 2**). Glymes and crown ethers are also being investigated for use in SIBs.[60–62] Preferred electrolyte properties include low viscosity, a wide electrochemical stability range, and high ionic conductivity. Ester-based solvents tend to produce thicker and less-uniform SEIs compared to ethers but are still preferred due to their lower viscosity and higher conductivity. Binary,[44,63] or less frequently, ternary[64,65] mixtures of cyclic and linear esters are often used in order to further improve viscosity and transport. The thermal stability of the

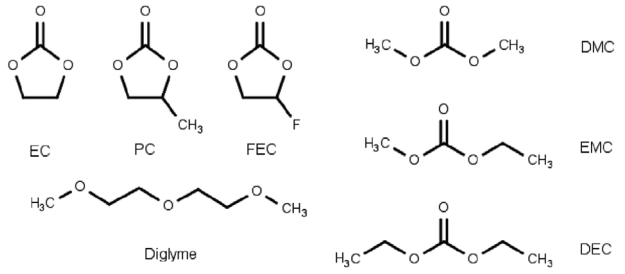

Figure 2. Chemical structures of typical electrolyte solvents used in SIBs.

electrolyte must also correspond to the specific application. Excessive temperatures or improper charging of the cell can lead to solvent decomposition, gas formation, and irreversible cell damage.[6]

The conductive salts used in SIBs are typically sodium analogs of well-established salts used in LIBs (such as $NaClO_4$, $NaPF_6$, NaTFSI, shown in **Figure 3**). The ionic conductivity and electrode (de)insertion behavior are strongly dependent on the interaction between the charge carrying cation and the anionic species. The mobility of the anions is considered quasi-stationary due to their larger radii compared to Na^+, whereas the mobility of Na^+ ions is influenced by the "closed shell" interaction with the solvent.[66] $NaClO_4$ and $NaPF_6$ are currently the most promising electrolytes for SIBs, however, they pose some safety concerns, and other salts are being explored.[6] These alternative salts exhibit additional challenges; NaTFSI, for example, is corrosive and degrades the aluminum current collector, while other salts simply do not provide satisfactory performance, e.g., in terms of ionic conductivity.[66,67]

Much work is dedicated to gaining insights about the decomposition mechanisms and products of common solvents, salts, and additives, to understand the species that make up the SEI. The SEI typically consists of inorganic species, such as NaCl, NaF, Na_2CO_3, Na_2O, NaOH,[18,25,42,66,68] and organic species, such as Na-ethylene dicarbonate (NaEDC), and Na-ethylene glycol (NEG).[43] The exact composition and structure of the SEI varies depending on the specific system chemistry, and the composition and structural features are still not fully understood even for individual systems.[69]

Electrolyte additives have been introduced as a possible way to stabilize against electrochemical decomposition and to selectively modify the SEI. Several studies have investigated fluoroethylene carbonate (FEC) as additive but have observed mixed results. FEC appears to improve the stability of the SEI[43] to the degree that it remains intact even when the electrolyte is replaced with an additive-free solution.[64,70] Others argue that FEC increases the polarizability and instability of the cell, and that the polarizability and instability of the cell costs outweighs the benefits of the stronger SEI.[71] Different effects of FEC are observed in full-cells versus half-cells for the same chemistry, which highlights the interconnectedness of all of the cell components.[72] Other additives such as difluoro ethylene carbonate (DFEC), ethylene sulfite (ES), and vinylene carbonate (VC) have been excluded from further investigations due to inadequate stability or reduced cell capacity.[25]

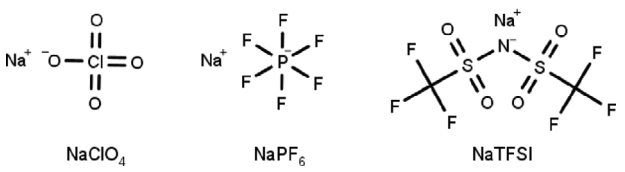

Figure 3. Common conductive salts applied in SIBs.

The significant influence of the electrolyte solution on the physical and chemical properties of the SEI is evident from their distinct compositions. SIMS and XPS measurements on SEIs formed in different electrolytes reveal different components. Komaba et al. conducted SIMS measurements on SEIs formed under otherwise identical conditions, with the only difference being the cation (Na^+/Li^+). They attributed the same role of a protective passivation layer to both SEIs, with the sodium-based SEI containing a higher proportion of inorganic species due to its thinner nature.[25] Consistent with this finding, Carboni et al. identified Na_2CO_3 as the main component in the SEI formed using an electrolyte consisting of NaTFSI in PC with the additive FEC. Pan et al. predominantly found sodium ethylene dicarbonate (SEDC) in the SEI formed using $NaPF_6$ in the solvent mixture of EC:DEC (1:1).[73] Oltean et al. also reported a significantly thinner sodium-based SEI from EC:DEC (1:1.5), where the proportion of inorganic compounds also outweighed that of a lithium-based SEI from EC:DMC (1:1), which mainly consists of organic compounds. Similar results were previously obtained by Komaba et al. for SEIs from PC electrolyte for both Na- and Li-ion battery cells.[25,74] Hirsh et al. identified the main constituents of a SEI formed in PC (1 M $NaPF_6$) as Na-alkyl carbonates, polyesters, hydroxides, NaF, and Na_2O,[68] which aligns well with similar results from Huang et al.[66] and Carboni et al.[42] All these observed compositions are chemically similar to those found in LIBs. It must be considered, however, that SEI components of SIBs are more soluble and less stable than their lithium analogues. The solubility of SEI components significantly influences the chemical composition and physical properties beyond the first cycle. NaF and Na_2CO_3 are 20–50 times more soluble in common ester solvents than LiF and Li_2CO_3, respectively. This difference is likely to be even more pronounced for organic SEI components and one of the primary reasons for the observed SEI stability difference between LIBs and SIBs. As the SEI dissolves over time, recurrent electrolyte degradation reactions take place at the thinner and poorly passivated electrode interface, leading to irreversible capacity loss via unchecked consumption of Na^+. The exact mechanism of this dissolution and degradation is still unclear, and is the subject of current investigations.[6,33,75,76]

Other studies work to develop an understanding of the SEI on a more fundamental level, such as determining the formation and degradation mechanisms, and the specific that properties correspond to improved cell performance. There is a loose consensus on the thinness of the SEI in ester-based SIBs, although absolute values vary due to the absence of binder or Na_xC signals in XPS measurements. Values ranging from 10 to 50 nm have been reported.[42,73] Hirsh et al. used CV measurements to argue that the low values of ICE depend on the presence of partially reversibly bound sodium components in the SEI.[68] Rangom et al. observed different cycling behaviors in cells subjected to different first charge and discharge rates.[77] This difference was determined to be caused by changes in the initial formation of the SEI,

however, XPS measurements did not reveal any chemical differences in the formed SEIs. They attributed the different cell responses regarding electronic and ionic impedance, as well as capacitance to variations in SEI thickness, density, and microstructure. They also observed an inverse relationship between charge rate and volumetric expansion of the SEI, such that the thinnest and most stable SEI with the lowest impedance was formed at the highest tested charge rate. Bommier et al. proposed the hypothesis of a SEI growing towards the anode, which they argued was not responsible for capacity loss. They attributed the capacity reduction to the degradation of the electrolyte at the sodium-metal counter electrode and the passivation of the counter electrode itself.[78] Similarly, Cresce et al. determined a reduced role of solvated Na^+ ions in SEI formation in SIB.[79]

There are many scientific papers published every year describing the SEI in SIBs. Most of which only focus on single, isolated, parts of the battery, missing the complex and interconnected influence of the entire cell on the phenomena that occur on the anode surface. Moreover, these studies are carried out with different HC samples and cell setups, which restricts comparison between studies and generates conflicting ideas. A comprehensive understanding of the reactions involved in the formation and evolution of the SEI during cell assembly, cycling and storage must be developed.[18,31,39]

In this perspective, we present experimental and computational methods, which, from our point of view, are essential for the development of a complete understanding of SIB performance. We seek to emphasize that, while these methods are invaluable on their own, unified, multiscale studies, with consistent materials, are needed in order to provide a clear and comprehensive picture of the processes that occur inside SIBs.

3. Analytical Methods

In this section, we will discuss several analytical methods used for battery research, loosely in order of scale, beginning with full-scale and operando techniques.

The individual analytical methods used to study SIBs are largely similar to those used for LIBs. With the exception of Nuclear Magnetic Resonance and X-ray based techniques, which will be discussed in more detail in their respective sections, very few changes need to be made to the system setups and operation. The largest difference between SIBs and LIBs in regard to analytical methods is the relative benefit of integrating multiple techniques into single studies.[80] The robust and consistent behavior of LIBs allows for clear and accurate studies using individual isolated techniques. In contrast, the sensitivity of SIB cell behavior to small changes in the cell, and to the influence of processes at many different size- and timescales, means that single techniques often do not provide a clear understanding of the cell properties and phenomena. Integrated multiscale approaches consisting of multiple techniques are required to elucidate these behaviors.

3.1. Differential/Online Electrochemical Mass Spectrometry (DEMS/OEMS)

DEMS and OEMS both describe in situ/operando methods that use mass spectrometry to analyze the gases that evolve during electrochemical processes.[81–83] DEMS and OEMS are often used interchangeably, but have differ slightly in regard to setup and data collection. The main difference of the two is that OEMS does not allow for instantaneous (differential) gas detection when applying a voltage or current, but instead has a delay in time. Previous studies in the area of batteries have focused on SEI formation and cell degradation studies, primarily on LIBs, and only recently on SIB/HC chemistries.

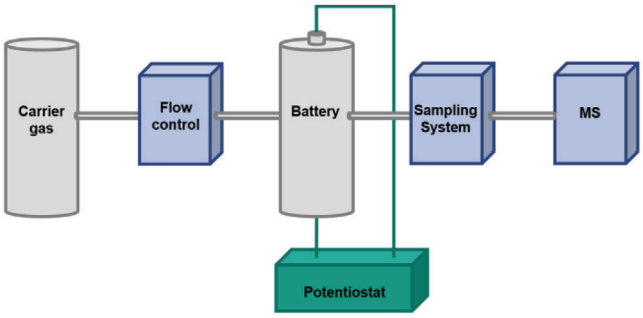

Figure 4. Schematic of a generalized OEMS setup with bypass containing a carrier gas. Not all setups include a sampling system.

DEMS can be realized by probing the gas in direct proximity of the electrode by attaching a gas-permeable membrane directly to a porous electrode. For aqueous electrolytes, a hydrophobic membrane is usable for this purpose. For organic electrolytes such membranes are not applicable, because the organic solvents in batteries can diffuse through the membrane and drain from the cell, which alters the behavior of the battery. Other sampling methods were developed for such batteries in order to counteract this problem, such as probing the gases using valves to extract samples from a head space above the battery. A continuously operated OEMS for batteries may also be achieved by allowing the evolving gas to enter a bypassing stream that contains a carrier gas. A general schematic of the OEMS setup is shown in **Figure 4**.

All setups consist of a potentiostat for electrochemical cycling/monitoring, often combined with EIS measurements, and sometimes thermal controls. The gas flow in OEMS systems with bypass is generally realized by an argon gas carrier stream which transports the product gas stream from the battery cell to the mass spectrometer. The stream is regulated by valves in order to prevent significant drying of the cell during periodic probing.

OEMS setups have been reported in literature to investigate different-sized battery cells. Experimental small-scale setups for coin-sized cells have been developed by academical facilities, as well as commercial suppliers, for the investigation of materials at coin cell size. Other groups have reported inserting a gas draining system into commercial cell formats like cylindrical and pouch cells.[84,85]

The recorded intensities of the mass-to-charge ratios m/z can be associated with the spectra of the product gasses. However, most mass spectrometers do not have sufficient mass resolving power to differentiate between species with similar masses. One example for this is the common formation gases C_2H_4 and CO when EC electrolytes are used. In this case, other m/z-values of the molecular fragments are used for the identification and quantification of these species.[82] Still, the unambiguous

identification of unique decomposition fragments of the product gases for quantification remains challenging.

In mass spectrometry, quantification of the gas amounts is often coupled to complex calibration protocols, which must be performed frequently. Not all setups fully transport all evolving gasses into the mass spectrometer, furthermore, the ion current signal of the MS may drift over time. The overall number of species tracked in a given test, including both whole molecules and fragments, is limited due to sampling time constraints. Internal references of the carrier gas and calibration gases, with regulated species concentrations and flows, are used for precise quantification.[83] This quantification protocol must be performed for every product species observed. This raises general maintenance and calibration expense for mass spectrometry.

The analysis and identification of the reaction mechanisms leading to the gas formation can be challenging, as the only information obtained is the composition of the product gases. Gases like CO and CO_2 can be produced from solvent decomposition at the electrodes, or also from decomposition of the salt, electrode, or separator materials. Modifying the experimental design can help to distinguish between the different sources, but when electrodes are varied, new interactions with other components are also observed.[82]

OEMS measurements of sodium|graphite half cells by Goktas et al. using ether electrolytes have shown gas evolution during equilibration and the first cycle.[86] Equilibration before cycling showed development of CO, which is attributed to reactions with the sodium electrode. During the first cycle, CO, CH_4, H_2, C_2H_6 and C_2H_4 were observed. However, in TEM measurements no SEI was found, indicating that the gas did not stem from solvent decomposition to typical SEI products.

The gas development is therefore attributed to electrode surface impurities. The electrolyte is assumed not to form an SEI at all, leading to the assumption of an SEI-free battery in ether systems.

Zhang et al. investigated the gas evolution in SIBs with different anode, cathode, and electrolyte chemistries using half- and full-cell setups with carbonate electrolyte.[87] Their results support the hypotheses that there are multiple degradation mechanisms of electrolyte and additives. They also identified how Na-metal electrodes and different types of cathode material impacts gas evolution. Further studies also examined cathode gassing in layered oxides and Prussian blue analogues.[82,88]

In our own studies, the formation of HC//sodium-vanadium-phosphate (NVP) cells with 1 M $NaPF_6$ in EC:PC (1:1) electrolyte has been investigated. Preliminary results, shown in **Figure 5**, indicate that most reactions only take place in the first cycle, whereas hydrogen production continues in the subsequent cycles.

In conclusion, OEMS enables essential insights into gas-producing degradation reactions at HC/electrolyte interfaces of SIBs; gas evolution can be quantified during operando measurements and correlated to operating conditions, as well as electrode and electrolyte design. More OEMS studies are needed in order to determine the degradation rates and mechanisms of the electrolyte and electrode interface in SIBs quantitatively and uniquely.

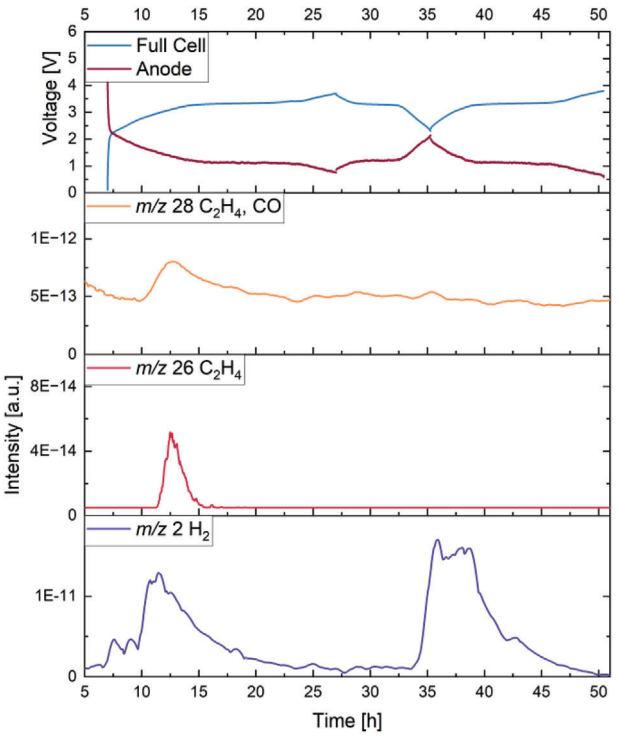

Figure 5. Example of an OEMS measurement. Baseline subtracted. Small peaks can be attributed to measurement artefacts. The measurement was conducted with a cell chemistry of HC|NVP 1 M $NaPF_6$ in EC:PC (1:1). Hydrogen development can be observed during the first and second cycle, while ethene at *m/z* 26 can only be observed in the first cycle. Since *m/z* 28 can indicate both ethene and CO, it is not clear whether CO is formed or the ethene is causing the peak.

3.2. Electrochemical Impedance Spectroscopy (EIS)

Electrochemical impedance spectroscopy techniques are an integral part of many cycling protocols to expand on the information that is gained from (mostly galvanostatic) cycling experiments in battery cell tests. EIS offers a noninvasive means to study electrode processes and derive (in theory) individual contributions of the cell resistance. The aim of the technique is to pinpoint bottlenecks in the charge-transfer and mass transport processes during the cell reaction. However, the complexity to work out such parameters unambiguously in a typical thin-layer battery setup (coin or pouch-cell formats) is often underestimated.

EIS probes an electrochemical system using a periodic voltage perturbation signal with a small amplitude over a range of frequencies. EIS is thus an alternating current (AC) method, in which the system is supposed to oscillate around an equilibrium state, inducing reversible, but no irreversible, changes. The potential changes display linear current–overpotential relationships (i–η)[89] for amplitudes smaller than a few tens of mV (typically <20 mV). The application of current perturbations is also possible. However, the amplitude in this case is specific to the capacity of the system. EIS can be extended to study the characteristic nonlinear i–η behavior at electrode/electrolyte interfaces by applying larger amplitudes (in case of E-perturbations). This is referred to as nonlinear frequency response analysis and is highly surface

sensitive. It may be used, e.g., to distinguish between SEI- and plating-related aging of Li-ion batteries.[90]

Impedance (Z) is the opposition to alternating current and the result of the combined effect of resistance and reactance in an electrical circuit. Resistance (R) represents the dissipation of heat (energy loss) and is frequency independent. Reactance (X) is a frequency-dependent response in AC circuits from inductors and capacitors. For capacitors, reactance stores energy and returns it into the circuit a quarter-cycle later, causing both a shift in phase angle and (frequency dependent) change in amplitude with respect to the input signal. The impedance, $Z(\omega)$, is defined as the vector sum of real (Z') and imaginary (Z'') contributions of the circuit components. Impedances of series or parallel circuit configurations follow Kirchhoff's current law. Because the three properties, resistance, capacitance C, and inductance L, respond differently to alternating currents, impedance spectroscopy enables conclusions about the components of electrical circuits, based on changes in amplitude and phase shifts with frequency.

EIS measurements are often paired with models in order to help extract battery parameters and estimate the state of battery (degradation):[91] Equivalent circuit models attempt to translate the response from an electrochemical system into known electrical circuit components. A simple example is provided in **Figure 6a**, for a hexacyanoferrate redox couple in aqueous solution at a Pt electrode. The electrode process can be expressed in a so-called Randles circuit (Figure 6a, inset). In this representation, Faradaic processes are expressed as a resistor (charge-transfer, R_{ct}), non-Faradaic processes, like the electrochemical double layer, are expressed as capacitors (e.g. C_{dl}) and diffusion processes, such as solid-state diffusion in an active material and mass-transport in the electrolyte in batteries, are represented with the so-called Warburg impedance (W or Z_W).[92] Hence, there can be clear physical connections between basic elements and processes. More complex and accurate models are being developed and will be discussed in Section 4.

We wish to emphasize some fundamental details about Nyquist plots (Figure 6a), as they are often displayed incorrectly in literature. In these plots, Z' and Z'' of $Z(\omega)$ are plotted in the complex-plane for each frequency. The distance from the origin of the complex plane to the data point is the absolute value of $Z(\omega)$. Note that for a semicircle to appear as a semicircle, the axes in Nyquist plots must be plotted orthonormal (not only the tick labels but the actual plot width and height). Though this information is trivial, it is frequently ignored in literature. Nyquist plots contain frequency information indirectly, as each data point represents the impedance at a given frequency. However, this complicates the comparison of different samples, as different data series can be easily shifted in the frequency domain while displaying similar impedance values. Therefore, it is good practice to label characteristic frequencies in a Nyquist plot or provide the corresponding Bode plots. The Bode representation offers a means to plot $|Z|$, Z', Z'', or the phase angle φ, as a function of frequency (Figure 6b) and is a useful addition when presenting EIS data. Bode plots are more suited to demonstrate that simulated impedance spectra fit the experimental data not only in magnitude, but also fall in the correct frequency domain.

The strength of EIS lies in the possibility to separate electrode processes on different time scales, ranging from a few

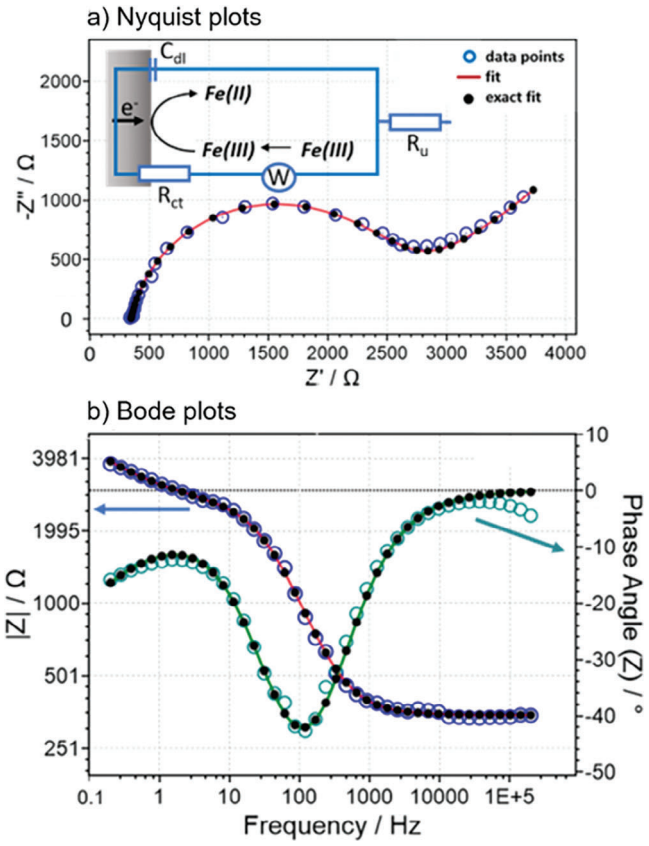

Figure 6. EIS spectrum of hexacyanoferrate redox couple in 10×10^{-3} M K_2SO_4 aqueous solution at a Pt-electrode. Experimental data is shown as empty circles; fitted data as solid line with black dots. a) Nyquist plot with inset of electrode process and rationalization of equivalent circuit model. b) corresponding Bode plots for $|Z|$ and phase angle versus frequency.

mHz to several MHz. For example, charge redistribution in the electrochemical double layer occurs on faster time scale than electrode reactions which, in turn, occur faster than associated mass transport processes. EIS is applied to answer a large variety of scientific questions in battery research. On a material research level, EIS is used to investigate aging of electrode materials, formation and resistivity of surface layers, and questions related to the charge-transfer process. As studies are mostly done on composite electrodes, EIS spectra also contain information about electrode porosity. The complexity of EIS spectra in 2-electrode systems is high, as spectra are superpositions of signatures from both the negative and positive electrodes (and the electrolyte), especially if porous electrodes are studied. Although the use of half-cell configurations simplifies the interpretation, metallic counter electrodes, such as Li foil, age during storage and cycling, and thus display different signatures in EIS spectra depending on their cycling history. This problem is amplified in post-Li batteries that use more reactive alkali metals, like Na or K.[93] In case of the latter, contributions from the working electrode may be masked or obscured by the high impedance of the counter electrode. 3-electrode setups help to single out contributions of cell components but require reliable reference electrodes.[94]

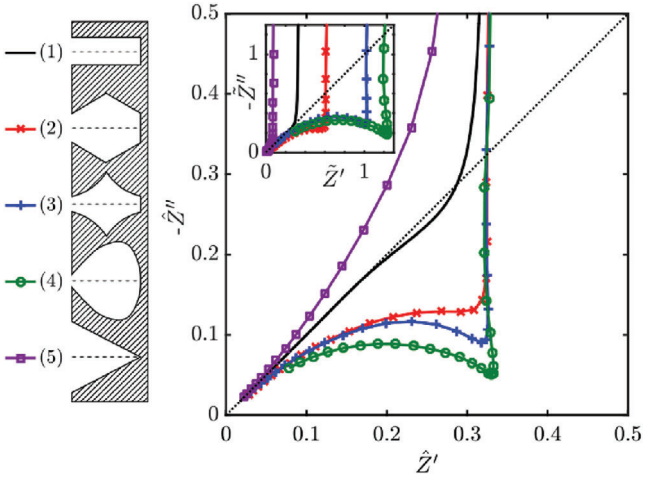

Figure 7. Simulated impedance spectra of 3D recreations of different pore geometries. Reproduced under terms of the CC-BY license.[100] Copyright 2017, Cooper et al. Elsevier Ltd.

The choice of cell setup has a profound impact on the acquired data. For example, electrode misalignment, and even the symmetry and position of the reference electrode with respect to working and counter electrode, influence the resulting EIS spectra.[95–97] In many battery-related studies, interpretations of EIS spectra are carried out by comparing spectra of different samples. Because of the complexity of porous electrodes, commonly used equivalent circuit models, such as the Randles circuit, are insufficient to describe all electrode processes, as well as charge and mass transport in particle networks. Electrical circuits are not unique, and therefore the goodness-of-fit to acquired data does not validate models unambiguously. In this context, the Gaberšček group coined the term "arbitrary (equivalent) circuit"[98,99] for series circuits with multiple Voigt-elements (parallel circuits with a capacitor in one branch and a resistor in the other), as these models may carry little-to-no physical meaning. Physics-based models, on the other hand, can provide a sound phenomenological basis for derived parameters, but are often not straightforward to implement in EIS fitting software for occasional EIS users. In the analysis of EIS spectra, it is a challenge that processes, i.e., their relaxation times, may overlap strongly, and thus not appear as individual semicircles in the spectrum, but rather create a merged (superimposed) arc that closely resemble semicircles. In fact, composite electrodes often show features originating from electrode porosity that appear as distorted semicircles that might be misinterpreted as electrode processes[100] (**Figure 7**). Such ambiguous spectra can only be resolved by changing measurement conditions, for example by varying the temperature (change charge-transfer kinetics), changing the electrolyte concentration (change mass transport properties/electrolyte conductivity),[101] applying different stack pressure (reduce contact resistance)[102] or replacing the electrolyte salt with redox-inactive compounds[103] in order to "turn-off," mask or overexaggerate certain processes.

Hence, even though setting up EIS measurements is easy, acquiring reliable data and going through the process of understanding the individual features and the dominating parameters in EIS spectra requires more time and effort than many reports appear to be willing to invest.

In two recent works, Linsenmann et al.[94,104] first developed a microreference electrode based on partly sodiated tin wire in order to investigate electrode pore resistance in pristine HC//Na 3-electrode half-cells, from which tortuosity values can be derived. The authors used the 3-electrode setup to track the evolution of cell impedance with state-of-charge (SOC) on the first cycle, i.e., at different stages of SEI formation and sodiation of the HC electrode. To account for porosity effects, the authors fitted their data with a transmission line model. Compared to a corresponding HC//Li half-cell, the electrode resistance was 4–5 times higher and at 100% SOC (end of charge) the charge-transfer resistance, R_{ct}, derived from fitted spectra was found to be about 10 times larger for the Na half-cell than for the Li half-cell. The example demonstrates the potential of EIS in the evaluation of cell characteristics and as a non-invasive technique to analyse SOC, state-of-health, but also useful physicochemical properties of the electrochemical system.

3.3. Operando Stress Measurements Using Substrate Curvature

Almost all physical and chemical processes that occur in a solid alter its mechanical stresses. Stress measurements can therefore be used to investigate the fundamental mechanisms that occur in the material. The substrate curvature technique allows to measure stresses in thin layers and at interfaces with extremely high resolution. Today this technique is used in many fields for quantifying stresses and ensuring reliability of devices, for example, in the microelectronics industry (wafer curvature). In the early 20th century Stoney[105] used the curvature of a substrate to determine stresses that are associated with electroplating. This allowed him to develop the following relation:

$$\sigma_f \approx \frac{E_S h_S^2}{6 h_f \left(1 - \nu_S\right)} \frac{1}{R} \tag{1}$$

For films that are much thinner than their substrate ($h_f \ll h_S$) the stress σ_f is inversely proportional to the radius of curvature R. The processes under investigation cause equibiaxial stresses in the film and deform the film-substrate-laminate into the shape of a shell of a sphere. Knowledge of the mechanical properties of the film is not required since the proportionality constant only contains elastic mechanical parameters of the ceramic substrate (E_S, ν_S). The stress-thickness product $\sigma_f \cdot h_f$ is the force acting per unit length at the film–substrate interface. It can be used instead of σ_f when h_f is not known or when surface or interface mechanisms are of interest.

Nowadays, the curvature is measured by reflected laser beam(s). The beams hit a cantilever distant from the clamp that holds the film inside the test cell. The curvature of the cantilever between the laser spots can be determined, by tracking the position of the reflected laser beams with a pixel detector and using a simple geometry (**Figure 8**). The presence of an electrolyte and its refractive index affects the laser deflection. The non-linearity in the law of refraction can complicate these measurements. If the setup can be designed in a way that the outgoing laser beam is approximately perpendicular to the window of the test cell, the

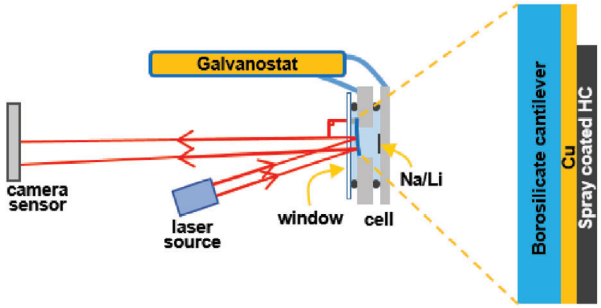

Figure 8. An electrochemical test cell inside a substrate curvature setup.

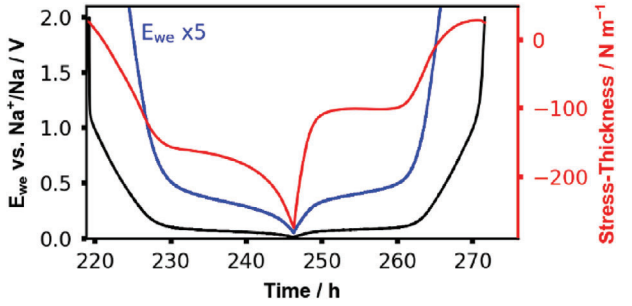

Figure 9. Stress-thickness and electrochemical potential of the 5th cycle of hard carbon (spray coated on a cantilever) cycled in 1 M $NaPF_6$ in EC/PC 1:1 with 10 mA g^{-1}.

deflection is linearly dependent on the refractive index.[106] Equation 1 is only valid for thin films, for thicker electrodes, deviations must be expected, and the mechanical properties of the film affect the radius of curvature. This is a concern for electrodes of real batteries, in particular, and assumptions need to be made how the curvature can be related to stress and/or volume changes of the electrode.[106]

In battery research, substrate curvature has been used to monitor stresses during electrode operation. A correlation of electrochemical and mechanical data as obtained by substrate curvature is then used to investigate fundamental electrochemical processes. On the one hand, the measured electrode potential of an electrode (relative to the counter electrode) originates from its interface with the electrolyte, i.e., it can be considered as an information from the electrode surface. On the other hand, the mechanical stress originates from both, the interface, and the volume of the electrode. For electrodes with finite thickness, the volume expansion and contraction typically dominate, so that stress data is complementary to the simultaneously recorded potential of the electrode.

With its high sensitivity, the substrate curvature technique is able to observe the volume expansion of zero-strain electrodes with high resolution[106] and can detect processes at interfaces, for example, the deposition of fractions of monolayers of atoms.[107] Detailed reviews of the technique[108] and its application to batteries[109,110] have been published. The technique has been mainly used for anode materials, but applications for cathode materials can also be found in the literature. So far, the focus was clearly based on lithium-ion batteries and only limited data exists on post-lithium systems.[111,112] Thoroughly investigated lithium-based anode materials include lithium titanate (LTO),[106] silicon,[113] germanium,[114] and aluminum.[115] Research on cathodes includes layered oxides for lithium-ion batteries[116] and the olivine $FePO_4$.[111] The latter describes a special case; in this work, lithium was exchanged by sodium in the same electrode and the change in the mechanical stresses during cycling were used to infer reaction pathways, including phase transformations, which differ significantly for both insertion ions.

Figure 9 shows the electrochemical potential versus Na^+/Na and the measured stress-thickness product of a characteristic cycle of a cantilever that was spray coated with HC. While the electrochemical potential is almost symmetrical between charge and discharge, large differences are apparent in the stress-thickness curves. Stresses at the plateau voltage are more compressive during sodium insertion than during extraction. This indicates that the storage process is less symmetrical than expected according to electrochemical data. Within a cycle, irreversible mechanical work is performed in the HC. During extraction, the stress is less dependent on the sodium content (plateau in stress thickness); it remains constant while the electrode changes its volume. This suggests that force-controlled processes are active. This bears resemblance with plastic deformation where the generation and motion of crystalline defects cause changes in shape or volume. Additional investigation of the temperature and rate dependence is required and will help to better understand the sodium storage mechanism of HC.

3.4. Time-of-Flight Secondary Ion Mass Spectrometry (ToF-SIMS)

ToF-SIMS is a surface sensitive mass spectrometric method for the layered 3D analysis of solid materials[117,118] that is able to obtain information about the lateral- and depth distribution of elements and fragments of chemical compounds. In the often-used dual beam approach, a liquid metal ion gun (LMIG, **Figure 10**a) is used to ballistically impact a surface with a low current, highly focused, pulsed primary ion (PI) beam. This impact

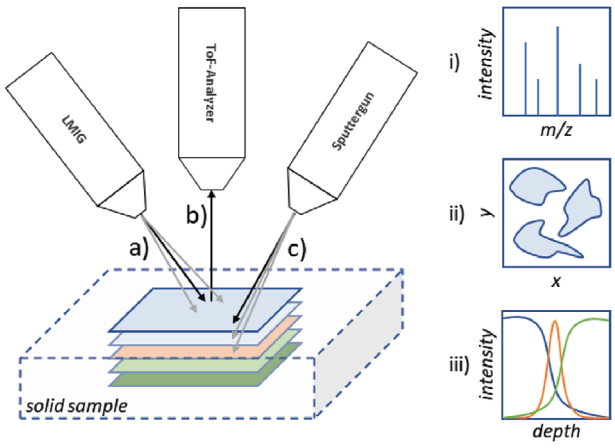

Figure 10. Schematics of a ToF-SIMS measurement setup with a) the LMIG, b) the ToF-analyzer and c) the sputter gun. For each pixel a mass spectrum (i) is obtained. Images (ii) can be formed by highly focusing the PI beam. Alternated usage of the LMIG and the sputter gun leads to profiles (iii) showing the depth distribution of the detected fragments.

causes molecular fragmentation and the emission of secondary ions (SI) of both polarities from the surface. Either cations or anions are collected via an electrical field and transferred in a mass analyzer. In state of the art time-of-flight mass analyzers (Figure 10b), the fragments are separated and distinguished with a mass resolution of up to $m/\Delta m > 28{,}000$, while the lateral resolution of the scanning PI beam goes down to <50 nm. Secondary electrons are also produced during SI generation and can be used for electron microscopy with a lateral resolution <40 nm.

Regions below the surface can be cleaved for analysis by applying a high current beam from an additional low energetic sputter gun (Figure 10c), which etches into the sample at micron-range depths. Charge accumulation on the surfaces of electrically insulating materials is avoided by using a low energy electron gun. A focused ion beam (FIB) milling option for cross-sectional imaging and tomography is also applicable.

For pulsed PI sources, surface roughness impairs the mass resolution of the time-of-flight analyzer, as fragments emerging from different heights exhibit slightly different flight times, increasing the width of corresponding peaks. Ultrahigh vacuum conditions are essential to impede collisions between the pulsed/secondary ions and gaseous particles. Volatile and highly amorphic, "soft" samples may be analyzed under cryogenic conditions, for which a liquid nitrogen-cooled sample stage can be provided.

Information gathered from this method consists of mass spectra for pixels (2D) or voxels (3D). The former is usually displayed as mass spectra or 2D images showing the lateral distribution of chemical fragments. The latter is mostly displayed as graphs, called depth profiles, or as 3D distribution cuboids that take the lateral information of each layer into consideration.

A major advantage of the technique is its superior sensitivity due to the high transmission of SIs in combination with single ion counting detectors, which allows for detection limits up to ppb range. Usage of larger PI species or clusters from a gas cluster ion beam (GCIB), such as Ar_{1500}^{+}, allows for the ionization of large fragments of weights up to 12,000 u, which tends to be a limitation for organic molecules. Organic SIs of this size require an orbitrap analyzer with a resolution of $m/\Delta m > 240{,}000$ @ m/z 200 possibly in combination with tandem mass spectrometry to be distinguished unambiguously.

The area of analysis can be extended beyond the reach of the PI grid (usually about 500×500 μm^2), by moving the sample stage. This effectively takes multiple measurements in a grid, at the borders of previous measurements, and digitally stitches several measurement fields together.

A disadvantage of this method is its high fragmentation rate for molecules during the collision cascade with the PIs. This complicates the data analysis. In this connection multivariate analysis methods allow for the identification of significant variables, thereby reducing the complexity of the mass spectrometric information. PCA (principal component analysis) or MCR (multivariate curve resolution) can be used to show differences between samples in terms of mass spectra and within depth profiles. More detailed information about the application of ToF-SIMS in battery research, its advantages, limitations and best practice is given in a recently published article by Lombardo et al.[119]

Understanding interfacial behavior and the interphase formation process is crucial for the development of battery-cells and energy storage devices. The SEIs in SIBs and LIBs have thicknesses in the order of 10 nm, and require surface sensitive equipment, like ToF-SIMS, to be analyzed, as the layers are too thin to be easily examined with other methods.[68]

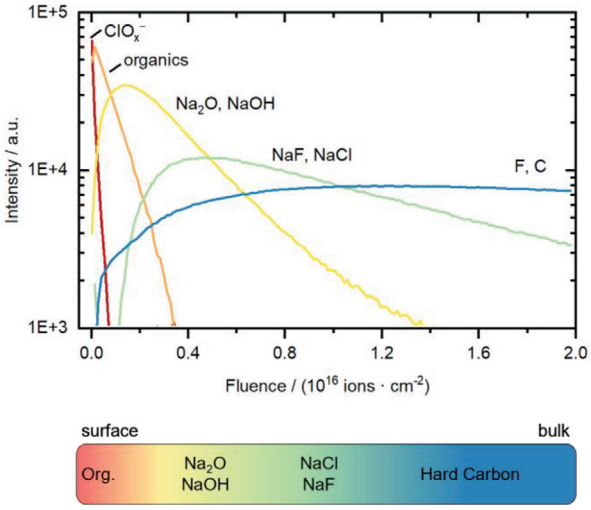

Figure 11. Top: 5 factor MCR-Analysis of a ToF-SIMS depth profile of the SEI on a Hard Carbon electrode from a sodium-ion battery. Bottom: graphical depiction of the results above.

A depth profile MCR analysis of the SEI formed in a SIB cell after 20 cycles on HC is shown exemplarily in **Figure 11**. The relative intensity and fluence of the various fragment profiles reveals a clear layered structure of the SEI. Sublayers of sodium oxide and hydroxide are formed on top of a halide salt layer, which is covering the bulk material.[46] Some fluorine signals show broader in-depth distributions, hence its signature in the bulk. Chlorine oxides on the surface may be residues of the $NaClO_4$ conducting salt, while the outermost organic layer consists of decomposition products of the electrolyte solvent, as shown by XPS measurements.[68]

The groups of Komaba[25] and Lust[120] have conducted ToF-SIMS measurements on the SEI in SIBs at HC anodes. The interaction and reaction products between the solvent and a sodium salt, such as $NaClO_4$ or $NaPF_6$, exhibit different behavior compared to their corresponding lithium salts. The difference is that the SEI in SIBs consists mainly of inorganic salts, including: Na_2O, NaOH, NaCl, NaF, Na_2CO_3 and Na_xPO_y. The SEI in LIBs, on the other hand, consists primarily of organic species.

3.5. X-Ray Photoelectron Spectroscopy (XPS)

XPS is a surface-sensitive characterization technique that is able to study the composition, chemical bonding, and electronic structure of surfaces and interfaces.[121] Inside a photoelectron spectrometer, typically operated at ultra-high vacuum, a (monochromatic) X-ray beam irradiates the surface of a sample with photons. If the incident photon energy ($h\nu$) is larger than the electron binding energy E_B, the impact causes the emission of photoelectrons (schematically depicted in **Figure 12**) from core and valence levels of near-surface atoms to the vacuum level. Any excess energy is transferred to the electrons as kinetic energy E_K.

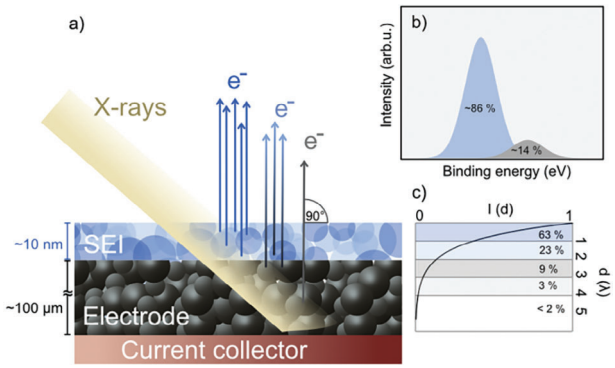

Figure 12. a) Schematic representation of the photoemission process from a cycled battery electrode with SEI. b,c) Show the approximate intensity I distribution for the resulting photoelectron signal from such an idealized layered sample in dependence of the inelastic mean free path λ of the photoelectrons in the material.

E_K is measured using an electron analyzer and allows for the calculation of the electrons' binding energy using Equation 2, where ϕ is the spectrometer work function.

$$E_B = h\nu - E_K - \phi \quad (2)$$

The photoelectron binding energy is specific for each element, and thus allows for the qualitative determination of the elementary composition. Moreover, the binding energy depends on the oxidation state and bonding environment of the atoms or molecules; changes in binding energy resulting from these environments are known as chemical shifts.[121] The peak intensity, i.e., the area under the peak, is directly proportional to the concentration of atoms of a given element and provides quantitative information about the surface chemistry.

The surface sensitivity of XPS stems from the strong interaction between photoelectrons and the sample.[122] Only electrons that leave the sample without losing energy (i.e., without inelastic scattering) contribute to the characteristic photoemission peaks. The probability for an electron to escape the sample surface without energy loss decreases exponentially as a function of the electron emission pathway and its inelastic mean free path λ (see Figure 12c). Thus, most of the signal stems from near-surface regions (see Figure 12b); the information depth is typically set to 3 λ, as this corresponds to 95% of the signal intensity for vertical electron emission. λ is dependent on both the composition of the sample material and the incident photoelectron kinetic energy. This energy dependence can be harnessed to achieve essentially nondestructive depth profiling by using synchrotrons to tune the incoming photon energy in order to change the kinetic energy of the electrons. Furthermore, the surface sensitivity can be enhanced using smaller electron take-off angles (grazing emission). However, the obtained data is always a weighted average of the entire probed volume, with the largest fraction of the signal intensity stemming from the region nearest to the surface. Evaluation of the depth-dependent composition of the near-surface region therefore requires an extensive data set that is rarely available. Quantitative analysis of atomic concentrations in the near-surface region, with the help of atomic sensitivity (ASF) factors,[121] is even more cumbersome because of the different kinetic energies, and thus different λ values, of the respective photoelectrons. For a more detailed review of photoelectron spectroscopy in battery research, the reader is referred to ref. [123]

XPS has become an indispensable tool in battery and SEI research; research groups use laboratory and synchrotron-based XPS to characterize SEI layers in Li-ion batteries based on the methods outlined in the seminal work from Peled and Edström.[124–126] This is partly due to surface sensitivity. With λ in the order of 3–4 nm for soft and carbonaceous materials,[118] using an Al K_α X-ray source, the information depth in XPS is of the order of 10 nm, and thus is ideally suited to study surface and interfacial layers in batteries, which typically have thicknesses in the same range. The thickness of the SEI layer can be estimated via bulk signal attenuation by tuning the excitation energy in such a way that a signal from the underlying bulk electrode can still be detected.[126]

The chemical shifts due to changes in oxidation state and bonding environment allow for detailed analysis of SEI components, as well as the effects of sodiation. Relative peak shifts between the surface layer and the bulk electrode material provide further information on the electronic properties of the interface.[127,128] The chemical evaluation is reasonably straightforward for simple binary compounds, such as NaF or well-known molecular species, but can be challenging for more complex species, as exact binding energies of the various decomposition products in the SEI are mostly unknown. A detailed analysis should also consider the fixed ratio of the different elements in a given molecular moiety, as given by its stoichiometry. As a result, because of the complexity of the evaluation, detailed analyses of the molecular composition of the SEI, also including the decomposition products, are highly challenging and scarce. Furthermore, they are at best semi-quantitative, assuming a homogeneous lateral composition and neglecting local variations therein. In summary, a complete quantitative elemental and molecular analysis of the SEI layer and its depth dependent composition, even though theoretically feasible, is essentially impossible at present and would require a huge data set. Combination with AI based evaluation schemes may also become helpful in future.

More information on the molecular composition of the SEI may be obtained by comparing experimental binding energies with calculated ones, using the states of all elements within a potential decomposition product.[129,130] Despite the large overlap in some signals, e.g., because of similar functional groups, other elemental peaks may show distinct differences, which eventually may allow to discriminate between different decomposition products.

In HC-based Na-ion batteries, XPS has mainly contributed to the understanding of SEI formation, composition, and stability. Early work by Dahbi et al. describes the initial SEI after one cycle of HC sodiation and desodiation in various electrolytes using soft and hard XPS. They observed the best electrochemical performance for HC cycled in 1 M $NaPF_6$ in PC with FEC, and attributed this to the formation of a thinner SEI layer.[131] Carboni et al. followed the SEI evolution during initial cycling on glucose-derived HC in 1 M NaTFSI in PC with 3% FEC.[42] They found that the organic–inorganic hybrid SEI evolved in composition and thickness upon cycling, but stabilized after approximately 10 cycles. Using XPS, the authors also showed incomplete desodiation of

HC, as residual Na_xC was observed in the desodiated state. This irreversible Na trapping was postulated as an additional cause for large irreversible capacity losses in HC-based Na-ion batteries.[42]

Fondard et al. studied the SEI on HC electrodes after long-term cycling using two excitation energies for depth-profiling and observed the best electrochemical performance for systems with a $NaPF_6$ and FEC-containing electrolyte. They were then able to correlate the improved performance to a SEI rich in SEDC and NaF, while poor electrochemical performance was associated with electrodes with either low NaF or high Na_2CO_3 contents in the SEI.[43] The Passerini group studied the dependence of the SEI composition and thickness on the electrolyte using a consistent HC electrode,[132] and also on the initial HC electrode surface composition and morphology using three different HC synthesis protocols.[75] The authors reported a decrease in organic SEI species on sodiated HC depending on the electrolyte salt anion in the order: $NaPF_6$ > $NaClO_4$ > NaTFSI > NaFTFSI > NaFSI.[132] The type of HC, on the other hand, had no detectable effect on the type of species present in the SEI, but did proportionally influence the concentrations of different components relative to the concentrations of oxidized species present on the pristine HC electrodes.[75]

Model studies performed on idealized, contamination-free and binder-free HC thin films, prepared by spray deposition,[133] demonstrated that under ultrahigh vacuum (UHV) conditions at room temperature, vapor-deposited Na dissolves chemically, almost completely into clean HC (**Figure 13**).[28] This underlines the facile insertion of Na in HC and corroborates theoretical predictions. In contrast, for the same amount of Na (2-3 monolayer equivalent) deposited on clean graphite at similar conditions (HOPG, Figure 13), dissolution is inhibited, and metallic Na films are formed (F. Buchner, R. J. Behm, unpublished results). This is indicated by the Na 1s peak at 1072.0 eV in combination with the specific plasmon loss features indicated in Figure 13. Furthermore, similar studies on the interaction of a presodiated HC film with 4–5 monolayer equivalents of the ionic liquid 1-butyl-1-methylpyrrolidinium bis(trifluoromethylsulfonyl)imide (BMP-TFSI) revealed that upon vapor deposition of the ionic liquid, Na is extracted from the near-surface regions and reacts with the ionic liquid (Figure 13). The driving force for this purely chemical reactive extraction process is the energy gain upon reactive interaction between the extracted Na and the adsorbed ionic liquid. This chemical reaction can be considered as a part of the initial SEI formation in Na-ion batteries. Overall, the interaction between Na and BMP-TFSI closely resembles earlier findings for Li intercalated in HOPG.[134]

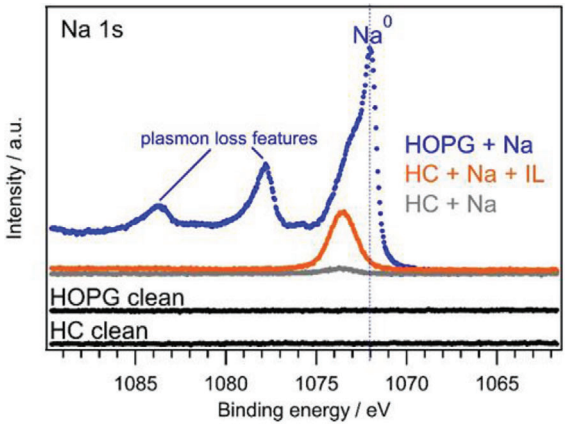

Figure 13. Na 1s spectra of clean HOPG and a hard carbon film (black dots), after vapor deposition of similar amounts of Na on HOPG (blue dots) and on the hard carbon film (gray dots) under ultrahigh vacuum conditions, and upon further deposition of 4–5 monolayer equivalents of the ionic liquid BMP-TFSI (orange dots).

Many studies compare and draw parallels between similar Na-ion and Li-ion systems,[75,132] while other works seek to elucidate the significant differences between the two monovalent battery chemistries. Photoelectron spectroscopy was used to prove,[33] understand, and help mitigate,[135] self-discharge behavior in Na-ion batteries due to SEI dissolution. Additionally, work on model $Li_4Ti_5O_{12}$ electrodes for Na^+ insertion with either Na or activated carbon counter electrodes has demonstrated that XPS is able to determine the reaction products from the Na metal counter electrode.[136]

3.6. Focused Ion Beam/Scanning Electron Microscopy (FIB/SEM) Tomography

Tomographic imaging using either X-ray computed tomography (CT), or FIB/SEM tomography of battery electrodes contributes to the understanding of the impact of 3D micro- and nanostructures on the overall performance of batteries. In addition, degradation processes within the electrode material associated with structural changes can be visualized in 3D through reconstruction of data sets.[137]

FIB/SEM is a well-established technique, initially used for TEM lamella preparation and for maskless prototyping of micro- and nanostructures.[138,139] A dual beam microscope comprises an ion beam column and an electron column which are usually mounted at an angle of 52–55° having their focal point at the specimen surface. Equipped with energy dispersive X-ray spectroscopy (EDS) and/or electron backscatter diffraction (EBSD) detectors, element mappings and information on crystalline structures are obtained. To date, commercial instruments are predominantly equipped with a liquid metal ion source (LMIS) using gallium due to its low melting point of 29.8 °C, low volatility, low vapor pressure, long lifetime, and good stability.[140] E.g., at 30 keV, gallium ion beams with 5 to 10 nm focal spots and picoampere currents can be achieved. Given the inherent high kinetic energy of the focused Ga^+ ion beam, elastic and inelastic collisions result in a cascade of interactions, such as local ablation/sputtering processes, dislocations and vacancy formation, backscattered ions, ion implantation and generation of secondary electrons.[141] The sputtering process allows cross-sectioning and site-specific preparation of samples for subsequent SEM imaging (**Figure 14**). By utilizing a sequence of sputtering and imaging steps, quantitative 3D reconstructions can be obtained. Although, FIB/SEM tomography can achieve smaller voxel sizes and hence higher resolution compared to X-ray CT, FIB/SEM tomography is a destructive method and Ga^+ ion implantation is an inherent problem leading to contamination and undesired doping of the investigated material. Within the last decade, FIB systems using liquid metal alloy ion sources and more recently with plasma sources (Xe, Ar, N, O) have been introduced, which

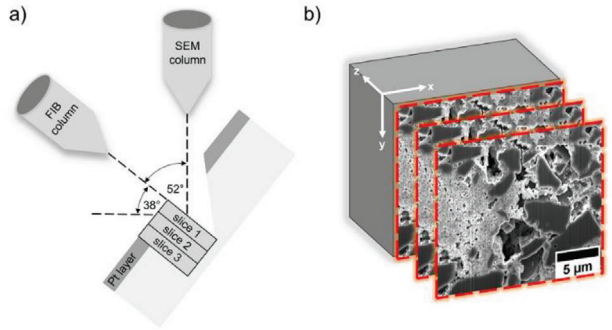

Figure 14. a) Schematic of focused ion beam/scanning electron microscopy tomography. b) Serial of stacked SEM slices of a hard carbon composite anode illustrating the consecutive slicing process for 3D reconstruction.

allow for large-scale FIB/SEM tomography, by enhanced removal rates. Microscopes using gas field ion sources, e.g., He ions, provide larger depth of field and smaller beam diameters due to their shorter wavelength compared to electrons. Therefore, its superior resolution is mainly used for imaging, since its sputtering rate is significantly lower compared to the Ga^+ ions.[141] In comparison to Ga^+ ion milling, novel plasma focused ion beams (PFIB) enable sectioning of larger volumes with edge lengths >100 µm.[142,143] Implantation effects are reduced, as Xe is not enriched and detected at grain or phase boundaries, compared to Ga ions, which can i.e. accumulate along grain boundaries in aluminium.[144]

X-ray CT[145] usually provides information on features at the micrometer scale, such as large pore channels. Transmission electron (TEM) tomography[146] excels in the sub-10 nm resolution regime, enabling detailed imaging of nanosized specimens, but is limited in the overall size that can be investigated.[147] FIB/SEM tomography can bridge the nanoscale to microscale domain with spatial resolutions ranging from a few to hundreds of nanometers. As depicted in Figure 14, volumes with edge lengths up to tens of micrometers[148] can be sliced with a slice width as small as several nanometers while recording a SEM image of the exposed cross-sections with resolution down to 1 nm.[149]

Tomography is an essential characterization tool for battery electrodes that plays a crucial role in identifying microstructural features, analyzing coating quality, evaluating the homogeneity of material distribution, but also enabling the visualization and identification of surface defects, grain boundaries, and changes in interfacial structures. This information is pivotal for understanding the electrode's structural stability, degradation mechanisms, effect of tortuosity and their impact on overall battery performance. In combination with EDS, the elemental distribution is obtained, providing information on segregation, diffusion and transformation of active species during electrochemical processes.[150] FIB/SEM instruments equipped with EBSD give insights on grain orientations and grain architectures.[151]

Sample preparation is a key step in FIB/SEM tomography, particularly if porous composite materials are studied. Porosity may lead to undesirable artifacts such as shine-through effects[152] due to pores, which are transparent for the electron beam. Filling the pore space of the electrode sample with materials like silicone resin minimizes redeposition and shine-through artifacts and enhances the grayscale contrast between individual electrode components. In addition, poor contrast between binder, conductive carbon and active electrode material and beam damage can be minimized by embedding the composite material.[153] This enhanced contrast is crucial for accurately setting threshold values when reconstructing the data sets.[154] Staining procedures of organic components like active material[155] or binders[156] with osmium tetroxide (OsO_4) further enhance the contrast.

3D reconstruction of FIB/SEM tomography data requires aligning and segmentation of the recorded 2D images. Alignment of the images is achieved by correlating shared features or fiducial markers, correcting for distortions, rotations, and translations. A challenge in 3D reconstructions is the determination of the threshold value for the segmentation of the images required to achieve accurate datasets. Recently, there has been a growing interest in the application of segmentation algorithms in combination with machine learning in order to increase the reliability of the segmented data sets, for instance, the pore volumes of highly porous systems, which is frequently underestimated.[152,157–159] This enables an enhanced semantic segmentation and subsequent classification of multiple phases within the FIB/SEM dataset, improving the overall quality of the results.

FIB/SEM tomography provides access to information about the microstructural properties of anode and cathode materials. It is frequently used to visualize mechanical degradation phenomena, such as cracking, voiding, disconnecting, and fragmentation. Such investigations have primarily focused on cathode materials for LIBs, e.g., for layered oxides,[160,161] iron phosphate,[162] and graphite anodes.[163,164]

The importance of volume fractions and distribution of the carbon binder domains (CBD) within cathode composite electrodes has been emphasized and studied by FIB/SEM tomography in order to correctly evaluate the electrolyte transport into the electrode structure. It has been shown that a heterogeneous tortuosity may lead to inhomogeneous charge/discharge states and degradation of the active material.[165] Further, the CBD influences the overall pore phase,[166] agglomeration of particles, and active surface area,[167] as well as blocks local surface reactions and impedes lithium redistribution.[168] The obtained datasets are used as input for different approaches of computational modeling of electrode structures and their corresponding transport processes. For instance, effective electronic and ionic conductivities of nickel manganese cobalt oxides (NMC)-based electrodes can be estimated,[169] by generating virtual models of real cathode structures, which overcome simplifications and lead to more realistic simulations.[170]

FIB/SEM tomography has also been employed to characterize Si anodes,[171–174] metal–air batteries,[175–177] solid-state batteries,[178–180] and SEI layers.[168,171,172,181] Significant changes of pore space, volume expansion, and interconnectivity of the active material of a Si-based anode during the cycling process were visualized by FIB/SEM tomography, and revealed the almost complete saturation of the electrode's pore network by the SEI products.[171] It has been observed that the formation of the SEI effectively hinders the fragmentation of silicon anodes.[172] The visualization of structural changes and degradation of organic porphyrin-based Li-ion battery electrodes could be shown by FIB/SEM 3D reconstruction, and wavelength-dispersive X-ray

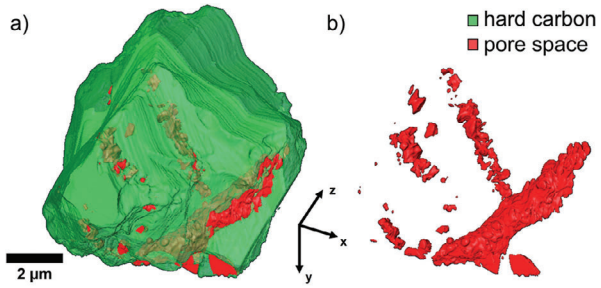

Figure 15. a) 3D reconstruction of a single hard carbon particle (green) and its pore space (red). b) Visualization of the pore space within the hard carbon particle.

spectroscopy (WDX).[155] The analysis of complex microstructures in NASICON-structured $Na_3V_2(PO_4)_3$ (NVP), a potential cathode material for sodium-ion batteries, revealed the presence of continuous nano channels inside the NVP microspheres.[182] Similar investigations on post-Li materials have been the subject of only very few FIB/SEM studies.

Porous organic, carbon-based electrodes are the preferred materials for supercapacitors and batteries due to their high energy-to-weight ratio, surface area, conductivity, and micro/nanoporous structure.[183] FIB/SEM tomography and quantitative 3D reconstruction has been used to investigate mesoporous and porous carbon-based electrodes.[184] Hard carbon, which is the preferred anode material for SIBs, has not yet been characterized via FIB/SEM tomography. Only very recently, Tratnik et al. attempted to visualize SEI formation on hard carbon via FIB/SEM cross-sectioning, where a dense surface SEI was found.[185] We have employed FIB/SEM to generate the first 3D reconstruction of an individual hard carbon particle and its pore space, shown in **Figure 15**.

3.7. Scanning Probe Microscopy (SPM)

Scanning probe microscopy (SPM) techniques, pioneered in the 1980s,[186] have significantly contributed to the visualization and understanding of nano- and microscale phenomena, and have recently gained interest for the study of interfacial phenomena at rechargeable battery electrodes. Many different techniques are included under the SPM "umbrella," such as scanning tunneling microscopy (STM), electrochemical (ec-STM), atomic force microscopy (AFM) and AFM-derived techniques like ec-AFM and Kelvin probe force microscopy (KPFM), scanning electrochemical microscopy (SECM), scanning ion conductance microscopy (SICM), scanning electrochemical cell microscopy (SECCM) and hybrid SPM techniques (e.g., AFM-SECM, SICM-SECM) The common characteristic of these methods is that local physical or (electro)chemical interactions between the probe, e.g., AFM tip, and micro- or nano-sized electrode or nanopipette are recorded (see **Figure 16**). SPM techniques give access to nanoscale and microscale information on, e.g., surface properties and processes, based on the local physical or (electro)chemical interactions with the probe across as it scans the sample surface. SPM instruments can gain high-resolution information on interfaces and formed interphases in solution, allowing in situ and operando studies at the electrode/electrolyte interface during charging and discharging.

SPM techniques are not as well-established in battery research as other characterization methods, but have recently risen in popularity because they are able to simultaneously obtain several characteristics of the cell, including: surface morphology, ionic fluxes,[187] electrochemical properties, electrical conductivity,[188] and nanomechanical properties.[189,190] Some SPM techniques, like STM, are only used on model systems, and scarcely for in situ studies with real electrode materials.[191] To date, SPM studies in battery research are primarily focused on Li-ion batteries.[190,192–194] A significant advantage of SPM compared to well-established electrochemical techniques is the insight into heterogeneity regarding nanomechanical, electrochemical, and electrical properties, which may originate from formed interphases. The rate performance of rechargeable batteries is predominantly constrained by the electrical conductivity of the anode and cathode materials and the ionic conductivity of the interfacial layers; this highlights the importance of correlating electrochemical data with material properties, such as conductance and Young's modulus, in order to elucidate local inhomogeneities. Whereas AFM-related techniques primarily provide physical information, scanning electrochemical probe microscopy (SEPM) techniques like SECM can provide information about charge transfer kinetics,[195] double-layer capacitance,[196] ion transport, diffusion, and local degradation,[197] all of which are essential for battery performance. The crucial role of the SEI in facilitating the transport of ions while passivating electrons can be studied with SEPM techniques. Among the SPM techniques, AFM, ec-AFM,[198] electrochemical strain microscopy (ESM),[199] quantitative nanomechanical AFM (QNM-AFM), and AFM force spectroscopy[200–202] are the most commonly used techniques for the study of phenomena at battery interfaces and interphases. AFM techniques are sensitive to the roughness of the material surface, which may lead to erroneous data due to AFM tip-related artefacts.[203] In contrast with static force microscopy, AFM imaging studies require careful sample preparation for electrode surfaces with high roughness, as demonstrated by Luchkin et al.[198] and Daboss et al.[204] In addition, non-contact imaging modes for in situ studies also minimize such artefacts[205] Embedding and subsequent cross-sectioning of e.g., composite carbonaceous negative electrode materials via mechanical polishing significantly reduces S_z values (maximum height of a defined area) from several microns to submicron.[204] This reduction minimizes artifacts and enables the direct observation of SEI formation. Spatially resolved electrochemical measurements obtained via SECM or SECCM, which so far have been done mainly on active particles, e.g., $LiMn_2O_4$,[206] are less prone to artifacts, particularly in SECM, when microsized electrodes are used, even in constant height[207] or constant distance modes.[208]

A significant body of literature has been published on interfacial processes at anodes and cathodes of LIBs, including SPM and SEPM studies on interphase formation.[209–213] SEPM techniques, like SECM and pipette-derived techniques like SECCM, have the advantage that they are noncontact techniques. These techniques are primarily used to study processes at Li-ion batteries,[214,215] including: SEI formation on the negative electrode,[210,216] the influence of applied potential and solvent

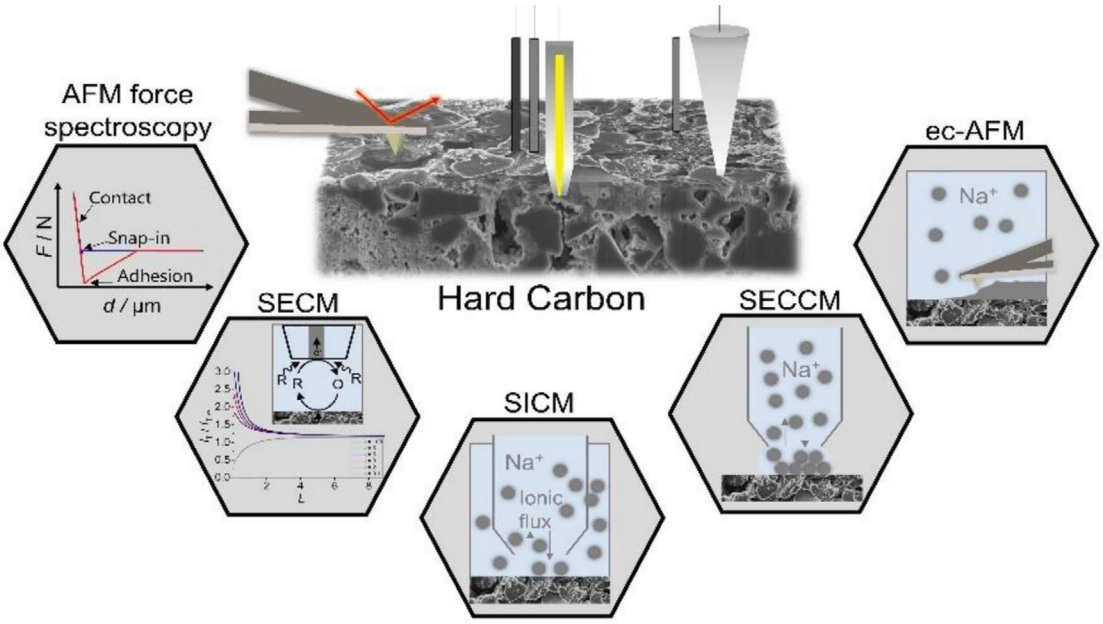

Figure 16. Overview of selected S(E)PM techniques being utilized in battery research.

decomposition on electron transfer processes at the electrode,[217] and visualization of deintercalation processes.[218] These techniques are also able to observe dynamic changes in relation to the formation of interphases (e.g., by electrolyte degradation), electrochemical properties of the interface during cycling, fluxes towards electrodes, and the influence of such processes on battery performance. The application of SECM holds promise in addressing scientific challenges at bulk processes,[219] for example, by relating spatially resolved visualization of the activity of the electrode and interface to bulk properties, and surface processes[209] at anodes and cathodes.[220,221]

With SECCM local charging/discharging experiments can be performed at single particles in situ without the influence of neighboring particles which is highly interesting for composite electrode materials. Even if expensive ionic liquids and electrolytes or expensive samples are used, only a tiny surface area (e.g., 1 μm^2) is exposed to the electrolyte thus saving on materials and resources. SPM is nondestructive and all techniques can operate in solution avoiding potentially altering cleaning and drying steps before characterizing the materials. The achieved resolution depends on the used probe and for AFM based techniques lies in the (sub-) nm range, and in the µm range for microelectrodes (e.g., SECM), respectively. Samples need to be flat (S_z < 6 µm) which is hardly ever the case for battery composite materials and needs additional preparation, e.g., by embedding the sample and polishing the surface. Force spectroscopic measurements may provide quantitative nanomechanical information, e.g., Young's modulus of battery components.

The effectiveness of the SEI in blocking electrons and preventing electrolyte decomposition while remaining stable during (de)intercalation, is closely associated with local electron transfer kinetics. SECM has been used to visualize the heterogeneities of the local electrochemical activity on the electrode surface that arise during in situ SEI formation.[209,210,216] SECM probes employing alternating current (AC) mode can use potentiometric electrodes, which allow for the mapping of ionic fluxes of Li^+ or Na^+ and determination of the dielectric permittivity and ionic resistivity of the SEI.[222,223]

A challenge, but an important aspect for composite electrodes and heterogeneous samples, is the correlation of electrochemical to morphological and nanomechanical properties, which provides local structure-activity information. Recently, hybrid SPM techniques[224–226] like AFM-SECM[227] have been used in battery research to get insight into interfacial processes, such as spatially resolved electrochemical information, nanomechanical properties (e.g., adhesion properties, Young's modulus), aging processes, and interphase formation.

So far, only a limited number of SPM studies have appeared on post-Li battery electrodes.[200–202,204,228–232] SIBs are considered to be the most promising and technologically most developed next generation battery chemistry.[233,234] However, different results have been published in respect to the effect of additives or the used cathode material[43,71,131,235,236] and redissolution of SEI.[237] SEPM techniques have been employed to study the SEI formation in embedded cross-sections of negative electrodes, such as highly oriented pyrolytic graphite (HOPG),[198] mesocarbon microbeads, graphite, graphene[231] and HC.[198,204] **Figure 17** shows SECM studies on spray-coated HC composite anodes (Kuranode hard carbon, Kuraray, Japan) for SIBs. The pristine electrode reveals uniform conductivity, which is reflected by the positive feedback response, as evidenced by approach curves recorded at multiple positions using ferrocene (Fc) as redox active species added to solution (Figure 17a). After 40 galvanostatic charge–discharge cycles versus Na^+/Na (0.1 C, 1 M $NaClO_4$ in PC), the SECM image (Figure 17b) reveals consistent negative feedback across the entire surface, which is corroborated by the approach curves obtained at marked positions. This indicates that a uniform, blocking interphase was formed. The dimensionless heterogeneous substrate kinetics parameter κ can be derived from the current expression displayed in Equation 3, where the

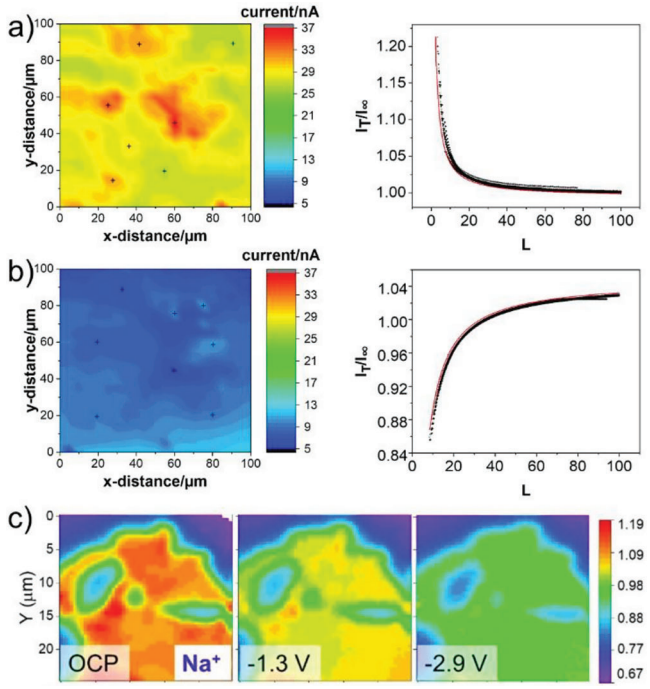

Figure 17. SECM feedback images of pristine (a, left) and cycled (b, right) hard carbon composite anodes (40 cycles in 1 M $NaClO_4$ in PC). The marked points in the images indicate locations where the approach curves (right) were recorded (black: experimental and red: corresponding theoretical fit). c) SECM feedback images of a multilayer graphene electrode in 0.1 M $NaBF_4$ at OCP (left), 1.3 V (middle) and 2.9 V (right) versus ferrocene (Fc/Fc^+). The scale shows the ratio between the tip current to the current obtained in bulk ($I_T/I_{T,\infty}$). Adapted with permission.[231]

current is expressed as a function of RG (ratio between the insulator thickness r_{glass} and the radius of the microelectrode r_T), L (ratio of distance to r_T) and κ.[238]

$$I_T(L, RG, \kappa) \approx I_T^C\left(L + \frac{1}{\kappa}, RG\right) + \frac{I_T^{Ins}(L, RG) - 1}{\left(1 + 2.47\ RG^{0.31}\ L\ \kappa\right)(1 + a)} \quad (3)$$

with

$$a = L^{0.006\ RG + 0.113}\kappa^{-0.0236\ RG + 0.91} \quad (4)$$

Approach curves were recorded using an ultramicroelectrode (r = 1.5 µm, RG = 40). Positive feedback was obtained for the pristine HC with $\kappa = 1.32 \pm 0.18$ ($n = 8$) and negative feedback at cycled HC (40 cycles) with $\kappa = 0.24 \pm 0.09$ ($n = 8$), indicating the insulating nature of the formed SEI. The effective heterogeneous substrate kinetics constant κ_{eff} ($\kappa_{eff} = \kappa \cdot D \cdot r^{-1}$) was extracted using $D = 2.24 \times 10^{-5}$ $cm^2\ s^{-1}$[239] and $r = 1.5$ µm. κ_{eff} decreased from 0.1978 ± 0.0262 cm s^{-1} for pristine composite electrode to 0.0360 ± 0.0139 cm s^{-1} in the case of the cycled electrode. Zeng et al. conducted a study on the initial formation of the SEI on multilayer graphene electrodes in $NaBF_4$ in EC:PC, quantifying the passivation and cation uptake using SECM.[231] A nonconductive growing interphase was found due to passivation of the electrode (Figure 17c).

As shown in Figure 17, SEI formation and the ability of the formed SEI, e.g., on HC electrodes, to block electron transfer can be studied via SEPM.

3.8. X-Ray Diffraction (XRD)

In the context of SIBs XRD (and also neutron diffraction) is predominantly utilized for structural characterization of the hard carbon material, i.e., on the anode side of the cells. Here, XRD allows for determining relevant structural parameters of different carbon materials, for instance to relate the performance in the SIB with specific structural motifs of HC. Note that from a formal point of view it is more appropriate to use the term "Wide-angle X-ray Scattering" compared to "XRD," as these HC materials feature a marked degree of structural disorder, which results in quite diffuse scattering maxima.[240] This point is not only a matter of terminology, as the substantial disorder of the graphene stacks pertains to the interpretation of the experimental data (see below). Nevertheless, to avoid confusion, here we continue with "XRD." Commonly, the average interlayer spacing $\bar{a}_3$ itself is regarded as the most relevant parameter, which can be extracted from the prominent 002 reflection of HC. Ideally, $\bar{a}_3$ can be determined from the position of the 002 reflection $2\theta_{002}$, applying Bragg's law: $\bar{a}_3 = 2/\lambda \sin(\theta_{002})$, with λ being the wavelength used.

For instance, Bommier et al. applied ex situ XRD experiments proving the reversible expansion and contraction of the graphene layers nanosheets of sucrose-derived HC.[55] As main insight, an intercalation mechanism was identified in the low-potential plateau region.

As important advanced methodology, in situ or operando XRD experiments can be used to peer into the sodium filling mechanism by monitoring fine structural changes in the atomic structure of HC. Again, mainly the parameter $\bar{a}_3$ is usually studied, providing insight into the widening/decline of $\bar{a}_3$ upon sodiate/desodiation of Na^+ into/out of the interlayer space between the graphene layers. Yet, aside from its position changes in the intensity and width of the 002 reflection can also shed light into the filling mechanism: by such experiments it was recently observed for hard-carbon nanofibers (HCNF) that within the initial sodiation in the slope region, the 002 reflection undergoes narrowing and a decline in intensity, implying that Na^+ ions are inserted between the graphene layers and that NaC_x might be formed (**Figure 18**).[241] Furthermore, treating the HCNF at different temperatures modified $\bar{a}_3$ which thus allowed for comparison with theoretical predictions for an optimum $\bar{a}_3$ value.

However, as recently pointed out by Chu et al.,[242] the characterization of the atomic graphene stack structure of HC should go beyond the average interlayer distance $\bar{a}_3$ and include further relevant structural parameters such as the graphene layer extension L_a and the stack height L_c (as well as their distribution), and defects in the graphene stacks. The latter comprise point defects within the graphenes themselves and "external" defects at the graphenes' edge. These parameters can be evaluated from XRD and neutron diffraction data by advanced evaluation methodology, based on two main approaches, namely either fitting the entire XRD curve (i.e. in reciprocal space) by appropriate theoretical functions[243,244] or by calculating the pair-distribution function (PDF).[55] Combining XRD and Raman spectroscopy

data suggested that the capacity in the sloping region might not only be related to $\bar{a}_3$, but even dominated by defects in the HC structure.[55] Based on XRD as well as small-angle X-ray scattering, Morikawa et al. found that filling of HC nanopores is a further relevant storage mechanism.[245] Among other points, such finding was concluded from the observation that upon deep sodiation in the plateau region the 002 signal does not change, indicating a pore filling mechanism.

The importance of advanced XRD analysis was recently discussed by Glatthaar et al., showing that a precise determination of the average interlayer spacing $\bar{a}_3$ from the commonly quite broad 002 reflection (or higher order 00*l* signals) needs a careful consideration of different effects: among others, an asymmetric background (e.g. from the small-angle scattering of nanopores) and the translational disorder in the stacking may affect the position of the maximum of the 002 signal.[246] It was demonstrated that applying the Bragg equation on the XRD raw data can result in too large $\bar{a}_3$ values, especially for HC with pronounced disorder. While the observed discrepancy of up to ca. 0.2 Å for samples treated up to moderate temperatures up to 1300 °C might appear minor, theoretical approaches discuss fine differences $\bar{a}_3$ affecting the energy for sodium insertion and thus changing the storage mechanisms in SIB.[246] Hence, given the typical range of $\bar{a}_3$ values (ca. 0.34 to 0.4 nm), such potential uncertainty is relevant and requires further detailed state-of-the-art XRD and neutron diffraction analysis.

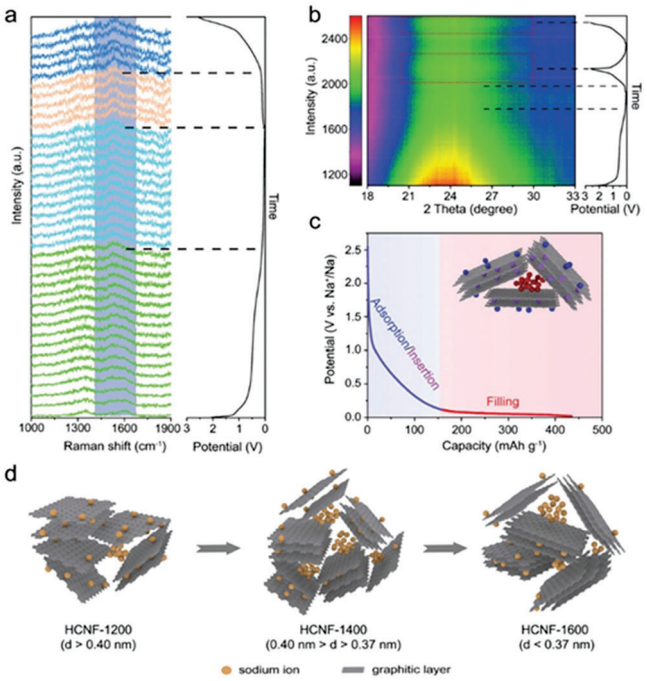

Figure 18. In situ characterization of sodium insertion in hard-carbon nano fibers (HCNF[241]), as a function of carbonization temperature (here 1200 °C–1600 °C). a) In situ Raman spectra and b) in situ XRD patterns of HCNF-1400. c) Schematic illustration for the adsorption/insertion–filling sodium storage mechanism in the HCNFs. d) Schematic illustration for the sodium storage mechanism of HCNF-1200, HCNF-1400, and HCNF-1600, as a function of the interlayer distance. Adapted with permission.[241]

3.9. Scanning Transmission Electron Microscopy (STEM)

Scanning transmission electron microscopy (STEM) has played a crucial role in enhancing our understanding of the influence of structure and defects on the performance of batteries and battery materials and the structural changes involved during charge and discharge cycles. Using STEM, it is possible to track and analyze these changes down to the atomic scale, such as the phase transitions observed at the surface of various oxides[247,248] or the growth of Na/Li dendrites in solid electrolytes.[249,250] Studying these structural transformations can help to elucidate the degradation mechanisms and to shed light on the electrochemical processes in battery materials.

The principle of STEM is similar to SEM, but with the key distinction that the forward scattered or transmitted electrons are used for imaging. This requires higher kinetic energy for the electrons (typically 60–300 keV), resulting in a shorter electron wavelength, smaller interaction volume and thus higher resolution capabilities. Additionally, the specimen under examination must be electron transparent, typically with a thickness below 100 nm.[251]

When the incoming electron wave interacts with the atomic structure, it can either pass through the specimen without interaction or undergo elastic and inelastic scattering. The elastically scattered electrons are classified based on their scattering angle. High-angle scattered electrons (>3°), as a result of the coulomb interaction between the incoming electrons and the atomic nucleus, are incoherent and their intensity is influenced by the atomic number (*Z*) of the elements present within the specimen. These waves can be detected using an annular-shaped detector with contrast is proportional to $Z^{1.5-2}$, forming a high-angle annular dark-field (HAADF) image.[252]

On the other hand, low-angle scattered electrons (<3°) are mostly coherent and can interfere with each other, producing a diffraction pattern. The electron diffraction pattern is generated based on Bragg's law, which relates the scattering angle to the crystal lattice spacing for constructive interference. As shown in, when scanning a nanometer-sized probe over the specimen, a series of diffraction patterns is generated at each probe position. These diffraction patterns form a 4D (4D-STEM) dataset, with two dimensions corresponding to the spatial axes and two dimensions representing the spatial frequency components of the diffraction pattern. The information that can be acquired through 4D-STEM includes:

1. Crystallographic orientation mapping: The diffraction patterns of the 4D-STEM data set can be analyzed to determine and map the crystallographic orientation distribution in the specimen, providing insights into grain boundaries, phases present and texture variations[253] as well as mapping the lithiation state if it is associated with sufficient crystallographic change.[254]
2. Strain and deformation mapping: The analysis of the diffraction patterns in 4D-STEM allows for the characterization of strain and deformation fields within the sample. By comparing the diffraction patterns with a reference pattern, changes in lattice spacing and crystal distortions can be quantified, providing insights into the mechanical properties and stress distribution of the material.[250]

3. Charge distribution analysis: By utilizing differential phase contrast (DPC) techniques in conjunction with 4D-STEM, information about the charge distribution and charge field can be extracted. In 4D-STEM DPC, the deflection of the central diffraction disc is measured. This deflection is caused by the interaction of the primary electron beam with the electric field within the specimen. By analyzing the extent and direction of the deflection, it is in principle possible to gain insights into the electric field and charge density of the material.[255]

By combining 4D-STEM with DPC and other spectroscopic techniques, such as electron energy-loss spectroscopy (EELS) and EDS it becomes possible to obtain compositional information and insights into the electronic structure, including bond type, oxidation state, and bandgap alongside the crystal orientation.[256,257]

Recently, Hughes et al.[258] employed 4D-STEM and EELS to investigate the strain and chemical evolution at the solid electrolyte-electrode interface. This study focuses on understanding the structural changes and chemical composition variations occurring at the interface during battery cycling. This combination provides a comprehensive understanding of the SEI and its impact on battery performance. The reliable preparation of STEM samples is crucial for meaningful investigations, especially when dealing with materials sensitive to electron beam irradiation. The most commonly used method for targeted preparation is focused ion beam (FIB), but the structural modifications caused by FIB are not well understood for various materials. Ziming et al.[259] studied the impact of both the electron and Ga^+ ion beam on insulating solid-state electrolytes, including lithium phosphorus oxynitride, Na-β''-alumina solid electrolyte (BASE), and $Na_{3.4}Si_{2.4}Zr_2P_{0.6}O_{12}$ (NaSICON). The researchers observed significant growth of lithium/sodium whiskers induced by both beams, even at low doses, resulting in a notable change in the chemical composition. This whisker growth is likely due to surface charging, which can be mitigated by coating the sample with a layer of gold or preparing it under cryogenic conditions (**Figure 19**).

STEM and 4D-STEM can be employed in situ to investigate Na-ion transport in a solid electrolyte to understand the role of the microstructure on sodium diffusion and dendrite formation. **Figure 20** demonstrates the utilization of STEM imaging along with 4D-STEM orientation mapping for visualizing the microstructure of a Na-β''-Al_2O_3 electrolyte and the distribution of Na^+ during biasing. After the 1st cycle, Na^+ diffused to the Au/electrode interface as well as along the grain boundary. This has been verified by STEM-EDS. Furthermore, the results reveal that the Na-ion transport to the Na-β''-Al_2O_3/Au electrode interface depends strongly on the local crystal orientation and sodium dendrite formation occurs at specific grain boundaries (indicated by green arrows).[259]

Here, 4D-STEM is providing the crystallographic orientation information of the grains and thus characterizes the grain boundaries. This information helps to optimize the microstructure to enhance sodium-ion mobility and reduce dendrite formation.

In the literature there are currently only limited publications with TEM dedicated to a detailed structural characterization of HC electrodes.[229] The disordered structure with

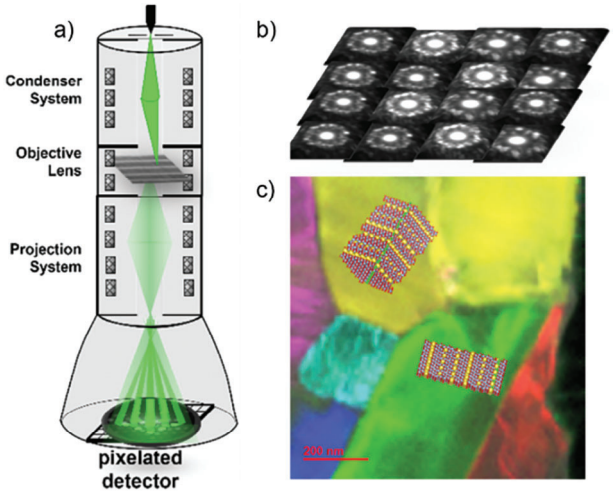

Figure 19. 4D-STEM on a Na-β''-alumina solid electrolyte: a) Principle of 4D-STEM, b) array of diffraction patterns and c) inverse pole figure highlighting the crystal orientation distribution map.

(sub)nanoscale pores renders classical (S)TEM characterization techniques difficult. However, some recent advanced techniques such as STEM-PDF[260] or high-resolution STEM-EELS[261] might provide new insights into the structural changes to elucidate structural changes during electrochemical processes in SIBs.

3.10. Electrochemical Single Electrode Microcalorimetry

Electrochemical methods like cyclic voltammetry or electrochemical impedance spectroscopy are based on the measurement of the electrode potential as a function of current or charge. From a thermodynamic point of view, since the (equilibrium) cell

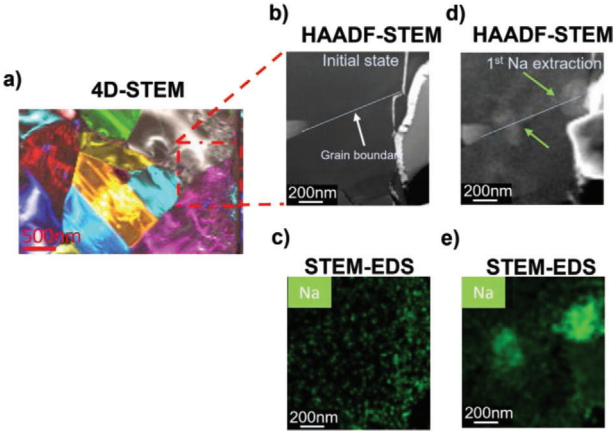

Figure 20. Formation of Na-filament along the grain boundary: a) 4D-STEM orientation map highlighting the nanocrystalline nature of the Na-β''-alumina. b) HAADF-STEM image of the region marked by the red dashed rectangle in a) and c) is the corresponding Na elemental map showing no enrichment of Na at the interfaces or grain boundaries (marks as white line in b). d) HAADF-STEM image after the first cycling shows the appearance of brighter contrast along the grain boundary. The corresponding STEM-EDS map in **e)** shows a clear enrichment of Na at the GB.

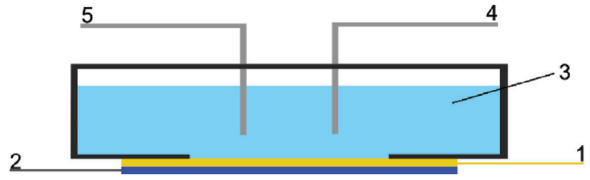

Figure 21. Sketch of a microcalorimeter for which a detailed version can be found in ref. [266] The temperature of a thin working electrode (1) is measured at its backside by a thin pyroelectric sensor (2). On top of the working electrode the electrochemical cell (3) with counter and reference electrodes (4, 5) is mounted.

voltage is related to the free enthalpy of the cell reaction, $\Delta_R G$, the measurement of the potential corresponds to the determination of $\Delta_R G$, as a function of the current or charge, including some deterioration by overpotential. However, there are other thermodynamic quantities of similar significance that are worth considering. Here, we will discuss the measurement of the heat, which is evolved at a single electrode, that is, e.g., in one half-cell of a battery system, as a function of current or potential and time. In general, the heat q evolved upon an electrode reaction can be separated[262–264] into two parts, $q = q_{rev} + q_{irrev}$. The reversibly exchanged heat, q_{rev}, changes its sign upon reversal of the current flow. It corresponds to the heat, which is evolved or absorbed during an infinitely slow process at the electrode–electrolyte junction close to thermodynamic equilibrium. It is also called Peltier heat. In real electrochemical systems, the reactions proceed within finite time, driven by overpotential, which will lead to the production of additional, irreversible heat, q_{irrev}, due to deviation from thermodynamic equilibrium. The reversibly exchanged (Peltier) heat at a single electrode is directly related to the entropy change of the electrochemical reaction, $\Delta_R S$. However, since ions and electrons are transported across the border of the half-cell during the reaction, their heat of transport[262] has to be considered, which leads to a "correction" of the usual formula for the reaction entropy by the entropy of transfer, $\Delta_T S$. The reaction entropy is then given by: $\Delta_R S = q_{rev}/T + \Delta_T S$, where T is the temperature of the isothermal system.[262–264] In aqueous systems $\Delta_T S$ can often be explicitly calculated from literature values of the heat of transport. For nonaqueous systems the transport "correction" might be more difficult to determine, however, approximations exist.[262] In addition, in many systems $\Delta_T S$ is small compared to the reaction entropy of the electrochemical electrode reaction.[262,263]

Most methods for the measurement of heat evolution or absorption at a single electrode rely on the measurement of temperature changes either of the electrode itself or the complete half-cell upon the electrochemical reaction. Traditional approaches are summarized, e.g., in references.[262,263,265] For an experimental setup reaching sub-monolayer sensitivity see, e.g., **Figure 21** and ref. [266].

An early application of single electrode microcalorimetry for the measurement of Peltier heats in battery systems dealt with zinc and bromine electrodes in zinc–bromine and zinc–air batteries.[267] Rather large conversions of up to 1 C were necessary, due to a relatively bulky electrode-thermistor setup. Recently, single electrode microcalorimetry was demonstrated for Li and Na bulk deposition in order to determine the reaction entropy in carbonate and diglyme based electrolytes.[268,269] In both cases, conversions below a few percent of a metal monolayer were employed. It should be noted that calorimetry is also effective at studying these properties in full cells, where the complete cell is immersed in the calorimeter. Using this method, e.g., Dahn et al. studied the reaction entropy of Li intercalation into $Li_xMo_6Se_8$ versus a Li electrode.[270] For more recent applications see, e.g., ref. [271]. In addition, the Peltier heat and reaction entropy of single electrodes is also attainable using thermocells, cells where the electrodes are kept at different temperatures (see, e.g., refs. [272,273] and references therein). Another popular approach for the study of the reaction entropy of battery systems, known as entropy profiling, involves measuring the temperature coefficient of the equilibrium cell potential.[274–276]

An example of single-electrode microcalorimetry is shown in **Figure 22**, which displays current, potential, electrode temperature and heat transients for Na deposition (left) and Na dissolution (right) on a thick Na film in 1 M $NaClO_4$/PC by 10 ms long current pulses with amplitudes of −0.3 and +0.3 mA, respectively (see first row of Figure 22). The potential (second row) essentially follows the current pulses, indicating negligible mass transport limitations. For Na deposition (left) the electrode temperature decreased linearly during the current pulse, signaling cooling of the electrode with a constant heat flux. After the pulse, the temperature relaxed towards the original temperature by thermal equilibration with the environment. The bottom row gives the total heat, which was determined from the temperature transients, and which was liberated or absorbed up to time t by the electrochemical reactions. Upon reversal of the current pulse polarity (right panel) all transients are almost quantitatively reversed, signaling the high reversibility of the Na deposition reaction under the studied reaction conditions. For further details and a discussion of the implications of the reaction entropy obtained from these measurements see ref. [269]. The time dependence of the total exchanged heat can also be obtained with single electrode microcalorimetry. This provides insights into the transport

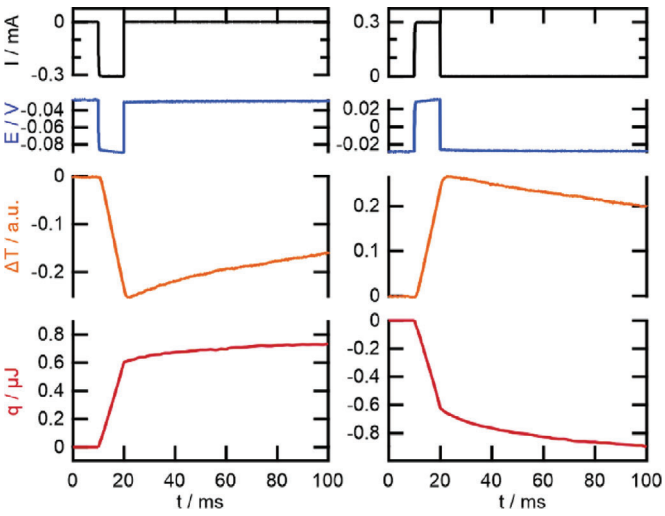

Figure 22. Current, potential, temperature and heat transients for Na deposition and dissolution by 10 ms long current pulses of −0.3 mA and +0.3 mA in 1 M $NaClO_4$/propylene carbonate. Upon reversal of the polarity of the current, that is, the direction of the electrochemical reaction, all transients change their signs.

mechanisms of Na^+ into and through the SEI.[277] Microcalorimetric measurements can also be conducted with HC electrodes, as long as they are thin enough to ensure fast heat transfer to the pyroelectric sensor.[133]

3.11. Solid-State Nuclear Magnetic Resonance (ssNMR)

Solid-state NMR is a versatile analytical method playing a crucial role in investigation of lithium- and sodium-ion battery[278,279] materials and systems, such as carbon,[280] $Ti_3C_2T_x$,[281] Sb,[282] SiCN,[283] Sn,[284] $Na_3V_2(PO_4)_3$ (NVP),[285] $Na_{2\pm x}V_3P_2O_{13}$,[286] $Na_3V_2O_{2x}(PO_4)_2F$,[287] Na_3PS_4,[288] $Na_{2+2x}Fe_{2-x}(SO_4)_3$,[289] $Na_4Fe_3(PO_4)_2(P_2O_7)$/C,[290] Na_2FePO_4F,[291] PBA,[292,293] and NASICON.[294]

The natural availability of a variety of atomic sensors across the periodic table, like nuclear spins as ^{1}H, ^{2}D, ^{6,7}Li, ^{11}B, ^{13}C, ^{14,15}N, ^{19}F, ^{23}Na, ^{25}Mg, ^{27}Al, ^{29}Si, ^{31}P, ^{33}S, ^{35}Cl, ^{39}K, ^{51}V, ^{119}Sn, etc., are of considerable value probing local structure, mobility, formation, transfer, reaction, and degradation mechanisms. It's wealth of information relies on nuclear spin interactions of atomic level perturbations in the energetic order of 10^{-7}–10^{-15} eV. Aside from the basic Zeeman contribution due to the applied external magnetic field, a couple of nuclear spin interactions are naturally present:

a) Shift contributions (chemical shift: CS, Fermi contact shift: FCS, Pseudo contact shift: PCS, Knight shift: KS, magnetic susceptibility shift: MSS and induced current shift: ICS)
b) Nuclear spin couplings (direct nuclear spin coupling: DNC, indirect nuclear spin coupling: INC)
c) Direct nuclear spin to unpaired electron spin distribution couplings (DNEC)
d) Quadrupolar interaction (QI).see **Table 1**.[278]

Table 1. NMR interaction types, their short description/origin and information content obtained from related spectral features (*MAS:[295,296] magic angle spinning to average out anisotropic interactions and **MW: microwave irradiation to decouple the electron spins from the nuclear spin,[297] both methods are useful for spectral resolution enhancement).

Type		Description	Information content
Shifts	CS	(De)shielding of the external magnetic field due to local valence electrons and through space effects	Site specific differentiation of ^{1}H, ^{6,7}Li, ^{11}B, ^{13}C, ^{19}F, ^{23}Na, ^{27}Al, ^{31}P, ^{29}Si, etc. species associated to the electrolyte, graphene-like sheets, SEI and CEI formation with related decompositions (NaF, NaCl, NaOH, NaO_x, Na_2CO_3, Na_xPO_y, etc.)
	FC	Field shift due to the acting isotropic part of unpaired electrons	Isotropic influence of radicals (within carbon, electrolyte, binder, etc.) and paramagnetic species (impurities, hetero-atoms and/or additives) depends on spin density, proximity, and temperature
	PCS	Field shift due to the anisotropic part of unpaired electrons	Anisotropic influence of radicals and paramagnetic species, see row above
	KS	Shift effect of the unpaired conduction band electrons	Metallic species to be identified (macroscopic metal contributions are mostly silent due to the Faraday effect and induced currents but may introduce magnetic susceptibility effects onto nearby material distributions)
	MSS	Overall magnetic susceptibility effect	Nearby and surrounding second order (nano- to microscale) material formations: graphene-like sheet, pore, binder, electrolyte, additive distributions, and densities
	ICS	Field shifts due to induced currents	During spinning (MAS*) of locally conductive materials within a magnetic field, local currents can be induced which produce an opposite field (shift dependence on the spinning speed)
Nucl. Dipole Couplings	DNC	Direct homonuclear and heteronuclear spin interaction (through space)	Proximity and distance information, distance encoding $\approx 1/r^3$
	INC	Indirect homonuclear and heteronuclear spin interaction (through bonds)	If spectroscopically resolvable it provides information about bond structures, hybridizations, coordination, and bond-order (e.g., coupling via 3, 4 or 5 bonds), e.g., electrolyte and (de)compositions
Quadrupole interactions (QI)		Quadrupolar moments (Q_m) interact with the surrounding electric field gradient (EFG) of the local electron distribution	For nuclei with suitable large Q_m (^{2}D, ^{6,7}Li ^{11}B, ^{14}N, ^{17}O, ^{23}Na, ^{25}Mg, ^{27}Al, ^{33}S, ^{35}Cl, ^{39}K, ^{43}Ca, ^{51}V, etc.) information about coordination, crystal order and mobility can be obtained but may often lead to broad spectral features, i.e., advanced experimental techniques are needed (MQ-NMR and ultra-fast NMR).[300]
DNEC		Direct nuclear to electron spin coupling through space	An average electron spin distribution due to radicals or transition metals will considerably broaden NMR spectral features requesting decoupling efforts (ultra-fast MAS or MW** irradiation).

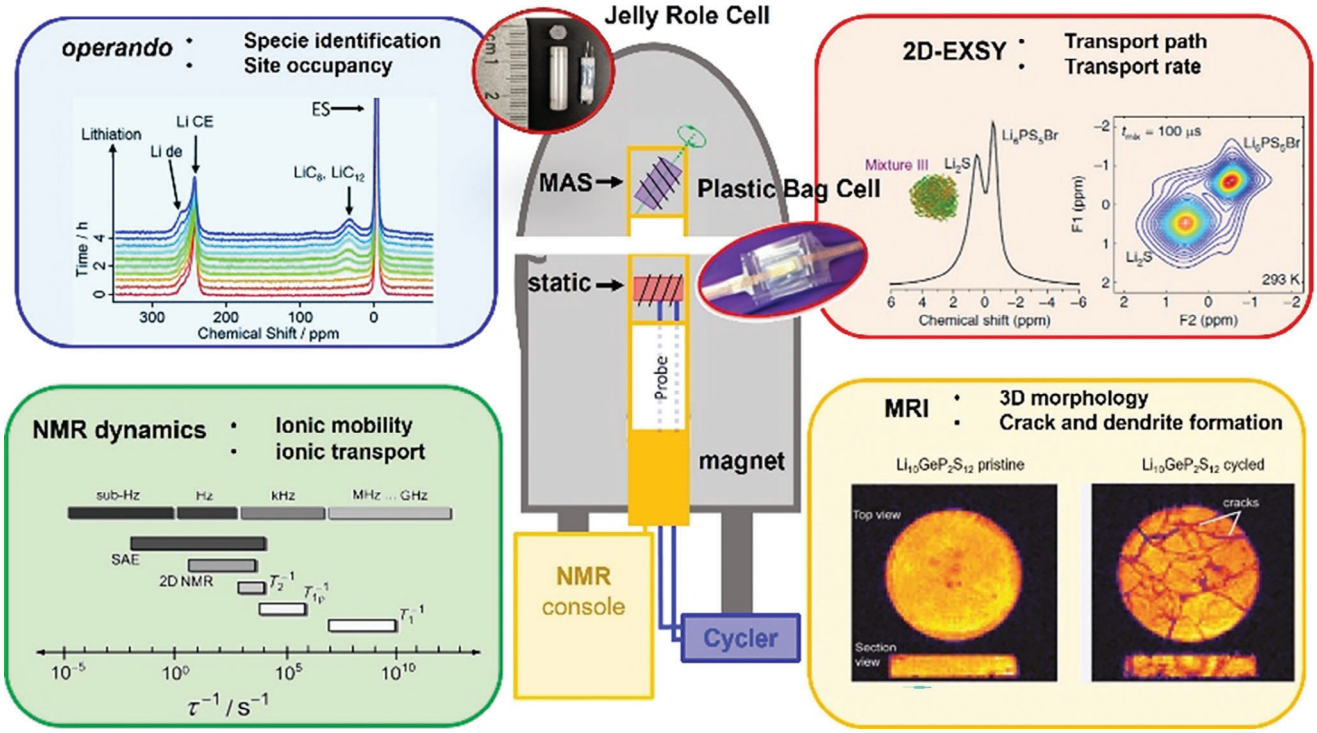

Figure 23. Schematics of current scope of the advancing ssNMR with its applications in battery characterization. Static-, MAS NMR and imaging has been used for ex situ, in situ, and operando methodologies to gain information about sites, dynamics and morphology. Reproduced with permission.[316] Copyright 2020, Royal Society of Chemistry; Reproduced with permission.[302] Copyright 2019, American Chemical Society; Reproduced with permission.[317] Copyright 2017, Springer; Reproduced with permission.[318] Copyright 2018, ACS Publications; Reproduced with permission.[319] Copyright 2012, Wiley-VCH27; Reproduced with permission.[278] Copyright 2017, ACS Publications.

Due to these internal interactions, for ^{6,7}Li- and ^{23}Na-NMR, the different components of an electrochemical cell (anode, cathode, electrolyte, binders, additives) span a large shift range from +1500 to −50 ppm, see **Figure 23**.

As sketched in Figure 23, solid-state NMR methods can be classified into two branches: static and MAS methodologies applied to ex situ, in situ and operando setups to investigate sites/species, dynamics, transport paths/rates and spatial resolved properties (MRI).[298,299]

However, several limitations have to be considered:

- NMR distinguishability is based on magnetically non-identical sites
- Nuclear spins become silent in the proximity of unpaired electron spins (e.g., Fe, Mn, Ni, Co, etc.)
- Some nuclear sensors provide a reduced sensitivity due to their low abundance, low gamma and large quadrupolar coupling (e.g., ^{17}O, ^{25}Mg, ^{33}S and ^{35}Cl).

Major advantages of ssNMR are:

- Applicable to different phases (liquid, gel, crystal, amorphous and metallic)
- Availability of a variety of nuclear sensors
- Sensitivity to couple of nuclear interactions' variations due to structural and morphological influences (bonds, coordination, grain boundaries, geometry frustrations, core/shell, surfaces, phases, mobilities, etc.)
- Probe for paramagnetic influences (shifts, line-broadening, and relaxation behavior).

^{23}Na ssNMR has been applied to identify different Na-species like:

- Solvated ions (electrolyte, e.g., $NaClO_4$ or $NaPF_6$),
- Adsorbed at defects, surfaces, and edges,
- SEI formation, originating from degenerated electrolyte (Na_2O, NaOH, NaCl, NaF, Na_2CO_3, Na_xP_y and Na_xPO_y);[278]
- Intercalated between sheets,
- Metallic fillings in pores

Two of the biggest challenges for HC in SIBs[234,279,301] are 1) storage capacity and 2) uncontrolled SEI degradation. Both can be monitored by ssNMR. Improved insight, especially improved spectral site-specific identification with structural localization, is expected to be gained by applying improved multinuclear and multidimensional experiments, ultrafast MAS[295,296], and in situ MAS NMR[303,304]. For accessing less-sensitive nuclei, a polarization enhancement (DNP) could be applied.[305,306]

NMR analytical investigations of LIBs and SIBs mostly follow similar methodologies. However, for the observation of the charge transfer nuclei (^{6}Li, ^{7}Li and ^{23}Na) exist differences, more between the rarely measured ^{6}Li versus ^{7}Li/^{23}Na than the most

common ^{7}Li vs. ^{23}Na, e.g. spin (1, 3/2, 3/2), natural abundance (7.59, 92.41, 100%), chemical shift range (28, 28, 72 ppm—electron density at sodium is larger than lithium most relevant for discriminating diamagnetic contributions), Larmor frequency (14.7, 38.9, 26.4% in respect to 1H), quadrupolar moment (-0.08, -4.01, 10.4 fm^2) and receptivity (0.001, 0.271, 0.093 in respect to 1H).

3.12. Computational Modeling

In this section, we will briefly discuss several computational analysis methods ranging from atom-scale to cell-scale simulations. Each of these modeling methods has a long history of usage in the study of different battery systems.[307] The majority of these studies have been focused on Li-ion based chemistries. However, there is a growing interest in Na-ion chemistries, and many of the methodologies used in prior Li-ion anode interface studies can be applied to Na-ion systems, too.

Density functional theory (DFT) calculations are the finest-grained method that we will discuss here, they are hallmarked by explicitly accounting for electrons in the form of density fields.[308–310] These calculations can be used to study atom-scale properties such as molecular and surface geometries, reaction energies and barriers, and solvation structures. Ab initio molecular dynamics (AIMD) is essentially an extension of DFT onto time-dependent systems.[311,312] AIMD allows for the examination of dynamical behavior, such as ion transport and intercalation, solvation behavior, surface evolution, and reactivity. These are known as "first principles" methods, which means they do not need parametrization from experiments or other computational methods. They are highly computationally expensive and are limited to simulating systems on the order of hundreds of atoms at picosecond timescales.

Several recent studies have employed DFT calculations to examine the stability of various electrolytes in Na-ion systems.[313,314] These studies were able to establish reduction mechanisms and energy barriers of common carbonate electrolytes. They established that out of EC/PC/VC, VC is the most likely species to undergo 1-electron reduction to form organic SEI components, and EC is the most likely species to undergo 2-electron reduction to form carbonate SEI components. EC was shown to have the highest reduction potential and lowest reaction barrier, which indicates that EC ring opening is the primary mechanism of SEI growth. VC and FEC were studied as additives for these systems, and were both observed to preferentially react instead of EC. They also raised the reaction barrier of neighboring EC, leading to reduced reactivity and different decomposition pathways.

AIMD calculations have been used in conjunction with experiments to study the effectiveness of Li-pretreated HC electrodes and develop a more detailed understanding of SEI formation in SIBs.[315] Systems with ether-based electrolytes exhibited better stability than those with carbonate electrolytes during experimental charge cycling, but the mechanism behind this stability was unclear. AIMD calculations revealed that tetraethylene glycol dimethyl ether (TEGDME)/Na^+ complexes expand the edges of HC layers, but do not insert between them. They also revealed that TEGDME will readily adsorb onto the HC surface, and that these adsorbed species are able to resist reduction compared to nonadsorbed species (**Figure 24**a). These findings indicate that the improved cyclability is likely due to the lower reactivity and increased SEI stability of TEGDME compared to carbonates.

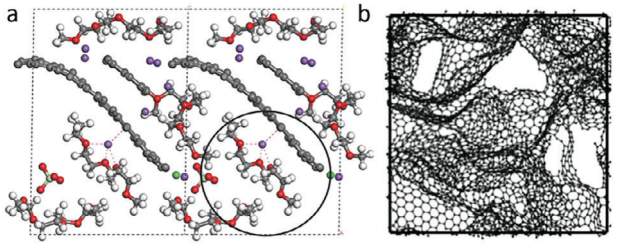

Figure 24. a) Snapshot of AIMD simulation of TEGDME at sodiated hard carbon after 45 ps. Reprinted with permission.[315] Copyright 2022, Wiley The black circle indicates where TEGDME has caused expansion of the HC edge layers b) MD-predicted model of HC structure. Reprinted with permission.[56] Copyright 2018, Wiley.

Classical molecular dynamics (MD) calculations consist of atoms and/or molecules with spring-link bonds, where the interactions between species are represented with parametrized force fields, rather than through explicit electronic contributions.[320–322] This leads to a substantial reduction in computational cost, which allows for the simulation of tens of thousands of atoms at nanosecond timescales. The larger scale enables the study of thermodynamic properties, diffusion rates, and nanometer-scale changes in surface morphology and electrolyte structure.

Experiments revealed that doping HC with nitrogen (N-HC) in SIBs leads to $a \approx$39% increase in capacity and improved cycling stability.[323] A combination of MD and DFT calculations were employed in order to understand the reason behind this promising behavior. MD calculations were performed to generate example HC geometries, which were then used as inputs for DFT calculations. DFT was then used to study the properties of N-HC and HC during sodiation. It was determined that N-HC underwent significantly less volume expansion than HC (7.9% vs 21.7%). This indicates that nitrogen doping reduces the internal stress in HC during sodiation and is responsible for the increased capacity and stability.

Recent work has combined experimental methods with MD and reverse Monte Carlo calculations in order to develop a better understanding of the binding and storage mechanisms of Na^+ in HC.[56]

XRD and neutron diffraction are the most important methods to determine the interlayer spacing, the relevance of which in sodiation can also be modeled theoretical calculation. DFT calculations can be used to determine the energy cost of Na^+ insertion into the interlayer space, as a function of the value of the interlayer spacing.[241] Such calculations reveal that above an interlayer spacing of 0.37 nm the energetic cost for Na^+ insertion declines drastically, which seems to be in line with XRD analysis.

X-Ray diffraction (XRD), neutron scattering, and pair distribution function analysis were used to study a specific HC sample. MD was then used to mimic the sintering process of HC fabrication on many different initial carbon structures, until a structure with similar density and pair distribution to experimental values was created (Figure 24b). A reverse Monte Carlo algorithm was

then used to modify the MD output in order to further improve the fit to experimental data. The resulting geometry was then analyzed in order to identify and quantify the presence of different HC structural features.

More advanced DFT approaches simulate gradually ordered graphene stack structures by machine-learning, simulating temperature annealing including defect sites, and thus generate structures which can potentially be compared with experimental XRD and small-angle X-ray or neutron scattering data in regard to the distribution of metal atoms.[324]

Additional simulations of Na^+ inserted into the final HC structure were performed in order to identify and quantify binding sites. These binding sites were then paired with energies from previous DFT calculations[325] to correlate them to the experimental charge/discharge voltage profiles. This allowed for the association of specific structural features to the sloping regions of the curve. This work also established a model to characterize HC from different sources.

Kinetic Monte Carlo (kMC) models are versatile and can be applied to a wide range of size- and timescales, depending on the properties of the system being simulated. They are often used to study atomistic behavior, where atoms and molecular beads are represented on a lattice. A set of relevant events, such as chemical reactions, and their corresponding rates must be provided as inputs for the system. The kMC model works by sequentially selecting these events based on likelihood and random number generation, and then applying to the system.[326,327] This method can be used to study morphological and compositional changes at time and length scales far beyond what is possible with AIMD or MD.

Recently, a kMC model has been developed to examine SEI growth in Li-metal systems at a level of detail far beyond prior studies.[328] In this work, electrolyte reaction pathways and barriers were supplied from DFT calculations, and the Li metal/electrolyte interface was simulated at open circuit conditions. The model accurately simulated the growth of the SEI layer and provided novel insights about the composition and distribution of species. To date, no kMC studies concerning SIBs or the HC/Na–electrolyte interface have been published.

Continuum models can also be applied to a variety of size- and timescales, depending on the system/properties of interest, and the desired level of precision. Species are represented implicitly as concentrations, rather than explicitly.[329,330] The models are based on conservation equations, used in form of species, charge, energy and momentum balances with transport and source/sink terms, e.g., from reactions. A simple schematic is shown in **Figure 25**. The recent rise of machine learning techniques has enabled the development of highly accurate continuum models by improving parametrization processes and experimental correlation, and will allow for more widespread application in the near future.[331] This is the coarsest-grained and most computationally inexpensive method that we will discuss, it can provide spatially- and time-dependent system properties at larger scales than any of the previously mentioned methods. Continuum models are often used in conjunction with experiments, which allows for the identification of battery properties, such as SEI thickness, and processes, such as reaction kinetics.

Continuum modeling has been employed to study SEI behavior during charge cycling of a Li-ion/graphite system.[332] This

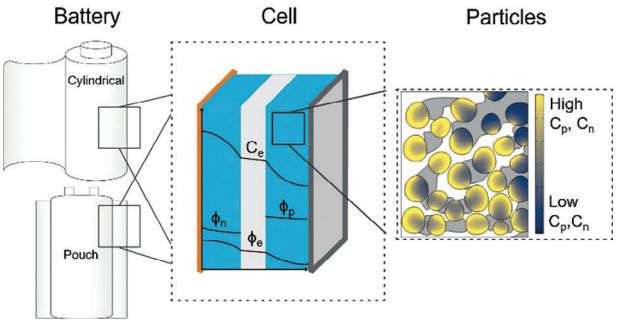

Figure 25. Sketch of the battery components at different scales. A battery is composed of multiple layers of single cells, which in turn are made of a porous structure, composed of electrode particles (yellow/black) held together by a conductive binder (gray), filled with a liquid electrolyte (white). The diagram also illustrates the electrochemical variables in the model: ion concentration in the electrolyte C_e, electrolyte potential ϕ_e, electrode potentials ϕ_n and ϕ_p and concentration of intercalated lithium C_n and C_p (yellow/black colormap). Reproduced under terms of the CC-BY license.[330] Copyright 2022, Planna et al. Elsevier Ltd.

model was able to determine a previously unknown mechanism of capacity fade and provide an explanation for the linear growth of the SEI. Other models have worked to model SEI growth[333] and aging[334] behaviors. Tanaka et al. have used continuum modeling to study the role of mechanical strain in SEI failure during the charging of lithium–silicon batteries.[335] The application of continuum models for similar studies in SIBs is expected in the near future.

Modeling can also be used to study vast amounts of data and systems, that would otherwise be impossible experimentally. Continuum models[336,337] have been used to predict optimal configurations, operating conditions, and safety properties at the cell and stack level. Dynamic multiscale models can be used to expedite the search for new battery materials by examining thousands of possible electrolytes and chemistries in order to narrow down the promising candidates for experimental testing.[338,91] The results from experimental studies of these species can then be fed back into the model in order to improve the predictability.[339,340]

Overall, computational modeling allows for the study of systems at scales and conditions that are not feasible with experiments. It serves to compliment and bridge together all of the previously discussed methods in order to develop a comprehensive understanding from the atomic scale to the industrial scale. We will discuss this in more detail in the next section.

4. Integration across Methods

The performance of SIBs and the behavior of the SEI/HC interface is influenced by the properties of every part of the electrochemical cell, and by phenomena occurring across many different time- and length-scales. The study of individual, isolated parts of the battery, at limited scales, provides information that is not necessarily accurate for the full system. All the methods we have discussed above are powerful, and provide valuable insight, but are limited in scope and scale when applied individually. In this section, we discuss possible approaches for integrating these methods together in order to overcome this limitation and develop a more holistic understanding of the HC interface and SIB

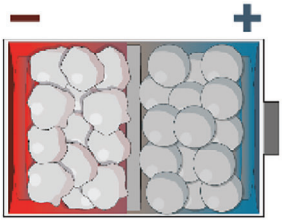

Figure 26. Schematic of general battery system, viewed at a "large" scale, with little fundamental information.

behavior. We include **Figures 26–31** as a visual representation of how these integrated methodologies build this understanding, starting from the full cell.

Operando methods are vital for obtaining insight at practical size- and timescales but are typically limited to seeing only a portion of the cell function/behavior/properties. They can be paired with other operando methods in order to overcome this and develop a broader understanding of the cell properties and performance. EIS analysis is almost always used in combination with other methods. It pairs very well with OEMS because both methods work operando and can be performed in parallel on the same system.[341] These measurements can be used to correlate the reactions observed in OEMS to changes in larger-scale properties, such as SEI resistance and the degradation state of the cell. The substrate curvature technique works also operando and is able to detect processes at the interface/SEI,[342] this can be coupled with the OEMS/IS methods to correspond SEI growth to specific reactions and changes in battery performance.

The numerous materials composing a battery cell undergo a number of physicochemical reactions, each of which induce a measurable change in Gibb's free energy. Single electrode microcalorimetry can detect the precise times when these changes occur but is not able to determine information about the reaction itself. OEMS/EIS/CV techniques can be used to supplement microcalorimetry measurements and determine precise timelines for reactions and develop clearer understanding of the relationship between specific reactions and changes in cell behavior.[269]

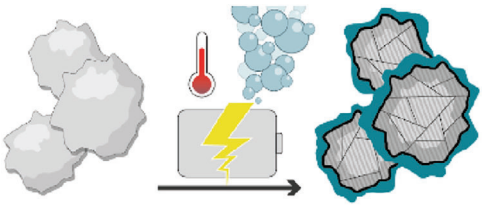

Figure 27. Schematic of larger-scale information that can be obtained by operando methods, the growing green border represents SEI growth, the thermometer, bubbles, and battery represent data available to microcalorimetry, OEMS, and EIS, respectively.

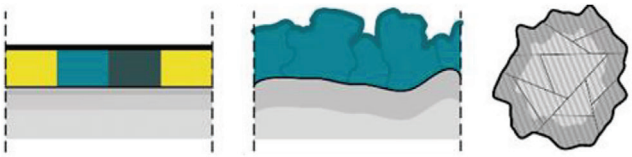

Figure 28. Schematics of more precise data that can be obtained by pairing methods that correspond to the same properties (chemical/structural) at different scales. The left image represents the SEI with detailed chemical information, but no structural information. The middle image represents the SEI with detailed structural information, but no chemical information. The right image represents detailed structural information about the HC electrode particles, without information on the SEI.

Operando methods are typically too coarse-grained to develop detailed conclusions about underlying phenomena, but they can be combined with more precise in situ or postmortem techniques to create a holistic picture of the processes under investigation. Operando measurements can be used to determine the points of time during charge cycling when significant events occur. In situ and postmortem techniques can then be applied to the cell at these points to determine the underlying behavior and mechanisms. OEMS is able to study battery reactivity operando but faces challenges with the precise determination of the reaction chemistry and is unable to distinguish the component of the cell where reactions occur. OEMS measurements are often used in combination with surface chemistry analysis methods, such as XPS, to correlate the observed reactivity and degradation products to their respective electrodes and location thereon. By extension, all of the operando methods discussed in the previous paragraph can be paired with detailed chemical and structural information from surface sensitive techniques like SEM/SPM/XPS/ToF-SIMS/DFT[228,269,342–345] in order to determine the specific underlying phenomena that correspond to the overall cell performance.

In the case of STEM, normally high-energy electron beams are used, so that the electron dose dictates whether the structure is changed. Battery materials can be beam-sensitive, i.e., their structure may be disrupted (amorphization) or destroyed, and thus the conductivity can be altered.[346]

Formation of secondary electrons during SEM operation is always paired with the emergence of element-specific X-rays providing information on segregation, diffusion or transformation of active species stemming from electrochemical processes.[150] While this process does not harm the sample surface, the FIB tomography option cleaves the sample surface and thus destructively provides insights into the bulk material.

The substrate curvature method probes the entire bulk simultaneously, and the measured stresses strongly depend on the volumetric changes and phase transformations of crystalline structures. XRD is able to observe these phenomena and can be combined with substrate curvature to obtain high-speed and high-resolution stress/strain and local crystal structure data. XRD can also be used to relate specific structural changes to energy changes observed with microcalorimetry.[347] AFM combined with OEMS/EIS/CV gives access to in situ and operando studies, providing correlated structure-reactivity information.[228]

The nanostructure of the SEI, in addition to its chemical properties, has a direct impact on its stability and passivation properties.[348]

XPS allows for precise qualitative and quantitative chemical analysis of interphases but cannot easily differentiate between the organic species that are commonly produced during electrolyte decomposition. It is also limited in scale; only small regions of a surface can be studied, and only the first few nanometers of a surface emit photoelectrons, making it very sensitive to the upper layers of the surface.

XPS can give information about the chemical and the oxidation state as well as on the electronic structure. But it is not possible to detect where the accumulation of certain elements or the change in the electronic structure appears. Here, ToF-SIMS and STEM deliver the advantage for combining spectroscopy and spectrometry on the scales of microns with real-space imaging at the atomic-scale.[349] ToF-SIMS suffers from the matrix effect, which only allows for qualitative and semi-quantitative studies without complex calibration routines; XPS does not suffer from this effect, and thus can obtain complimentary quantitative data for the ToF-SIMS study.

Given the achievable spatial resolution and the fact that in situ measurements can be performed, AFM and other methods from the family of SPM techniques can contribute and complement microscopic methods like SEM that are short of 3D morphology information and are usually only performed in high vacuum.[228]

Reaching even smaller length-scales, STEM experiments can be enabled by FIB technique which is ensuring the necessary sample quality. In the case of Na-based batteries the preparation must be done under cryo-conditions to avoid diffusion of Na^+ due to the influence of the ion-beam.[350] Solid-state NMR and MRI are able to compliment and validate XRD, SEM, TEM, and XPS characterization results.[296]

XRD analysis is mainly used to study the atomic scale structure of the HC in regard to the sodiation/desodiation processes and is thus complementary to other methods being sensitive to local order and defects. In particular, the combination of Raman spectroscopy and XRD, especially if performed in situ or operando, shows high promise to unravel fine details of changes in periodic order as well as on the relevance of defect sites.[28] For instance, the layer extension L_a can be assessed by XRD as well as by Raman spectroscopy. Moreover, such methodology has already been performed on hard carbon nano fibers used for sodiation studies, revealing insight into the different storage mechanisms.[241] Here, the changes in the XRD data upon sodiation were accompanied by a red-shift of the G-band in Raman spectroscopy, reflecting elongation of the C-C blond length.[351] Also, Also, the D-band declines during sodiation,[241] which may be caused by Na^+ adsorption on surface of graphene stacks, and which thus may complement small-angle X-ray scattering analysis[245] probing the pore filling process.

Different techniques can also be paired together to overcome practical limitations of study, such as constraints on size, material properties, and sample environment.

On the scales of below 100 nm up to 100 mm, ToF-SIMS provides information about lateral and in-depth distribution of substructured surface layers. The ballistic impact on the surface during the ToF-SIMS ionization process can damage (alter) some sensitive chemical compounds. Surface sensitive techniques, like XPS, can be applied to obtain the initial chemical state, before the sample is damaged. Here, the chemical states must be investigated before the sample is damaged by the primary ion beam from the ToF-SIMS.

ToF-SIMS and standard XPS measurements traditionally require UHV conditions, which disallows the use of liquid-containing samples, and thus can only be used postmortem or loosely for in situ examination (when samples are cryogenically frozen during analysis). Here, (near) ambient pressure XPS measurements provide a potential pathway to obtain more realistic data on solid/liquid interfaces in batteries with and without electrochemical bias.[352,353] Other liquid- and gas-sensitive methods, such as OEMS, can provide information about the remaining reaction products from initial SEI formation as well as continuous degradation.

The geometry of the investigated surface plays a significant role as the quality of obtained information decreases and eventually vanishes depending on surface roughness. Topographic effects limiting the resolution of ToF-SIMS measurements can be related to morphology investigations by SPM techniques and SEM imaging in order to regain realistic information.

Computational models are paired with many different experimental methods in order to provide detailed insight on processes that are otherwise too fast, small, or complex, to be observed experimentally.

DFT is often paired with chemical analysis techniques, such as OEMS and XPS, in order to delineate the reactive species and develop reaction mechanisms for the experimentally-observed products.[354,355] AIMD and DFT calculations are also frequently used in combination with XPS and Raman spectroscopy in order to determine the surface conditions and reaction mechanisms that produce the SEI species observed experimentally.[356,357]

Larger scale simulations can provide insight on structural data and transport processes. SPM techniques can be paired with MD to determine the interfacial nanostructures and complex molecular phenomena that contribute to more stable electrodes.[358] MD simulations can also provide atom-scale transport behavior and diffusion rates to correspond with solid state NMR studies.[359] MD and reverse Monte Carlo calculations can be coupled with XRD in order to develop an atomistic understanding of the HC microstructure and Na^+ insertion behavior. DFT calculations can then determine the specific HC characteristics and structures that contribute to more effective ion storage.[56]

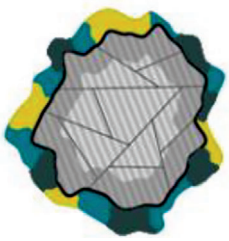

Figure 29. Schematic representation of the SEI on a HC particle as can be derived from experiments.

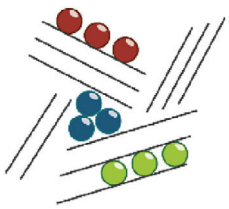

Figure 30. Atomic scale information on the different types of Na^+ insertion behavior in HC: Metallic pore filling (blue), intercalation between layers (green) and adsorption on edges (red).

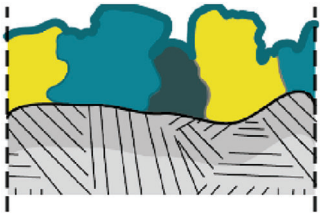

Figure 31. Representation of SEI including detailed structural and chemical information, on a particle with well-defined structure.

Computational models can also be applied to develop a clearer physical understanding of operando techniques. EIS is often difficult to precisely interpret due to the overlapping of different frequency regions (processes) and sensitivity to minute changes in the cell. Witt et al. have developed a continuum model of experimental EIS measurements, as well as discharge in full- and half cells, in order to correlate experimentally observed cell behavior to specific SEI properties.[334] This model is able to overcome the challenge of experimentally overlapping data and delineate individual ongoing processes in the cell.

Multiple modeling methods can be combined in order to bridge the precision of finer methods to the scale of coarser methods. kMC methods can be coupled with continuum models to allow for atomistic insight and reaction information to be obtained at large timescales.[360]

Advances in processing hardware and machine-learning are allowing for modelling to be applied more rigorously than ever before. The availability of robust DFT parameters is often the bottleneck for larger-scale methods like MD and kMC. Machine learning methods and kMC principles can be applied to DFT calculations in order to accelerate the search for these reaction barriers and parameters.[361] Machine learning can also be applied to accelerate the aforementioned search for electrolyte and electrode materials, and to improve the precision/accuracy of experiment-based models, like those of EIS.[362,363]

The integration of all these methods, both experimental and theoretical, enables the full understanding of the fundamental properties of the HC interface and its relationship with the overall performance of SIBs.

5. Conclusion

The major issues currently limiting SIB technologies are capacity fade and cell degradation, primarily due to instabilities in the HC electrode-electrolyte interface that induce the formation of ineffective SEIs. These instabilities are simultaneously influenced by processes that occur across many timescales at all parts of the electrochemical cell. The properties of the electrolyte and HC anode have the strongest influence on the stability of the SEI, and the large inconsistency between different HC samples makes it even more difficult to obtain clear and reliable information (Figure 30).

Electronic information about the battery cell is provided by EIS measurements, while the single electrodes can be probed by SPM techniques. Continuum models are able to simulate and clarify this data.

Chemical information about the gas-phase reaction products of processes occurring during formation of the SEI in electrochemical cells is provided by OEMS, while GC-MS or NMR provide insights in the liquid-electrolyte phase. Microcalorimetric measurements of thermodynamic data can help pinpoint when different chemical reactions occur. XPS, ssNMR, and ToF-SIMS give detailed information about the solid products, including chemical identity as well as lateral and depth profiles of chemical compounds. DFT, AIMD, and kMC calculations provide atom-scale insight on reactivity.

Physical events that generate changes in the Gibbs free energy of the system can also be detected by microcalorimetric studies. Operando stress curvature measurements reveal information about the fundamental mechanical properties of the electrode and SEI over the course of cycling. SEM can help visualize the difference between separate states of a single electrode. STEM and XRD investigations show the smallest entity of physical-structural bulk properties, namely the crystal structure. MD calculations are able to determine atomic structures and ionic transport behavior.

The techniques discussed here do not constitute a comprehensive list; there are many other powerful methods available for the study of battery systems, including: accelerating rate calorimetry,[364] differential scanning calorimetry,[365] dilatometry,[366] cyclic voltammetry,[367] and many more.[368–372] The methods and combinations we selected for this perspective are intended to provide an outline of the different scales and properties that can be studied in SIBs, in order to provide a clear overarching idea for new researchers and are summarized in **Table 2**.

Herein, we provide an overview of necessary interconnectable techniques aimed at the multiscale investigation of the SEI on HC electrodes in SIB. There is no single method that is capable of investigating all of these scales simultaneously. Multiscale studies, that account for simultaneous processes, multiple parts of the cell, and use consistent HC reference materials, are needed in order to provide a complete picture of SIB behavior. In situ and operando measurements of the processes in SIBs and their effects must be correlated to their underlying chemical and physical phenomena at all scales, from cell-level to atomistic, by coupling multiple experimental and computational methods in single studies. Continuous collaboration between well-connected academic groups with complementary expertise is needed to overcome the logistical challenges posed by multiscale investigations of chemically consistent systems.

6. Experimental Section

Substrate Curvature: For the operando stress measurement, a borosilicate glass cantilever (155 µm thick, 14 mm long and 5 mm wide) was used. It was coated with a 25 nm tungsten film that served as a current collector and then spray coated with a hard carbon composite electrode. The coating consisted of 85 % hard carbon (Kuranode hard carbon 5 µm type II, Kuraray, Japan), 5 % CMC binder and 10 % conductive carbon (Vulcan XC72R). The curvature measurement was performed in a test setup that was developed within the group.[106] It is optimized for measurements inside a custom-made electrochemical test cell and exhibits accurate temperature stabilization. The cantilever was clamped in the test cell, which was then filled by about 0.6 mL of electrolyte containing 1 M $NaPF_6$ dissolved in EC:PC (1:1). It contained less than 3 ppm of water (Karl Fischer Titration) after drying for more than a week with 4 Å

Table 2. List of the herein described analytical methods for the analysis of sodium-ion batteries with a focus on SEI investigation.

Method	Requirements	Obtained info/strength	Missing info	Complementary method filling the gap	Scale/Resolution	In situ / operando / postmortem	Time/difficulty
OEMS	Cell or setup allowing to sample produced gas	Chemical decomposition mechanisms, progression of degradation processes as function of operating conditions and cell design	Structural info, solid/liquid degradation products, single degradation kinetics	Ab initio and continuum simulations for kinetics/mechanisms, NMR for electrolyte composition, ToF-SIMS/XPS for SEI composition	Ideal and technical electrode level, small and large cells	Operando	Seconds to hours difficulty to quantify single reaction rates
EIS	Potentiostat with electrochemical impedance module	In theory fundamental electrochemical parameters, e.g., double layer capacitance, diffusion coefficients, reaction kinetics)/fast data acquisition & quick to setup	Electrode morphologies	XPS, SPM, FIB/SEM, microcalorimetry, simulations	From cell to pack level (coin cells to pouch/prismatic formats)	In situ (stationary EIS)	Minutes to hours/easy for simple spectra comparison challenging for in-depth analysis (particularly batteries)
Substrate curvature	Sample rigidly attached to a ceramic substrate (purely elastic)	Mechanical stress caused by electrode operation/electrochemical reactions with very high sensitivity	Structural and chemical info	XRD, XPS, TOF-SIMS, SECM	Sample dimensions: 5– 20 mm; resolution. changes on the level of sub-monolayers	Operando	Sample and cell preparation ≈1 d, measurement time minutes up to weeks
ToF-SIMS	Smooth surface, solid, UHV	Highly resolved lateral/3D element/fragment distribution, sensitivity	Chemical info	XPS, SPM, GC EIS	50 nm–several mm	Postmortem	Measurement times from minutes to days, very expensive
XPS/HAXPS	Solid, UHV, preferably smooth	High surface sensitivity, qualitative and (semi)quantitative chemical info, oxidation states, chemical bonding, electronic structure	Lateral distribution	ToF-SIMS, SPM, GC, OEMS	lateral ≈5– 500 µm vertical ≈ 1– 50 nm (with hard X-rays)	Postmortem, for solid state even operando, with liquids: ambient -pressure XPS for in situ/operando	Minutes to hours, synchrotron measurements only proposal-based
FIB/SEM	Protective Pt coatings, sample preparation like embedding for tomography	Porosity, microstructure, coupled with EDS and EBSD additional information on element composition, insights on crystallographic information, e.g., grain orientations and grain architectures	Chemical info	ToF-SIMS, XPS, STEM	≈10 nm– 400 µm	Postmortem	Hours-days for sample preparation, actual measurement: hours, 3D reconstruction: hours to days

(*Continued*)

Table 2. (Continued).

Method	Requirements	Obtained info/strength	Missing info	Complementary method filling the gap	Scale/Resolution	In situ / operando / postmortem	Time/difficulty
SPM	Preferably smooth surface	Surface morphology, ionic fluxes, electrochemical properties, electrical conductivity, electrochemical activity, nanomechanical properties	Chemical info	XPS, STEM, SEM,	>0.1 nm lateral-res. few Å height-res.	In situ, postmortem	Minutes to hours
XRD	Sample amount ≈50 mg at minimum (powder); for in situ experiments special cells being transparent for X-rays or neutrons	Crystallographic info mainly on HC: interlayer spacing, dimension and disorder of the graphene stacks; presence of elemental Na.	Chemical info	Raman spectroscopy, XPS	Few Å to nm	In situ, operando, postmortem	Minutes to hours
STEM	Solid state sample, high vacuum compatible (except with dedicated holder), to be thinned to electron transparency	2D/3D nanoscale morphology, atomic structure, semiquantitative nanoscale chemical composition, nanoscale oxidation state	Bulk properties, quantitative chemical composition, light element detection, surface sensitivity, electrochemical characterization	Light optical microscopy, SEM, FIB, XPS, ToF-SIMS	0.1 nm– ≈30 µm	Postmortem, with dedicated holders also in situ or operando	Sample prep.: hours–days measurements: hours–days data analysis: hours–days
Microcalorimetry	Thin electrode	Heat evolution during electrochemical reaction; reaction entropy	Structural info, chemical info	SPM, XRD, EIS, XPS	1–10 mm	In situ	Complete experiment: days to weeks, single heat measurement < 10 s
NMR	Superconducting homogeneous magnet with electronics and detectors used to analyze materials of about 1 to 100 mg (depending on density and sample-holder/rotor size)	Site specific differentiation/quantification, local structure, mobility, formation, transfer, (electrochemical and side) reaction, and degradation mechanisms	Interphases, ionic states of elements, nonmagnetic sites (nuclei)	XRD, OEMS, GC, SEM, TEM, XAS, PDF, XPS, and EIS	Electrode level to cells (usually plastic bag cell) with local structure resolution below 1 nm	In situ, operando and postmortem	Minutes to hours
Modeling	Different modeling techniques are limited to different scales. Many techniques require significant amounts of input data specific to the system in question	Degradation, transport and insertion mechanisms and kinetics, SEI evolution and degradation on HC as function of material and operation, model design can be tailored for research question	Structural and chemical info at different scales	All experimental measurements	From nm to cm	N/A	varies significantly depending on modeling method

molecular sieve (Sigma-Aldrich). Na metal foils served as counter and reference electrodes. The test cell was hermetically sealed by mounting a sapphire window to its front and then moved from the argon filled glove box into the curvature setup. Electrochemical experiments were performed using a commercial battery cycler (VMP3, Bio-Logic SAS). During the stress measurement, two laser beams (Schäfter + Kirchhoff 51nanoFCM) entered and left the test cell through the transparent sapphire window and were reflected at the back of the cantilever. To minimize stress concentrations related to clamping, two laser beams were used. The position of both reflected beams was recorded by a CMOS camera with a 1'' chip (Pixelink PL-B782F) located at a distance of 208 mm from the cantilever. A Labview program recorded the data from the camera for both laser spots (center of mass of the intensity distribution) at 40 Hz as well as the electrochemical data from the VMP3. Simple trigonometry was used to calculate the deflection angles and radius of curvature of the cantilever in the region between both laser beams. The composite electrode contained materials with very different thermal expansion coefficients (polymer, metal, and ceramic). To suppress curvature due to temperature, the setup was located inside a thermally isolated box with a Peltier-based active temperature control (also controlled by the Labview program) that limits temperature fluctuations below ± 10 mK.

OEMS: For the OEMS measurements a test setup developed by the own group was used.[85] In the PAT-cell gas by EL-cell was assembled in a glovebox under argon gas with an electrode (consisting of 85% hard carbon, 10% carbon black and 5% PVDF binder), an NVP electrode by the Binder Group and 150 µL of 1 M $NaPF_6$ in EC:PC (1:1) electrolyte. The insulation sleeve also contained a sodium reference ring.

The cell was attached to a constant argon flow via a mass flow controller (EL-Flow Prestige FG-200CV, BRONKHORST) to the mass spectrometer (Omnistar GSD 320 OC2 (PTM81217121), PFEIFFER VACUUM). Measurement data were recorded with the proprietary software PV MassSpec. The potentiostat (Gamry Interface 5000, GAMRY Instruments) was used to conduct two formation cycles (charge and discharge) at 1/10C.

EIS: Electrochemical impedance spectroscopy (EIS) measurements were performed on a 50×10^{-3} M aqueous solution of $K_4Fe(CN)_6/K_3Fe(CN)_6$ with an additional 10×10^{-3} M K_2SO_4 supporting electrolyte. The measurement was carried out under ambient conditions in a three-electrode setup (10 mL glass vessel with PTFE lid to fix electrodes) using a Biologic SP-200 potentiostat. Reference electrode: Ag/AgCl in 3 M KCl; working electrode: Pt disc electrode (1.6 mm diameter) and counter electrode (Pt wire). Data analysis performed with RelaxIS3 (rhd instruments, version 3.0.20 Build 19).

ToF-SIMS: HC electrodes with a mass loading of 1.5 mg cm^{-2} for time-of-flight secondary ion mass spectrometry (ToF-SIMS) measurements were electrochemically cycled versus Na-metal in PC electrolyte with 1 M $NaClO_4$ conducting salt and 2% FEC additive at 0.1C. The cells were disassembled and handled under argon atmosphere in a glovebox and transported in a VCT 500 shuttle (Leica Microsystems, Wetzlar, Germany) under inert gas conditions to the SIMS machine. ToF-SIMS depth profiles were performed in positive ion mode using a ToF.SIMS 6 (Iontof GmbH, Muenster, Germany) machine, which is equipped with a Bi nanoprobe analysis gun and was operated at 15 keV. A pulsed Bi_3^+ primary ion beam scanned a surface area of 50×50 µm^2 with 128×128 pixels at a cycle time of 100 µs until a total dose density of 2.74×10^{13} ions cm^{-2} was reached. Charge compensation was carried out with a low energetic electron flood gun. The achieved mass resolution was better than $m/\Delta m$ = 6000 (FWHM) at m/z 62.982 (Na_2OH^+). For data analysis SurfaceLab 7.3 software (IONTOF GmbH, Muenster, Germany) was used by which the surface spectra were calibrated to the mass signals of the fragments Na_2OH^+, Na_2F^+ and $Na_2CO_3^+$.

FIB/SEM Tomography: FIB/SEM tomography was performed using a Helios Nanolab 600 (Thermo Fisher Scientific Inc., USA). The gallium ion beam was operated at 30 kV. The HC particle within a composite electrode was covered with a protective platinum layer via ion beam induced deposition (IBID) using the precursor methylcyclopentadienyl trimethyl platinum ($C_9H_{16}Pt$). Cross-section and trenches alongside the particle were prepared prior to FIB/SEM tomography. Imaging and slice and view were conducted using the software package "Auto Slice & View G3" (version 1.0.0.1236, Thermo Fisher Scientific Inc., USA). Secondary electron images were acquired at 0.69 nA and 3 kV with a pixel size of 16.6×16.6 nm^2 using immersion mode and the through-the-lens-detector (TLD). After each image a slice of 30 nm thickness was removed from the particle front, in total a stack of 332 images was acquired.

For the 3D reconstruction of the particle, the obtained image stack was processed using Avizo Lite (version 9.1.0, Thermo Fisher Scientific Inc., USA), i.e., the images were manually aligned and filtered using edge-preserving smoothing, binarized and segmented using a threshold. The segmentation of pore space within the HC particle was revised manually afterwards.

SPM: The approach curves and corresponding SECM mappings of the HC composite electrodes (pristine and 40 cycles in 1 M $NaClO_4$/PC, 0.1 C) were recorded with 0.01 M ferrocene as redox mediator in acetonitrile/0.1 M $TBAPF_6$. A Pt UME (r = 1.5 µm) was used as the working electrode, a leakless Ag/AgCl (eDAQ Pty Ltd, Australia) electrode served as the reference and a Pt wire as the counter electrode. All measurements were controlled with the Sensolytics SECM software (version 2.2.3.3, Sensolytics GmbH, Germany). A potential of 0.5 V was applied at the UME tip. The UME was approached with 2 µm s^{-1} toward the HC composite electrode surface at three positions for tilt correction. Afterwards, a mapping of 100×100 µm^2 was recorded with a step size of 3 µm and tip velocity of 2 µm s^{-1}. After the mapping, approach curves were performed with the same parameters as described above.

XPS: X-ray photoelectron spectroscopy (XPS) measurements were carried out in a commercial UHV system (SPECS) with a base pressure of 2×10^{-10} mbar. It consists of two chambers, one containing an Aarhus-type STM/AFM system (SPECS Aarhus SPM150 with a Colibri sensor), the other one is equipped with an X-ray source (SPECS XR50, Al-K_α and Mg-K_α), a He lamp (SPECS UVS 300) and a hemispherical analyzer (SPECS, DLSEGD-Phoibos-Has3500) for XPS and UPS measurements. The XP spectra were recorded using monochromatized Al K_α radiation ($h\nu_0$ = 1486.6 eV) at a power of 400 W (U = 15 kV, I = 26.7 mA), with a pass energy of 20 eV for all detail spectra. All spectra were recorded at an electron emission angle of 0° with respect to the surface normal. The binding energy (BE) scale was calibrated by setting the position of the main C 1s peak of the substrate to 284.6 eV.

Samples for XPS measurements were prepared by carbon spray deposition on a Cu foil,[133] which was glued with conductive silver paste on the Ta sample holder. The sample was then transferred to the spectrometer in a hermetically sealed transport box excluding contact to air and introduced via a load lock into the UHV system. Afterward, the sample was heated to 300 °C (measured at the manipulator) to remove volatile contaminants.

Acknowledgements

D.S. and K.H. contributed equally to this work. This work contributes to the research performed at CELEST (Center for Electrochemical Energy Storage Ulm-Karlsruhe) and was funded by the German Research Foundation (DFG) under Project ID 390874152 (POLiS Cluster of Excellence). The authors extend the thanks to Elisa Monte for her valuable contribution in creating the TOC figure for this paper.

Open access funding enabled and organized by Projekt DEAL.

Conflict of Interest

The authors declare no conflict of interest.

Keywords

hard carbon, solid electrolyte interphase, multiscale, SEI, sodium-ion battery

Received: August 25, 2023
Revised: November 14, 2023
Published online:

[1] United Nations Treaty Collection, https://treaties.un.org/Pages/ViewDetails.aspx?src=TREATY&mtdsg_no=XXVII-7-d&chapter=27&clang=_en (accessed: May 2023).
[2] Critical Raw Materials Resilience: Charting a Path Towards Greater Security and Sustainability, https://ec.europa.eu/docsroom/documents/42849 (accessed: April 2023).
[3] V. Etacheri, R. Marom, R. Elazari, G. Salitra, D. Aurbach, *Energy Environ. Sci.* **2011**, *4*, 3243.
[4] R. Zhao, S. Zhang, J. Liu, J. Gu, *J. Power Sources* **2015**, *299*, 557.
[5] X. Gao, H. Liu, W. Deng, Y. Tian, G. Zou, H. Hou, X. Ji, *Batteries Supercaps* **2021**, *4*, 1657.
[6] M. Á. Muñoz-Márquez, M. Zarrabeitia, S. Passerini, T. Rojo, *Adv. Mater. Interfaces* **2022**, *9*, 2101773.
[7] H. Pan, Y.-S. Hu, L. Chen, *Energy Environ. Sci.* **2013**, *6*, 2338.
[8] D. H. P. Kang, M. Chen, O. A. Ogunseitan, *Environ. Sci. Technol.* **2013**, *47*, 5495.
[9] K. M. Abraham, *ACS Energy Lett.* **2020**, *5*, 3544.
[10] C. Delmas, *Adv. Energy Mater.* **2018**, *8*, 1703137.
[11] F. Xie, Z. Xu, Z. Guo, Y. Li, Y. Lu, M.-M. Titirici, Y.-S. Hu, in *Sodium-Ion Batteries: Materials, Characterization, and Technology* (Eds.: M.-M. Titirici, P. Adelhelm, Y.-S. Hu), John Wiley & Sons, Ltd., New York **2022**, pp. 27–59.
[12] P. K. Nayak, L. Yang, W. Brehm, P. Adelhelm, *Angew. Chem., Int. Ed.* **2018**, *57*, 102.
[13] R. C. Asher, *J. Inorg. Nucl. Chem.* **1959**, *10*, 238.
[14] M. DiVincenzo, *Condens. Matter* **1985**, *32*, 2538.
[15] Z. Wang, S. M. Selbach, T. Grande, *RSC Adv.* **2014**, *4*, 3973.
[16] J. Asenbauer, T. Eisenmann, M. Kuenzel, A. Kazzazi, Z. Chen, D. Bresser, *Sustainable Energy Fuels* **2020**, *4*, 5387.
[17] W. Luo, C. Bommier, Z. Jian, X. Li, R. Carter, S. Vail, Y. Lu, J.-J. Lee, X. Ji, *ACS Appl. Mater. Interfaces* **2015**, *7*, 2626.
[18] X. Dou, I. Hasa, D. Saurel, C. Vaalma, L. Wu, D. Buchholz, D. Bresser, S. Komaba, S. Passerini, *Mater. Today* **2019**, *23*, 87.
[19] M. Wahid, Y. Gawli, D. Puthusseri, A. Kumar, M. V. Shelke, S. Ogale, *ACS Omega* **2017**, *2*, 3601.
[20] H. Li, F. Shen, W. Luo, J. Dai, X. Han, Y. Chen, Y. Yao, H. Zhu, K. Fu, E. Hitz, L. Hu, *ACS Appl. Mater. Interfaces* **2016**, *8*, 2204.
[21] M. Thompson, Q. Xia, Z. Hu, X. S. Zhao, *Mater. Adv.* **2021**, *2*, 5881.
[22] C. Bommier, W. Luo, W.-Y. Gao, A. Greaney, S. Ma, X. Ji, *Carbon* **2014**, *76*, 165.
[23] J. Jin, Z. Shi, C. Wang, *Electrochim. Acta* **2014**, *141*, 302.
[24] F. Wu, M. Zhang, Y. Bai, X. Wang, R. Dong, C. Wu, *ACS Appl. Mater. Interfaces* **2019**, *11*, 12554.
[25] S. Komaba, W. Murata, T. Ishikawa, N. Yabuuchi, T. Ozeki, T. Nakayama, A. Ogata, K. Gotoh, K. Fujiwara, *Adv. Funct. Mater.* **2011**, *21*, 3859.
[26] Z. Hong, Y. Zhen, Y. Ruan, M. Kang, K. Zhou, J.-M. Zhang, Z. Huang, M. Wei, *Adv. Mater.* **2018**, *30*, 1802035.
[27] M. Dahbi, M. Kiso, K. Kubota, T. Horiba, T. Chafik, K. Hida, T. Matsuyama, S. Komaba, *J. Mater. Chem. A* **2017**, *5*, 9917.
[28] M. Anji Reddy, M. Helen, A. Groß, M. Fichtner, H. Euchner, *ACS Energy Lett.* **2018**, *3*, 2851.
[29] E. Peled, *J. Electrochem. Soc.* **1979**, *126*, 2047.
[30] C. Vaalma, D. Buchholz, M. Weil, S. Passerini, *Nat. Rev. Mater.* **2018**, *3*, 18013.
[31] M. Zhang, Y. Li, F. Wu, Y. Bai, C. Wu, *Nano Energy* **2021**, *82*, 105738.
[32] F. Xie, Z. Xu, Z. Guo, M.-M. Titirici, *Prog. Energy* **2020**, *2*, 042002.
[33] R. Mogensen, D. Brandell, R. Younesi, *ACS Energy Lett.* **2016**, *1*, 1173.
[34] J. Song, B. Xiao, Y. Lin, K. Xu, X. Li, *Adv. Energy Mater.* **2018**, *8*, 1703082.
[35] P. Bai, Y. He, P. Xiong, X. Zhao, K. Xu, Y. Xu, *Energy Storage Mater.* **2018**, *13*, 274.
[36] B.-H. Hou, Y.-Y. Wang, Q.-L. Ning, W.-H. Li, X.-T. Xi, X. Yang, H.-J. Liang, X. Feng, X.-L. Wu, *Adv. Mater.* **2019**, *31*, 1903125.
[37] Y. Zhang, N. Zhang, W. Chen, Z. Rao, J. Wu, L. Xue, W. Zhang, *Energy Technol.* **2019**, *7*, 1900779.
[38] Y. Zheng, Y. Lu, X. Qi, Y. Wang, L. Mu, Y. Li, Q. Ma, J. Li, Y.-S. Hu, *Energy Storage Mater.* **2019**, *18*, 269.
[39] Y. Zhu, Y. Huang, C. Chen, M. Wang, P. Liu, *Electrochim. Acta* **2019**, *321*, 134698.
[40] Y. Yang, C. Wu, X.-X. He, J. Zhao, Z. Yang, L. Li, X. Wu, L. Li, S.-L. Chou, *Adv. Funct. Mater.* **2023**, https://doi.org/10.1002/adfm.202302277.
[41] H. Li, *Joule* **2019**, *3*, 911.
[42] M. Carboni, J. Manzi, A. R. Armstrong, J. Billaud, S. Brutti, R. Younesi, *ChemElectroChem* **2019**, *6*, 1745.
[43] J. Fondard, E. Irisarri, C. Courrèges, M. R. Palacin, A. Ponrouch, R. Dedryvère, *J. Electrochem. Soc.* **2020**, *167*, 070526.
[44] M. Ma, H. Cai, C. Xu, R. Huang, S. Wang, H. Pan, Y. Hu, *Adv. Funct. Mater.* **2021**, *31*, 2100278.
[45] X. Li, X. Hu, L. Zhou, R. Wen, X. Xu, S. Chou, L. Chen, A.-M. Cao, S. Dou, *J. Mater. Chem. A* **2019**, *7*, 11976.
[46] H. Alptekin, H. Au, E. Olsson, J. Cottom, A. C. S. Jensen, T. F. Headen, Q. Cai, A. J. Drew, M. Crespo Ribadeneyra, M. Titirici, *Adv. Mater. Interfaces* **2021**, *9*, 2101267.
[47] Y. Lu, L. Wang, J. Cheng, J. B. Goodenough, *Chem. Commun.* **2012**, *48*, 6544.
[48] J. Luo, S. Sun, J. Peng, B. Liu, Y. Huang, K. Wang, Q. Zhang, Y. Li, Y. Jin, Y. Liu, Y. Qiu, Q. Li, J. Han, Y. Huang, *ACS Appl. Mater. Interfaces* **2017**, *9*, 25317.
[49] J.-Z. Guo, P.-F. Wang, X.-L. Wu, X.-H. Zhang, Q. Yan, H. Chen, J.-P. Zhang, Y.-G. Guo, *Adv. Mater.* **2017**, *29*, 1701968.
[50] T. Jin, Y. Liu, Y. Li, K. Cao, X. Wang, L. Jiao, *Adv. Energy Mater.* **2017**, *7*, 1700087.
[51] J. Deng, W.-B. Luo, X. Lu, Q. Yao, Z. Wang, H.-K. Liu, H. Zhou, S.-X. Dou, *Adv. Energy Mater.* **2018**, *8*, 1701610.
[52] E. Lee, J. Lu, Y. Ren, X. Luo, X. Zhang, J. Wen, D. Miller, A. DeWahl, S. Hackney, B. Key, D. Kim, M. D. Slater, C. S. Johnson, *Adv. Energy Mater.* **2014**, *4*, 1400458.
[53] C. Bommier, X. Ji, *Small* **2018**, *14*, 1703576.
[54] Y. Jin, P. M. L. Le, P. Gao, Y. Xu, B. Xiao, M. H. Engelhard, X. Cao, T. D. Vo, J. Hu, L. Zhong, B. E. Matthews, R. Yi, C. Wang, X. Li, J. Liu, J.-G. Zhang, *Nat. Energy* **2022**, *7*, 718.
[55] C. Bommier, T. W. Surta, M. Dolgos, X. Ji, *Nano Lett.* **2015**, *15*, 5888.
[56] T. W. Surta, E. Koh, Z. Li, D. B. Fast, X. Ji, P. A. Greaney, M. R. Dolgos, *Adv. Energy Mater.* **2022**, *12*, 2200647.
[57] D. Alvira, D. Antorán, J. J. Manyà, *Chem. Eng. J.* **2022**, *447*, 137468.
[58] X. Dou, I. Hasa, M. Hekmatfar, T. Diemant, R. J. Behm, D. Buchholz, S. Passerini, *ChemSusChem* **2017**, *10*, 2668.
[59] X.-K. Wang, J. Shi, L.-W. Mi, Y.-P. Zhai, J.-Y. Zhang, X.-M. Feng, Z.-J. Wu, W.-H. Chen, *Rare Met.* **2020**, *39*, 1053.
[60] Z.-L. Xu, G. Yoon, K.-Y. Park, H. Park, O. Tamwattana, S. Joo Kim, W. M. Seong, K. Kang, *Nat. Commun.* **2019**, *10*, 2598.
[61] M. Goktas, B. Akduman, P. Huang, A. Balducci, P. Adelhelm, *J. Phys. Chem. C* **2018**, *122*, 26816.
[62] B. Jache, J. O. Binder, T. Abe, P. Adelhelm, *Phys. Chem. Chem. Phys.* **2016**, *18*, 14299.

[63] A. A. Arie, B. Tekin, E. Demir, R. Demir-Cakan, *Waste Biomass Valorization* **2020**, *11*, 3121.
[64] A. Ponrouch, R. Dedryvère, D. Monti, A. E. Demet, J. M. Ateba Mba, L. Croguennec, C. Masquelier, P. Johansson, M. R. Palacín, *Energy Environ. Sci.* **2013**, *6*, 2361.
[65] A. Ponrouch, M. R. Palacín, *Electrochem. Commun.* **2015**, *54*, 51.
[66] Y. Huang, L. Zhao, L. Li, M. Xie, F. Wu, R. Chen, *Adv. Mater.* **2019**, *31*, 1808393.
[67] L. Shen, S. Shi, S. Roy, X. Yin, W. Liu, Y. Zhao, *Adv. Funct. Mater.* **2021**, *31*, 2006066.
[68] H. S. Hirsh, B. Sayahpour, A. Shen, W. Li, B. Lu, E. Zhao, M. Zhang, Y. S. Meng, *Energy Storage Mater.* **2021**, *42*, 78.
[69] X. Zhao, Y. Chen, H. Sun, T. Yuan, Y. Gong, X. Liu, T. Chen, *Batteries* **2023**, *9*, 226.
[70] F. A. Soto, P. Yan, M. H. Engelhard, A. Marzouk, C. Wang, G. Xu, Z. Chen, K. Amine, J. Liu, V. L. Sprenkle, F. El-Mellouhi, P. B. Balbuena, X. Li, *Adv. Mater.* **2017**, *29*, 1606860.
[71] R. Dugas, A. Ponrouch, G. Gachot, R. David, M. R. Palacin, J. M. Tarascon, *J. Electrochem. Soc.* **2016**, *163*, A2333.
[72] X. Chen, Y. Zheng, W. Liu, C. Zhang, S. Li, J. Li, *Nanoscale* **2019**, *11*, 22196.
[73] Y. Pan, Y. Zhang, B. S. Parimalam, C. C. Nguyen, G. Wang, B. L. Lucht, *J. Electroanal. Chem.* **2017**, *799*, 181.
[74] V. A. Oltean, B. Philippe, S. Renault, R. Félix Duarte, H. Rensmo, D. Brandell, *Chem. Mater.* **2016**, *28*, 8742.
[75] H. Moon, M. Zarrabeitia, E. Frank, O. Böse, M. Enterría, D. Saurel, I. Hasa, S. Passerini, *Batteries Supercaps* **2021**, *4*, 960.
[76] M. A. Muñoz-Márquez, M. Zarrabeitia, E. Castillo-Martínez, A. Eguía-Barrio, T. Rojo, M. Casas-Cabanas, *ACS Appl. Mater. Interfaces* **2015**, *7*, 7801.
[77] Y. Rangom, R. R. Gaddam, T. T. Duignan, X. S. Zhao, *ACS Appl. Mater. Interfaces* **2019**, *11*, 34796.
[78] C. Bommier, D. Leonard, Z. Jian, W. F. Stickle, P. A. Greaney, X. Ji, *Adv. Mater. Interfaces* **2016**, *3*, 1600449.
[79] A. V. Cresce, S. M. Russell, O. Borodin, J. A. Allen, M. A. Schroeder, M. Dai, J. Peng, M. P. Gobet, S. G. Greenbaum, R. E. Rogers, K. Xu, *Phys. Chem. Chem. Phys.* **2016**, *19*, 574.
[80] J. Meng, G. Jia, H. Yang, M. Wang, *Front. Chem.* **2022**, *10*, 986541.
[81] N. Schlüter, P. Novák, D. Schröder, *Adv. Energy Mater.* **2022**, *12*, 2200708.
[82] S. L. Dreyer, A. Kondrakov, J. Janek, T. Brezesinski, *J. Mater. Res.* **2022**, *37*, 3146.
[83] R. Lundström, E. J. Berg, *J. Power Sources* **2021**, *485*, 229347.
[84] C. Misiewicz, R. Lundström, I. Ahmed, M. J. Lacey, W. R. Brant, E. J. Berg, *J. Power Sources* **2023**, *554*, 232318.
[85] L. Bläubaum, Elektrochemische und gasanalytische Untersuchungen an Lithium-Ionen-Batterien, https://doi.org/10.5445/IR/1000161140https://publikationen.bibliothek.kit.edu/1000161140 (accessed: August 2023).
[86] M. Goktas, C. Bolli, E. J. Berg, P. Novák, K. Pollok, F. Langenhorst, M. v. Roeder, O. Lenchuk, D. Mollenhauer, P. Adelhelm, *Adv. Energy Mater.* **2018**, *8*, 1702724.
[87] L. Zhang, C. Tsolakidou, S. Mariyappan, J.-M. Tarascon, S. Trabesinger, *Energy Storage Mater.* **2021**, *42*, 12.
[88] E. Marelli, C. Marino, C. Bolli, C. Villevieille, *J. Power Sources* **2020**, *450*, 227617.
[89] A. J. Bard, L. R. Faulkner, *Electrochemical Methods – Fundamentals and Applications*, John Wiley & Sons, Inc., New York **2001**.
[90] T. Vidaković-Koch, T. Miličić, L. A. Živković, H. S. Chan, U. Krewer, M. Petkovska, *Curr. Opin. Electrochem.* **2021**, *30*, 100851.
[91] U. Krewer, F. Röder, E. Harinath, R. D. Braatz, B. Bedürftig, R. Findeisen, *J. Electrochem. Soc.* **2018**, *165*, A3656.
[92] A. Ch. Lazanas, M. I. Prodromidis, *ACS Meas. Sci. Au* **2023**, *3*, 162.
[93] M. Hess, *Electrochim. Acta* **2017**, *244*, 69.
[94] F. Linsenmann, D. Pritzl, H. A. Gasteiger, *J. Electrochem. Soc.* **2019**, *166*, A3668.
[95] M. Ender, A. Weber, I.-T. Ellen, *J. Electrochem. Soc.* **2011**, *159*, A128.
[96] C. Bünzli, H. Kaiser, P. Novák, *J. Electrochem. Soc.* **2015**, *162*, A218.
[97] S. Klink, E. Madej, E. Ventosa, A. Lindner, W. Schuhmann, F. La Mantia, *Electrochem. Commun.* **2012**, *22*, 120.
[98] S. Drvarič Talian, J. Moškon, R. Dominko, M. Gaberšček, *Adv. Mater. Interfaces* **2022**, *9*, 2101116.
[99] S. Drvarič Talian, J. Moškon, R. Dominko, M. Gaberšček, *ACS Appl. Mater. Interfaces* **2017**, *9*, 29760.
[100] S. J. Cooper, A. Bertei, D. P. Finegan, N. P. Brandon, *Electrochim. Acta* **2017**, *251*, 681.
[101] J. Landesfeind, J. Hattendorff, A. Ehrl, W. A. Wall, H. A. Gasteiger, *J. Electrochem. Soc.* **2016**, *163*, A1373.
[102] M. Gaberšček, J. Moskon, B. Erjavec, R. Dominko, J. Jamnik, *Electrochem. Solid-State Lett.* **2008**, *11*, A170.
[103] J. Landesfeind, D. Pritzl, H. A. Gasteiger, *J. Electrochem. Soc.* **2017**, *164*, A1773.
[104] F. Linsenmann, D. Pritzl, H. A. Gasteiger, *J. Electrochem. Soc.* **2021**, *168*, 010506.
[105] G. G. Stoney, *Proc. R. Soc. London, Ser. A* **1909**, *82*, 172.
[106] Z. Choi, D. Kramer, R. Mönig, *J. Power Sources* **2013**, *240*, 245.
[107] M. Fayette, U. Bertocci, G. R. Stafford, *J. Electrochem. Soc.* **2016**, *163*, D146.
[108] E. Chason, in *Handbook of Mechanics of Materials*, (Eds: S. Schmauder, C.-S. Chen, K. K. Chawla, N. Chawla, W. Chen, Y. Kagawa), Springer, Singapore **2019**, pp. 2051–2082.
[109] A. Mukhopadhyay, B. W. Sheldon, *Prog. Mater. Sci.* **2014**, *63*, 58.
[110] M. K. Jangid, A. Mukhopadhyay, *J. Mater. Chem. A* **2019**, *7*, 23679.
[111] M. Janzen, D. Kramer, R. Mönig, *Energy Technol.* **2020**, *9*, 2000867.
[112] S. Rakshit, A. S. Pakhare, O. Ruiz, M. R. Khoshi, E. Detsi, H. He, V. A. Sethuraman, S. P. V. Nadimpalli, *J. Electrochem. Soc.* **2021**, *168*, 010504.
[113] A. Al-Obeidi, D. Kramer, S. T. Boles, R. Mönig, C. V. Thompson, *Appl. Phys. Lett.* **2016**, *109*, 071902.
[114] A. Al-Obeidi, D. Kramer, R. Mönig, C. V. Thompson, *J. Power Sources* **2016**, *306*, 817.
[115] M. H. Tahmasebi, D. Kramer, R. Mönig, S. T. Boles, *J. Electrochem. Soc.* **2019**, *166*, A5001.
[116] V. Malav, M. K. Jangid, I. Hait, A. Mukhopadhyay, *ECS Electrochem. Lett.* **2015**, *4*, A148.
[117] J. C. Vickerman, I. S. Gilmore, *Surface Analysis: The Principal Techniques*, John Wiley & Sons Ltd., Chichester, UK **2009**.
[118] T. L. Alford, L. C. Feldman, J. W. Mayer, in *Fundamentals of Nanoscale Film Analysis*, Springer, Berlin **2007**, pp. 1–338.
[119] T. Lombardo, F. Walther, C. Kern, Y. Moryson, T. Weintraut, A. Henss, M. Rohnke, *J. Vac. Sci. Technol. A* **2023**, *41*, 053207.
[120] R. Väli, A. Jänes, T. Thomberg, E. Lust, *Electrochim. Acta* **2017**, *253*, 536.
[121] J. C. Vickerman, *Surface Analysis: The Principal Techniques*, John Wiley & Sons, Ltd, Chichester, UK **2009**.
[122] C. J. Powell, A. Jablonski, *NIST Electron Inelastic-Mean-Free-Path Database – Version 1.2*, National Institute of Standards and Technology, Gaithersburg, MD **2010**.
[123] I. Källquist, R. L. Ruyet, H. Liu, R. Mogensen, M.-T. Lee, K. Edström, A. J. Naylor, *J. Mater. Chem. A* **2022**, *10*, 19466.
[124] A. M. Andersson, A. Henningson, H. Siegbahn, U. Jansson, K. Edström, *J. Power Sources* **2003**, *119-121*, 522.
[125] V. Eshkenazi, E. Peled, L. Burstein, D. Golodnitsky, *Solid State Ionics* **2004**, *170*, 83.
[126] S. Malmgren, K. Ciosek, M. Hahlin, T. Gustafsson, M. Gorgoi, H. Rensmo, K. Edström, *Electrochim. Acta* **2013**, *97*, 23.

[127] J. Maibach, F. Lindgren, H. Eriksson, K. Edström, M. Hahlin, *J. Phys. Chem. Lett.* **2016**, *7*, 1775.
[128] F. Lindgren, D. Rehnlund, I. Källquist, L. Nyholm, K. Edström, M. Hahlin, J. Maibach, *J. Phys. Chem. C* **2017**, *121*, 27303.
[129] K. Forster-Tonigold, F. Buchner, J. Bansmann, R. J. Behm, A. Groß, *Batteries Supercaps* **2022**, *5*, 202200307.
[130] F. Buchner, K. Forster-Tonigold, T. Bolter, A. Rampf, J. Klein, A. Groß, R. J. Behm, *J. Vac. Sci. Technol. A* **2022**, *40*, 023204.
[131] M. Dahbi, T. Nakano, N. Yabuuchi, S. Fujimura, K. Chihara, K. Kubota, J.-Y. Son, Y.-T. Cui, H. Oji, S. Komaba, *ChemElectroChem* **2016**, *3*, 1856.
[132] G. G. Eshetu, T. Diemant, M. Hekmatfar, S. Grugeon, R. J. Behm, S. Laruelle, M. Armand, S. Passerini, *Nano Energy* **2019**, *55*, 327.
[133] K. Palanisamy, S. Daboss, D. Schäfer, M. Rohnke, L. Derr, M. Lang, R. Schuster, C. Kranz, *Batteries Supercaps* **2023**, 202300402.
[134] F. Buchner, K. Forster-Tonigold, J. Kim, C. Adler, J. Bansmann, A. Groß, R. J. Behm, *J. Phys. Chem. C* **2018**, *122*, 18968.
[135] L. A. Ma, A. J. Naylor, L. Nyholm, R. Younesi, *Angew. Chem., Int. Ed. Engl.* **2021**, *60*, 4855.
[136] K. Pfeifer, K. Pfeifer, S. Arnold, J. Becherer, C. Das, C. Das, J. Maibach, H. Ehrenberg, S. Dsoke, *ChemSusChem* **2019**, *12*, 3312.
[137] J. R. Fitzpatrick, S. I. R. Costa, N. Tapia-Ruiz, *Johnson Matthey Technol. Rev.* **2021**, *66*, 44.
[138] C. Kizilyaprak, J. Daraspe, B. M. Humbel, *J. Microsc.* **2014**, *254*, 109.
[139] B. Li, J. Li, S. Ikhmayies, M. Zhang, Y. E. Kalay, J. S. Carpenter, J. Hwang, S. N. Monteiro, C. Bai, J. P. Escobedo-diaz, P. R. Spena, R. Goswami, *Characterization of Minerals, Metals, and Materials 2019*, Springer International Publishing, Cham, Switzerland **2019**.
[140] C. A. Volkert, A. M. Minor, *MRS Bull.* **2007**, *32*, 389.
[141] J. I. Goldstein, D. E. Newbury, J. R. Michael, N. W. M. Ritchie, J. H. J. Scott, D. C. Joy, *Scanning Electron Microscopy and X-Ray Microanalysis*, Springer, New York, NY **2018**.
[142] T. Hsu, W. K. Epting, R. Mahbub, N. T. Nuhfer, S. Bhattacharya, Y. Lei, H. M. Miller, P. R. Ohodnicki, K. R. Gerdes, H. W. Abernathy, G. A. Hackett, A. D. Rollett, M. De Graef, S. Litster, P. A. Salvador, *J. Power Sources* **2018**, *386*, 1.
[143] R. Mahbub, W. K. Epting, T. Hsu, J. H. Mason, M. Feng, N. T. Nuhfer, H. W. Abernathy, G. A. Hackett, S. Litster, A. D. Rollett, P. A. Salvador, *J. Electrochem. Soc.* **2020**, *167*, 054506.
[144] X. Zhong, C. A. Wade, P. J. Withers, X. Zhou, C. Cai, S. J. Haigh, M. G. Burke, *J. Microsc.* **2021**, *282*, 101.
[145] L. Vásárhelyi, Z. Kónya, R. V Kukovecz, *Mater. Today Adv.* **2020**, *8*, 100084.
[146] R. Leary, P. A. Midgley, J. M. Thomas, *Acc. Chem. Res.* **2012**, *45*, 1782.
[147] T. Rodenas, G. Prieto, *Catal. Today* **2022**, *405-406*, 2.
[148] L. Holzer, M. Cantoni, in *Nanofabrication Using Focused Ion and Electron Beams: Principles and Applications* (Eds.: I. Utke, S. Moshkalev, P. Russell), Oxford University Press, Oxford **2011**, pp. 410–435.
[149] A. Ul-Hamid, *A Beginners' Guide to Scanning Electron Microscopy*, Springer International Publishing, Cham, Switzerland **2018**.
[150] R. Wirth, *Chem. Geol.* **2009**, *261*, 217.
[151] O. Furat, D. P. Finegan, D. Diercks, F. Usseglio-viretta, K. Smith, *J. Power Sources* **2021**, *483*, 229148.
[152] R. Moroni, S. Thiele, *Ultramicroscopy* **2020**, *219*, 113090.
[153] M. Ender, J. Joos, T. Carraro, E. Ivers-Tiffée, *Electrochem. Commun.* **2011**, *13*, 166.
[154] M. Klingele, R. Zengerle, S. Thiele, *J. Power Sources* **2015**, *275*, 852.
[155] T. Philipp, G. Neusser, E. Abouzari-Lotf, S. Shakouri, F. D. H. Wilke, M. Fichtner, M. Ruben, M. Mundszinger, J. Biskupek, U. Kaiser, P. Scheitenberger, M. Lindén, C. Kranz, *J. Power Sources* **2022**, *522*, 231002.
[156] J.-H. Lee, J. Kim, M. H. Jeong, K. H. Ahn, H. L. Lee, H. J. Youn, *J. Power Sources* **2023**, *557*, 232552.
[157] M. Osenberg, A. Hilger, M. Neumann, A. Wagner, N. Bohn, J. R. Binder, V. Schmidt, J. Banhart, I. Manke, *J. Power Sources* **2023**, *570*, 233030.
[158] T. Sardhara, R. C. Aydin, Y. Li, N. Piché, R. Gauvin, C. J. Cyron, M. Ritter, *Front. Mater.* **2022**, *9*, 1.
[159] M. Čalkovský, E. Müller, M. Meffert, N. Firman, F. Mayer, M. Wegener, D. Gerthsen, *Mater. Charact.* **2021**, *171*, 110806.
[160] J. R. Wilson, J. S. Cronin, S. A. Barnett, S. J. Harris, *J. Power Sources* **2011**, *196*, 3443.
[161] B. Song, T. Sui, S. Ying, L. Li, L. Lu, A. M. Korsunsky, *J. Mater. Chem. A* **2015**, *3*, 18171.
[162] R. Scipioni, P. S. Jørgensen, D. T. Ngo, S. B. Simonsen, Z. Liu, K. J. Yakal-Kremski, H. Wang, J. Hjelm, P. Norby, S. A. Barnett, S. H. Jensen, *J. Power Sources* **2016**, *307*, 259.
[163] N. Lin, Z. Jia, Z. Wang, H. Zhao, G. Ai, X. Song, Y. Bai, V. Battaglia, C. Sun, J. Qiao, K. Wu, G. Liu, *J. Power Sources* **2017**, *365*, 235.
[164] S. Sailer, M. Mundszinger, J. Martin, M. Mancini, M. Wohlfahrt-Mehrens, U. Kaiser, *Micron* **2023**, *166*, 103398.
[165] Z. Liu, Y. C. K. Chen-Wiegart, J. Wang, S. A. Barnett, K. T. Faber, *Microsc. Microanal.* **2016**, *22*, 140.
[166] M. Ghadban, M. Sabharwal, C. Rea, X. Li, A. E. Goode, M. Smith, C. Murphy, M. Secanell, *J. Power Sources* **2023**, *562*, 232745.
[167] L. Almar, J. Joos, A. Weber, E. Ivers-Tiffée, *J. Power Sources* **2019**, *427*, 1.
[168] T. Hutzenlaub, S. Thiele, N. Paust, R. Spotnitz, R. Zengerle, C. Walchshofer, *Electrochim. Acta* **2014**, *115*, 131.
[169] F. Cadiou, T. Douillard, F. Willot, J.-C. Badot, B. Lestriez, E. Maire, *J. Electrochem. Soc.* **2020**, *167*, 140504.
[170] J. Joos, A. Buchele, A. Schmidt, A. Weber, E. Ivers-Tiffée, *Energy Technol.* **2021**, *9*, 2000891.
[171] A. Etiemble, A. Tranchot, T. Douillard, H. Idrissi, E. Maire, L. Roué, *J. Electrochem. Soc.* **2016**, *163*, A1550.
[172] C. Zhu, S. Chen, K. Li, Z. W. Yin, Y. Xiao, H. Lin, F. Pan, L. Yang, *Sci. Bull.* **2023**, *68*, 408.
[173] D. Kim, S. Lee, W. Hong, H. Lee, S. Jeon, S. Han, J. Nam, *Microsc. Microanal.* **2019**, *25*, 1139.
[174] V. Vanpeene, P. Soucy, J. Xiong, N. Dupré, B. Lestriez, L. Roué, *J. Power Sources* **2021**, *498*, 229904.
[175] T. Danner, S. Eswara, V. P. Schulz, A. Latz, *J. Power Sources* **2016**, *324*, 646.
[176] M. Augustin, P. E. Vullum, F. Vullum-Bruer, A. M. Svensson, *J. Power Sources Adv.* **2023**, *20*, 100113.
[177] M. Biton, F. Tariq, V. Yufit, Z. Chen, N. Brandon, *Acta Mater.* **2017**, *141*, 39.
[178] F. Walther, F. Strauss, X. Wu, B. Mogwitz, J. Hertle, J. Sann, M. Rohnke, T. Brezesinski, J. Janek, *Chem. Mater.* **2021**, *33*, 2110.
[179] T. Shi, Y. Q. Zhang, Q. Tu, Y. Wang, M. C. Scott, G. Ceder, *J. Mater. Chem. A* **2020**, *8*, 17399.
[180] J. Zhao, Y. Tang, Q. Dai, C. Du, Y. Zhang, D. Xue, T. Chen, J. Chen, B. Wang, J. Yao, N. Zhao, Y. Li, S. Xia, X. Guo, S. J. Harris, L. Zhang, S. Zhang, T. Zhu, J. Huang, *Energy Environ. Mater.* **2022**, *5*, 524.
[181] S. Kranz, T. Kranz, A. G. Jaegermann, B. Roling, *J. Power Sources* **2019**, *418*, 138.
[182] J. Yang, D. Li, X. Wang, X. Zhang, J. Xu, J. Chen, *Energy Storage Mater.* **2020**, *24*, 694.
[183] N. Nan, J. Wang, A. A. Eckstein, *Adv. Mater. Sci. Eng.* **2019**, *2019*, 8680715.
[184] Y. Katayanagi, T. Shimizu, Y. Hashimasa, N. Matsushita, Y. Yamazaki, T. Yamaguchi, *J. Power Sources* **2015**, *280*, 210.
[185] B. Tratnik, N. Van De Velde, I. Jerman, G. Kapun, E. Tchernychova, M. Tomšič, A. Jamnik, B. Genorio, A. Vizintin, R. Dominko, *ACS Appl. Energy Mater.* **2022**, *5*, 10667.

[186] G. Binnig, H. Rohrer, C. Gerber, E. Weibel, *Appl. Phys. Lett.* **1982**, *40*, 178.
[187] Y. Takahashi, D. Takamatsu, Y. Korchev, T. Fukuma, *JACS Au* **2023**, *3*, 1089.
[188] S. Yang, J. Wu, B. Yan, L. Li, Y. Sun, L. Lu, K. Zeng, *J. Power Sources* **2017**, *352*, 9.
[189] L. Danis, S. M. Gateman, C. Kuss, S. B. Schougaard, J. Mauzeroll, *ChemElectroChem* **2017**, *4*, 6.
[190] R. Kempaiah, G. Vasudevamurthy, A. Subramanian, *Nano Energy* **2019**, *65*, 103925.
[191] F. Buchner, B. Uhl, K. Forster-Tonigold, J. Bansmann, A. Groß, R. J. Behm, *J. Chem. Phys.* **2018**, *148*, 193821.
[192] D. Liu, Z. Shadike, R. Lin, K. Qian, H. Li, K. Li, S. Wang, Q. Yu, M. Liu, S. Ganapathy, X. Qin, Q. Yang, M. Wagemaker, F. Kang, X. Yang, B. Li, *Adv. Mater.* **2019**, *31*, 1806620.
[193] J. Wan, H.-J. Yan, R. Wen, L.-J. Wan, *ACS Energy Lett.* **2022**, *7*, 2988.
[194] A. Mishra, D. Sarbapalli, O. Rodríguez, J. Rodríguez-López, *Annu. Rev. Anal. Chem.* **2023**, *16*, 93.
[195] X. Lu, Q. Wang, X. Liu, *Anal. Chim. Acta* **2007**, *601*, 10.
[196] S. Tan, D. Perry, P. R. Unwin, *J. Electroanal. Chem.* **2018**, *819*, 240.
[197] A. Mishra, D. Sarbapalli, Md. S. Hossain, Z. T. Gossage, Z. Li, A. Urban, J. Rodríguez-López, *J. Electrochem. Soc.* **2022**, *169*, 086501.
[198] S. Y. Luchkin, S. A. Lipovskikh, N. S. Katorova, A. A. Savina, A. M. Abakumov, K. J. Stevenson, *Sci. Rep.* **2020**, *10*, 8550.
[199] N. Balke, S. Jesse, A. N. Morozovska, E. Eliseev, D. W. Chung, Y. Kim, L. Adamczyk, R. E. García, N. Dudney, S. V. Kalinin, *Nat. Nanotechnol.* **2010**, *5*, 749.
[200] S. D. Lacey, J. Wan, A. V. W. Cresce, S. M. Russell, J. Dai, W. Bao, K. Xu, L. Hu, *Nano Lett.* **2015**, *15*, 1018.
[201] N. Weadock, N. Varongchayakul, J. Wan, S. Lee, J. Seog, L. Hu, *Nano Energy* **2013**, *2*, 713.
[202] J. Zhang, R. Wang, X. Yang, W. Lu, X. Wu, X. Wang, H. Li, L. Chen, *Nano Lett.* **2012**, *12*, 2153.
[203] P. Eaton, P. West, *Atomic Force Microscopy* (Eds: P. Eaton, P. West), Oxford University Press, Oxford **2010**, pp. 121–138.
[204] S. Daboss, T. Philipp, K. Palanisamy, J. Flowers, H. S. Stein, C. Kranz, *Electrochim. Acta* **2023**, *453*, 142345.
[205] H. Pan, Y. Chen, W. Pang, H. Sun, J. Li, Y. Lin, O. Kolosov, Z. Huang, *MethodsX* **2021**, *8*, 101250.
[206] B. Tao, L. C. Yule, E. Daviddi, C. L. Bentley, P. R. Unwin, *Angew. Chem., Int. Ed.* **2019**, *58*, 4606.
[207] A. J. Bard, F. R. F. Fan, J. Kwak, O. Lev, *Anal. Chem.* **1989**, *61*, 132.
[208] D. O. Wipf, A. J. Bard, D. E. Tallman, *Anal. Chem.* **1993**, *65*, 1373.
[209] G. Zampardi, S. Klink, V. Kuznetsov, T. Erichsen, A. Maljusch, F. LaMantia, W. Schuhmann, E. Ventosa, *ChemElectroChem* **2015**, *2*, 1607.
[210] H. Bülter, F. Peters, J. Schwenzel, G. Wittstock, *Angew. Chem., Int. Ed.* **2014**, *53*, 10531.
[211] H. Bülter, F. Peters, G. Wittstock, *Energy Technol.* **2016**, *4*, 1486.
[212] B. Krueger, L. Balboa, J. F. Dohmann, M. Winter, P. Bieker, G. Wittstock, *ChemElectroChem* **2020**, *7*, 3590.
[213] F. Xu, B. Beak, C. Jung, *J. Solid State Electrochem.* **2012**, *16*, 305.
[214] A. Kumatani, T. Matsue, *Curr. Opin. Electrochem.* **2020**, *22*, 228.
[215] E. Ventosa, W. Schuhmann, *Phys. Chem. Chem. Phys.* **2015**, *17*, 28441.
[216] E. Ventosa, E. Madej, G. Zampardi, B. Mei, P. Weide, H. Antoni, F. La Mantia, M. Muhler, W. Schuhmann, *ACS Appl. Mater. Interfaces* **2017**, *9*, 3123.
[217] P. Schwager, H. Bülter, I. Plettenberg, G. Wittstock, *Energy Technol.* **2016**, *4*, 1472.
[218] Y. Takahashi, A. Kumatani, H. Munakata, H. Inomata, K. Ito, K. Ino, H. Shiku, P. R. Unwin, Y. E. Korchev, K. Kanamura, T. Matsue, *Nat. Commun.* **2014**, *5*, 5450.
[219] Z. J. Barton, J. Rodríguez-López, *Anal. Chem.* **2014**, *86*, 10660.
[220] W. Li, *J. Electrochem. Soc.* **2020**, *167*, 090514.
[221] E. Peled, S. Menkin, *J. Electrochem. Soc.* **2017**, *164*, A1703.
[222] B. Ballesteros Katemann, A. Schulte, E. J. Calvo, M. Koudelka-Hep, W. Schuhmann, *Electrochem. Commun.* **2002**, *4*, 134.
[223] C. S. Santos, A. Botz, A. S. Bandarenka, E. Ventosa, W. Schuhmann, *Angew. Chem., Int. Ed.* **2022**, *61*, e202202744.
[224] A. N. Patel, C. Kranz, *Annu. Rev. Anal. Chem.* **2018**, *11*, 329.
[225] A. Page, D. Perry, P. R. Unwin, *Proc. R. Soc. A* **2017**, *473*, 20160889.
[226] Y. Takahashi, A. I. Shevchuk, P. Novak, Y. Zhang, N. Ebejer, J. V. Macpherson, P. R. Unwin, A. J. Pollard, D. Roy, C. A. Clifford, H. Shiku, T. Matsue, D. Klenerman, Y. E. Korchev, *Angew. Chem., Int. Ed.* **2011**, *50*, 9638.
[227] C. Kranz, C. Demaille, in *Scanning Electrochemical Microscopy*, (Eds: A. J. Bard, M. V. Mirkin), CRC Press, Boca Raton **2022**, pp. 513–560.
[228] S. Daboss, F. Rahmanian, H. S. Stein, C. Kranz, *Electrochem. Sci. Adv.* **2022**, *2*, e2100122.
[229] N. S. Katorova, S. Y. Luchkin, D. P. Rupasov, A. M. Abakumov, K. J. Stevenson, *J. Chem. Phys.* **2020**, *152*, 194704.
[230] X. Zhang, J. Yang, Z. Ren, K. Xie, Q. Ye, F. Xu, X. Liu, *New Carbon Mater.* **2022**, *37*, 371.
[231] Y. Zeng, Z. T. Gossage, D. Sarbapalli, J. Hui, J. Rodríguez-López, *ChemElectroChem* **2022**, *9*, 202101445.
[232] P. Desai, J. Forero-Saboya, V. Meunier, G. Rousse, M. Deschamps, A. M. Abakumov, J.-M. Tarascon, S. Mariyappan, *Energy Storage Mater.* **2023**, *57*, 102.
[233] A. Rudola, A. J. R. Rennie, R. Heap, S. S. Meysami, A. Lowbridge, F. Mazzali, R. Sayers, C. J. Wright, J. Barker, *J. Mater. Chem. A* **2021**, *9*, 8279.
[234] N. Tapia-Ruiz, A. R. Armstrong, H. Alptekin, M. A. Amores, H. Au, J. Barker, R. Boston, W. R. Brant, J. M. Brittain, Y. Chen, M. Chhowalla, Y.-S. Choi, S. I. R. Costa, M. Crespo Ribadeneyra, S. A. Cussen, E. J. Cussen, W. I. F. David, A. V. Desai, S. A. M. Dickson, E. I. Eweka, J. D. Forero-Saboya, C. P. Grey, J. M. Griffin, P. Gross, X. Hua, J. T. S. Irvine, P. Johansson, M. O. Jones, M. Karlsmo, E. Kendrick, et al., *J. Phys. Energy* **2021**, *3*, 031503.
[235] A. Ponrouch, A. R. Goñi, M. R. Palacín, *Electrochem. Commun.* **2013**, *27*, 85.
[236] K. Pan, H. Lu, F. Zhong, X. Ai, H. Yang, Y. Cao, *ACS Appl. Mater. Interfaces* **2018**, *10*, 39651.
[237] L. A. Ma, A. J. Naylor, L. Nyholm, R. Younesi, *Angew. Chem., Int. Ed.* **2021**, *60*, 4855.
[238] R. Cornut, C. Lefrou, *J. Electroanal. Chem.* **2008**, *621*, 178.
[239] Y. Wang, E. I. Rogers, R. G. Compton, *J. Electroanal. Chem.* **2010**, *648*, 15.
[240] K. Faber, F. Badaczewski, W. Ruland, B. M. Smarsly, *Z. Anorg. Allg. Chem.* **2014**, *640*, 3107.
[241] C. Cai, Y. Chen, P. Hu, T. Zhu, X. Li, Q. Yu, L. Zhou, X. Yang, L. Mai, *Small* **2022**, *18*, 2105303.
[242] Y. Chu, J. Zhang, Y. Zhang, Q. Li, Y. Jia, X. Dong, J. Xiao, Y. Tao, Q.-H. Yang, *Adv. Mater.* **2023**, *35*, 2212186.
[243] W. Ruland, B. Smarsly, *J. Appl. Crystallogr.* **2002**, *35*, 624.
[244] O. Osswald, M. O. Loeh, F. M. Badaczewski, T. Pfaff, H. E. Fischer, A. Franz, J.-U. Hoffmann, M. Reehuis, P. J. Klar, B. M. Smarsly, *C* **2023**, *9*, 27.
[245] Y. Morikawa, S. Nishimura, R. Hashimoto, M. Ohnuma, A. Yamada, *Adv. Energy Mater.* **2020**, *10*, 1903176.
[246] C. Glatthaar, M. Wang, L.-Q. Wagner, F. Breckwoldt, Z. Guo, K. Zheng, M. Kriechbaum, H. Amenitsch, M.-M. Titirici, B. M.

Smarsly, *Chemistry of Materials* **2023**, https://doi.org/10.1021/acs.chemmater.3c01520.
[247] P. Poizot, S. Laruelle, S. Grugeon, L. Dupont, J. M. Tarascon, *Nature* **2000**, *407*, 496.
[248] K. Wang, W. Hua, X. Huang, D. Stenzel, J. Wang, Z. Ding, Y. Cui, Q. Wang, H. Ehrenberg, B. Breitung, C. Kübel, X. Mu, *Nat. Commun.* **2023**, *14*, 1487.
[249] M. D. Slater, D. Kim, E. Lee, C. S. Johnson, *Adv. Funct. Mater.* **2013**, *23*, 947.
[250] J. M. Tarascon, M. Armand, *Nature* **2001**, *414*, 359.
[251] *Transmission Electron Microscopy: Diffraction, Imaging, and Spectrometry*, (Eds: C. B. Carter, D. B. Williams), Springer, Berlin **2016**.
[252] *Scanning Transmission Electron Microscopy: Imaging and Analysis*, (Eds: S. J. Pennycook, P. D. Nellist), Springer, Berlin **2011**.
[253] C. Ophus, *Microsc. Microanal.* **2019**, *25*, 563.
[254] X. Mu, A. Kobler, D. Wang, V. S. K. Chakravadhanula, S. Schlabach, D. V. Szabó, P. Norby, C. Kübel, *Ultramicroscopy* **2016**, *170*, 10.
[255] X. Zhou, A. Ahmadian, B. Gault, C. Ophus, C. H. Liebscher, G. Dehm, D. Raabe, *Nat. Commun.* **2023**, *14*, 3535.
[256] J. Ryu, S. Lee, S. Kim, Y.-C. Joo, M. Kim, *Appl. Phys. Lett.* **2022**, *121*, 042101.
[257] J. Wei, T. Ogawa, B. Feng, T. Yokoi, R. Ishikawa, A. Kuwabara, K. Matsunaga, N. Shibata, Y. Ikuhara, *Nano Lett.* **2020**, *20*, 2530.
[258] L. Hughes, B. Savitzky, C. Gopal, P. Herring, A. Anapolsky, C. Ophus, A. Minor, *Microsc. Microanal.* **2020**, *26*, 150.
[259] Z. Ding, Y. Tang, T. Ortmann, J.-K. Eckhardt, Y. Dai, M. Rohnke, G. Melinte, C. Heiliger, J. Janek, C. Kübel, *Advanced Energy Materials. Portico* **2023**, https://doi.org/10.1002/aenm.202302322.
[260] X. Mu, A. Mazilkin, C. Sprau, A. Colsmann, C. Kübel, *Microscopy* **2019**, *68*, 301.
[261] O. L. Krivanek, N. Dellby, J. A. Hachtel, J.-C. Idrobo, M. T. Hotz, B. Plotkin-Swing, N. J. Bacon, A. L. Bleloch, G. J. Corbin, M. V. Hoffman, C. E. Meyer, T. C. Lovejoy, *Ultramicroscopy* **2019**, *203*, 60.
[262] J. N. Agar, in *Advances in Electrochemistry and Electrochemical Engineering*, (Ed: P. Delahay), Interscience Publishers, London **1963**, pp. 31–121.
[263] T. Ozeki, N. Ogawa, K. Aikawa, I. Watanabe, S. Ikeda, *J. Electroanal. Chem. Interfacial Electrochem.* **1983**, *145*, 53.
[264] R. Schuster, *Curr. Opin. Electrochem.* **2017**, *1*, 88.
[265] P. Boudeville, *Inorg. Chim. Acta* **1994**, *226*, 69.
[266] S. Frittmann, V. Halka, C. Jaramillo, R. Schuster, *Rev. Sci. Instrum.* **2015**, *86*, 064102.
[267] V. S. Donepudi, B. E. Conway, *J. Electrochem. Soc.* **1984**, *131*, 1477.
[268] M. J. Schmid, K. R. Bickel, P. Novák, R. Schuster, *Angew. Chem., Int. Ed.* **2013**, *52*, 13233.
[269] F. Karcher, M. Uhl, T. Geng, T. Jacob, R. Schuster, *Angew. Chem., Int. Ed.* **2023**, *62*, e202301253.
[270] J. R. Dahn, W. R. McKinnon, J. J. Murray, R. R. Haering, R. S. McMillan, A. H. Rivers-Bowerman, *Phys. Rev. B: Condens. Matter Mater. Phys.* **1985**, *32*, 3316.
[271] L. E. Downie, L. J. Krause, J. C. Burns, L. D. Jensen, V. L. Chevrier, J. R. Dahn, *J. Electrochem. Soc.* **2013**, *160*, A588.
[272] A. F. Gunnarshaug, P. J. S. Vie, S. Kjelstrup, *J. Electrochem. Soc.* **2021**, *168*, 050522.
[273] A. F. Gunnarshaug, P. J. S. Vie, S. Kjelstrup, *J. Electrochem. Soc.* **2023**, *170*, 049001.
[274] Y. Reynier, J. Graetz, T. Swan-Wood, P. Rez, R. Yazami, B. Fultz, *Phys. Rev. B* **2004**, *70*, 174304.
[275] P. J. Osswald, M. Del Rosario, J. Garche, A. Jossen, H. E. Hoster, *Electrochim. Acta* **2015**, *177*, 270.
[276] M. P. Mercer, S. Affleck, E. M. Gavilán–Arriazu, A. A. Zülke, P. A. Maughan, S. Trivedi, M. Fichtner, A. R. Munnangi, E. P. M. Leiva, H. E. Hoster, *ChemPhysChem* **2022**, *23*, 202100748.
[277] F. Karcher, M. Uhl, T. Geng, T. Jacob, R. Schuster, *Angewandte Chemie International Edition. Portico* **2023**, *62*, https://doi.org/10.1002/anie.202301253.
[278] O. Pecher, J. Carretero-González, K. J. Griffith, C. P. Grey, *Chem. Mater.* **2017**, *29*, 213.
[279] X. Liu, Z. Liang, Y. Xiang, M. Lin, Q. Li, Z. Liu, G. Zhong, R. Fu, Y. Yang, *Adv. Mater.* **2021**, *33*, 2005878.
[280] T. Zhang, C. Li, F. Wang, A. Noori, M. F. Mousavi, X. Xia, Y. Zhang, *Chem. Rec.* **2022**, *22*, e202200083.
[281] S. Kajiyama, L. Szabova, K. Sodeyama, H. Iinuma, R. Morita, K. Gotoh, Y. Tateyama, M. Okubo, A. Yamada, *ACS Nano* **2016**, *10*, 3334.
[282] B. Chen, M. Liang, Q. Wu, S. Zhu, N. Zhao, C. He, *Trans. Tianjin Univ.* **2022**, *28*, 6.
[283] E. Šić, M. Melzi d'Eril, K. Schutjajew, M. J. Graczyk-Zajac, H. Breitzke, R. Riedel, M. Oschatz, T. Gutmann, G. Buntkowsky, *Batteries Supercaps* **2022**, *5*, 202200066.
[284] J. M. Stratford, M. Mayo, P. K. Allan, O. Pecher, O. J. Borkiewicz, K. M. Wiaderek, K. W. Chapman, C. J. Pickard, A. J. Morris, C. P. Grey, *J. Am. Chem. Soc.* **2017**, *139*, 7273.
[285] X. Zhang, X. Rui, D. Chen, H. Tan, D. Yang, S. Huang, Y. Yu, *Nanoscale* **2019**, *11*, 2556.
[286] M. A. Reddy, H. Euchner, R. Witter, O. Clemens, *J. Mater. Chem. A* **2018**, *6*, 6947.
[287] P. Serras, V. Palomares, J. Alonso, N. Sharma, J. M. López del Amo, P. Kubiak, M. L. Fdez-Gubieda, T. Rojo, *Chem. Mater.* **2013**, *25*, 4917.
[288] C. Yu, S. Ganapathy, N. J. J. de Klerk, E. R. H. van Eck, M. Wagemaker, *J. Mater. Chem. A* **2016**, *4*, 15095.
[289] G. Oyama, O. Pecher, K. J. Griffith, S. Nishimura, R. Pigliapochi, C. P. Grey, A. Yamada, *Chem. Mater.* **2016**, *28*, 5321.
[290] X. Wu, G. Zhong, Y. Yang, *J. Power Sources* **2016**, *327*, 666.
[291] Q. Li, Z. Liu, F. Zheng, R. Liu, J. Lee, G.-L. Xu, G. Zhong, X. Hou, R. Fu, Z. Chen, K. Amine, J. Mi, S. Wu, C. P. Grey, Y. Yang, *Angew. Chem.* **2018**, *130*, 12094.
[292] M. Chen, Q. Liu, S.-W. Wang, E. Wang, X. Guo, S.-L. Chou, *Adv. Energy Mater.* **2019**, *9*, 1803609.
[293] S. Takeda, Y. Umehara, H. Hara, G. Maruta, *Mol. Cryst. Liq. Cryst.* **2002**, *379*, 253.
[294] Y. Liu, J. Li, Q. Shen, J. Zhang, P. He, X. Qu, Y. Liu, *eScience* **2022**, *2*, 10.
[295] A. Samoson, *J. Magn. Reson.* **2019**, *306*, 167.
[296] Y. Nishiyama, G. Hou, V. Agarwal, Y. Su, A. Ramamoorthy, *Chem. Rev.* **2023**, *123*, 918.
[297] E. P. Saliba, E. L. Sesti, F. J. Scott, B. J. Albert, E. J. Choi, N. Alaniva, C. Gao, A. B. Barnes, *J. Am. Chem. Soc.* **2017**, *139*, 6310.
[298] A. J. Ilott, M. Mohammadi, C. M. Schauerman, M. J. Ganter, A. Jerschow, *Nat. Commun.* **2018**, *9*, 1776.
[299] Y. Xiang, X. Li, Y. Cheng, X. Sun, Y. Yang, *Mater. Today* **2020**, *36*, 139.
[300] P.-H. Chien, K. J. Griffith, H. Liu, Z. Gan, Y.-Y. Hu, *Annu. Rev. Mater. Res.* **2020**, *50*, 493.
[301] R. Morita, K. Gotoh, K. Kubota, S. Komaba, K. Hashi, T. Shimizu, H. Ishida, *Carbon* **2019**, *145*, 712.
[302] A.-I. Freytag, A. D. Pauric, S. A. Krachkovskiy, G. R. Goward, *J. Am. Chem. Soc.* **2019**, *141*, 13758.
[303] P. Shan, J. Chen, M. Tao, D. Zhao, H. Lin, R. Fu, Y. Yang, *J. Magn. Reson.* **2023**, *353*, 107516.
[304] I. Mohammad, M.-A. Cambaz, A. Samoson, M. Fichtner, R. Witter, *Solid State Nuclear Magnetic Resonance* **2023**, *101914*, https://doi.org/10.1016/j.ssnmr.2023.101914.
[305] I. Kaminker, *Isr. J. Chem.* **2019**, *59*, 990.
[306] T. Biedenbänder, V. Aladin, S. Saeidpour, B. Corzilius, *Chem. Rev.* **2022**, *122*, 9738.

[307] W. Lee, Y. Kim, in *Sodium-Ion Batteries*, (Eds: M.-M. Titirici, P. Adelhelm, Y.-S. Hu), John Wiley & Sons, Ltd., New York **2022**, pp. 603–640.
[308] M. Born, R. Oppenheimer, *Ann. Phys.* **1927**, *389*, 457.
[309] W. Kohn, L. J. Sham, *Phys. Rev.* **1965**, *140*, A1133.
[310] N. Mardirossian, M. Head-Gordon, *Mol. Phys.* **2017**, *115*, 2315.
[311] G. Kresse, J. Hafner, *Phys. Rev. B* **1993**, *47*, 558.
[312] D. Marx, J. Hutter, *Ab Initio Molecular Dynamics: Basic Theory and Advanced Methods*, Cambridge University Press, Cambridge **2009**.
[313] Q. Liu, D. Mu, B. Wu, L. Wang, L. Gai, F. Wu, *ChemSusChem* **2017**, *10*, 786.
[314] H. Kumar, E. Detsi, D. P. Abraham, V. B. Shenoy, *Chem. Mater.* **2016**, *28*, 8930.
[315] B. Xiao, F. A. Soto, M. Gu, K. S. Han, J. Song, H. Wang, M. H. Engelhard, V. Murugesan, K. T. Mueller, D. Reed, V. L. Sprenkle, P. B. Balbuena, X. Li, *Adv. Energy Mater.* **2018**, *8*, 1801441.
[316] K. Gotoh, T. Yamakami, I. Nishimura, H. Kometani, H. Ando, K. Hashi, T. Shimizu, H. Ishida, *J. Mater. Chem. A* **2020**, *8*, 14472.
[317] C. Yu, S. Ganapathy, E.-R. H. van Eck, H. Wang, S. Basak, Z. Li, M. Wagemaker, *Nat. Commun.* **2017**, *8*, https://doi.org/10.1038/s41467-017-01187-y.
[318] P.-H. Chien, X. Feng, M. Tang, J.-T. Rosenberg, S. O'Neill, J. Zheng, S.-C. Grant, Y. Y. Hu, *J. Phys. Chem. Lett.* **2018**, *9*, 1990.
[319] M. Wilkening, P. Heitjans, *ChemPhysChem* **2011**, *13*, 53.
[320] S. Nosé, *J. Chem. Phys.* **1984**, *81*, 511.
[321] K. Toukan, A. Rahman, *Phys. Rev. B* **1985**, *31*, 2643.
[322] L. Monticelli, D. P. Tieleman, in *Biomolecular Simulations: Methods and Protocols*, (Eds: L. Monticelli, E. Salonen), Humana Press, Totowa, NJ **2013**, pp. 197–213.
[323] A. Agrawal, S. Janakiraman, K. Biswas, A. Venimadhav, S. K. Srivastava, S. Ghosh, *Electrochim. Acta* **2019**, *317*, 164.
[324] J.-X. Huang, G. Csányi, J.-B. Zhao, J. Cheng, V. L. Deringer, *J. Mater. Chem. A* **2019**, *7*, 19070.
[325] C. Bommier, X. Ji, P. A. Greaney, *Chem. Mater.* **2019**, *31*, 658.
[326] M. Andersen, C. Panosetti, K. Reuter, *Front. Chem.* **2019**, *7*, 202.
[327] N. Metropolis, S. Ulam, *J. Am. Stat. Assoc.* **1949**, *44*, 335.
[328] M. Gerasimov, F. A. Soto, J. Wagner, F. Baakes, N. Guo, F. Ospina-Acevedo, F. Röder, P. B. Balbuena, U. Krewer, *J. Phys. Chem. C* **2023**, *127*, 4872.
[329] J. S. Newman, C. W. Tobias, *J. Electrochem. Soc.* **1962**, *109*, 1183.
[330] F. B. Planella, W. Ai, A. M. Boyce, A. Ghosh, I. Korotkin, S. Sahu, V. Sulzer, R. Timms, T. G. Tranter, M. Zyskin, S. J. Cooper, J. S. Edge, J. M. Foster, M. Marinescu, B. Wu, G. Richardson, *Prog. Energy* **2022**, *4*, 042003.
[331] Y. Kuhn, H. Wolf, A. Latz, B. Horstmann, *Batteries Supercaps* **2023**, *6*, 202200374.
[332] L. von Kolzenberg, A. Latz, B. Horstmann, *ChemSusChem* **2020**, *13*, 3901.
[333] A. M. Colclasure, K. A. Smith, R. J. Kee, *Electrochim. Acta* **2011**, *58*, 33.
[334] D. Witt, F. Röder, U. Krewer, *Batteries Supercaps* **2022**, *5*, 202200067.
[335] M. Tanaka, J. B. Hooper, D. Bedrov, *ACS Appl. Energy Mater.* **2018**, *1*, 1858.
[336] S. Toghyani, F. Baakes, N. Zhang, H. Kühnelt, W. Cistjakov, U. Krewer, *J. Electrochem. Soc.* **2022**, *169*, 040550.
[337] J. Lian, M. Koch, W. Li, T. Wierzbicki, J. Zhu, *J. Electrochem. Soc.* **2020**, *167*, 090556.
[338] F. Baakes, M. Lüthe, M. Gerasimov, V. Laue, F. Röder, P. B. Balbuena, U. Krewer, *J. Power Sources* **2022**, *522*, 230881.
[339] A. Benayad, D. Diddens, A. Heuer, A. N. Krishnamoorthy, M. Maiti, F. L. Cras, M. Legallais, F. Rahmanian, Y. Shin, H. Stein, M. Winter, C. Wölke, P. Yan, I. Cekic-Laskovic, *Adv. Energy Mater.* **2022**, *12*, 2102678.
[340] S. P. Ong, *Comput. Mater. Sci.* **2019**, *161*, 143.
[341] J. M. Zheng, Z. R. Zhang, X. B. Wu, Z. X. Dong, Z. Zhu, Y. Yang, *J. Electrochem. Soc.* **2008**, *155*, A775.
[342] A. Tokranov, B. W. Sheldon, P. Lu, X. Xiao, A. Mukhopadhyay, *J. Electrochem. Soc.* **2014**, *161*, A58.
[343] B. Qin, A. Schiele, Z. Jusys, A. Mariani, T. Diemant, X. Liu, T. Brezesinski, R. J. Behm, A. Varzi, S. Passerini, *ACS Appl. Mater. Interfaces* **2020**, *12*, 3697.
[344] P. G. Kitz, M. J. Lacey, P. Novák, E. J. Berg, *Anal. Chem.* **2019**, *91*, 2296.
[345] C. K. Chan, R. Ruffo, S. S. Hong, Y. Cui, *J. Power Sources* **2009**, *189*, 1132.
[346] K. K. Neelisetty, X. Mu, S. Gutsch, A. Vahl, A. Molinari, F. von Seggern, M. Hansen, T. Scherer, M. Zacharias, L. Kienle, V. K. Chakravadhanula, C. Kübel, *Microsc. Microanal.* **2019**, *25*, 592.
[347] J. Asenbauer, A.-L. Wirsching, M. Lang, S. Indris, T. Eisenmann, A. Mullaliu, A. Birrozzi, A. Hoefling, D. Geiger, U. Kaiser, R. Schuster, D. Bresser, *Adv. Sustainable Syst.* **2022**, *6*, 2200102.
[348] A. Ramasubramanian, V. Yurkiv, T. Foroozan, M. Ragone, R. Shahbazian-Yassar, F. Mashayek, *J. Phys. Chem. C* **2019**, *123*, 10237.
[349] A. M. Kia, J. Speulmanns, S. Bönhardt, J. Emara, K. Kühnel, N. Haufe, W. Weinreich, *Appl. Surf. Sci.* **2021**, *564*, 150457.
[350] Z. Ding, Y. Tang, V. S. K. Chakravadhanula, Q. Ma, F. Tietz, Y. Dai, T. Scherer, C. Kübel, *Microscopy* **2022**, *72*, 326.
[351] D.-S. Bin, Y. Li, Y.-G. Sun, S.-Y. Duan, Y. Lu, J. Ma, A.-M. Cao, Y.-S. Hu, L.-J. Wan, *Adv. Energy Mater.* **2018**, *8*, 1800855.
[352] I. Källquist, T. Ericson, F. Lindgren, H. Chen, A. Shavorskiy, J. Maibach, M. Hahlin, *ACS Appl. Mater. Interfaces* **2022**, *14*, 6465.
[353] J. Maibach, I. Källquist, M. Andersson, S. Urpelainen, K. Edström, H. Rensmo, H. Siegbahn, M. Hahlin, *Nat. Commun.* **2019**, *10*, 3080.
[354] E. W. C. Spotte-Smith, S. M. Blau, D. Barter, N. J. Leon, N. T. Hahn, N. S. Redkar, K. R. Zavadil, C. Liao, K. A. Persson, *J. Am. Chem. Soc.* **2023**, *145*, 12181.
[355] A. Guéguen, P. Novák, E. J. Berg, *J. Electrochem. Soc.* **2016**, *163*, A2545.
[356] D. Monti, E. Jónsson, M. R. Palacín, P. Johansson, *J. Power Sources* **2014**, *245*, 630.
[357] K. Hankins, V. Prabhakaran, S. Wi, V. Shutthanandan, G. E. Johnson, S. Roy, H. Wang, Y. Shao, S. Thevuthasan, P. B. Balbuena, K. T. Mueller, V. Murugesan, *J. Phys. Chem. Lett.* **2021**, *12*, 9360.
[358] D. A. Rakov, F. Chen, S. A. Ferdousi, H. Li, T. Pathirana, A. N. Simonov, P. C. Howlett, R. Atkin, M. Forsyth, *Nat. Mater.* **2020**, *19*, 1096.
[359] M. Lin, R. Fu, Y. Xiang, Y. Yang, J. Cheng, *Curr. Opin. Electrochem.* **2022**, *35*, 101048.
[360] F. Röder, R. D. Braatz, U. Krewer, *Comput. Chem. Eng.* **2019**, *121*, 722.
[361] L. Xu, G. Henkelman, *J. Chem. Phys.* **2008**, *129*, 114104.
[362] S. Manna, D. Roy, S. Das, B. Pathak, *Mater. Adv.* **2022**, *3*, 7833.
[363] Z. Lu, *Mater. Rep. Energy* **2021**, *1*, 100047.
[364] D. Ouyang, M. Chen, J. Weng, K. Wang, J. Wang, Z. Wang, *J. Energy Chem.* **2023**, *81*, 543.
[365] K. Mukai, T. Inoue, *Electrochem. Commun.* **2018**, *88*, 101.
[366] I. Escher, M. Hahn, G. A. Ferrero, P. Adelhelm, *Energy Technol.* **2022**, *10*, 2101120.
[367] T. Kim, W. Choi, H.-C. Shin, J.-Y. Choi, J. M. Kim, M.-S. Park, W.-S. Yoon, *J. Electrochem. Sci. Technol.* **2020**, *11*, 14.
[368] X. Yang, A. L. Rogach, *Adv. Energy Mater.* **2019**, *9*, 1900747.

[369] Y. Zhu, T. Gao, X. Fan, F. Han, C. Wang, *Acc. Chem. Res.* **2017**, *50*, 1022.
[370] Z. Shadike, E. Zhao, Y.-N. Zhou, X. Yu, Y. Yang, E. Hu, S. Bak, L. Gu, X.-Q. Yang, *Adv. Energy Mater.* **2018**, *8*, 1702588.
[371] G. Åvall, J. Mindemark, D. Brandell, P. Johansson, *Adv. Energy Mater.* **2018**, *8*, 1703036.
[372] Q. Bai, L. Yang, H. Chen, Y. Mo, *Adv. Energy Mater.* **2018**, *8*, 1702998.
[373] J. K. C. Ding Ziming, T. Yushu, O. Till, E. J. Kevin, M. Giogine, Janek, *Adv. Energy Mat.* **2013**, *13*, 2302322.
[374] J. Eills, D. Budker, S. Cavagnero, E. Y. Chekmenev, S. J. Elliott, S. Jannin, A. Lesage, J. Matysik, T. Meersmann, T. Prisner, J.-A. Reimer, H. Yang, I.-V. Koptyug, *Chem. Rev.* **2023**, *123*, 1417.
[375] S. Haber, M. Leskes, *Solid State Nucl. Magn. Reson.* **2022**, *117*, 101763.